JIE FAN

MORPHOLOGICAL CHARACTERIZATION AND ANALYSIS OF THIN, CONTINUUM STRUCTURES BASED ON NON-CONSTANT CURVATURE CLOTHOID SPIRAL

Taking Inspiration from Climbing Organs - Tendrils

MORPHOLOGICAL CHARACTERIZATION AND ANALYSIS OF THIN, CONTINUUM STRUCTURES BASED ON NON-CONSTANT CURVATURE CLOTHOID SPIRAL

Taking Inspiration from Climbing Organs - Tendrils

Jie FAN



Cecilia Laschi	Professor, National University of Singapore	Reviewer
Michele Palladino	Assistant Professor, University of L'Aquila	Reviewer
Paolo Dario	Professor, Institute of BioRobotics Scuola Superiore Sant'Anna di Pisa	Supervisor
Barbara Mazzolai	Director, Bioinspired Soft Robotics Laboratory Istituto Italiano di Tecnologia	Tutor
Francesco Visentin	Assistant Professor, University of Verona	Co-Tutors
Emanuela Del Dottore	Researcher, Bioinspired Soft Robotics Laboratory Istituto Italiano di Tecnologia	Co-Tutors

A thesis submitted in fulfillment of the requirements for
the degree of Doctor of Philosophy
in
BIOROBOTICS

SCUOLA SUPERIORE SANT'ANNA
&
ISTITUTO ITALIANO DI TECNOLOGIA

May 2022

Jie Fan: *Morphological Characterization and Analysis of Thin, Continuum Structures based on Non-constant Curvature Clothoid Spiral, Taking Inspiration from Climbing Organs - Tendrils*, Doctor of Philosophy, © May 2022
Pontedera, PI

Dedicated to my family and my husband
You make me a braver and better person.

ABSTRACT

Morphological Characterization and Analysis of Thin, Continuum Structures based on Non-constant Curvature Clothoid Spiral

Taking Inspiration from Climbing Organs - Tendrils

Continuum structure, characterized by thin and slender geometries, is common to find in nature and appears to be an indispensable and essential feature of both biological and soft robotic systems. Owing to the continuous deformation of morphological configurations, such structures incorporate the common characteristics of natural systems and can provide innovative and intelligent solutions in a continuum mechanism with high compliance and adaptation when interacting with the external environment.

Taking the morphological evolution of *Passiflora caerulea* tendrils upon mechano-response as the ideal representative of continuum structures, this thesis proposed the novel marker-less methodologies to reconstruct the shape of thin, continuum structures and to analyze tendrils' curling morphologies and movement. The proposed methods are based on vision and clothoid curve models in 2D and in 3D cases, respectively. Thanks to the affine properties between the curvature and torsion linearly along with arclength, clothoid curves alow a smooth transition between straight line and curve segments. Also, the affine property characterizing the clothoid is ideal for following the changes in the shape of natural structures. For this reason, we used this approach to represent and reconstruct curling continuum structures, such as tendrils and tendril-like artificial structures.

To reconstruct the 2D morphology of tendrils, we proposed three model-based approaches: single-segment clothoid, piecewise clothoid with the prescribed number of segments, and piece-wise clothoid model with the optimal number of segments. These methods have been numerically validated on both the continuum of biological and artificial structures and also compared with constant curvature fitting results with a high average accuracy $(R^2 > 0.9)$.

Based on the 2D work, we reconstructed the morphological evolution of tendrils using stereo vision with points-correspondence by Fréchet distance and describe them using 3D piecewise clothoid curve. Then, about the dynamic analysis of stimulated tendrils, we deduced the morphologies and stimulus-response relationship of tendrils from the variation and distribution of curvature, torsion and tip movement, which are consistent with the botanists' perspectives on sensitivity and transduction.

In addition, we developed a sorting algorithm to order unarranged points for the extraction of continuum structures' center-line in images.

It is effective and adaptive in dealing with different cases, such as discontinuity, branches, and with/without intersection.

In conclusion, the main contribution of this thesis is to provide a viable solution for shape reconstruction and representation of slender-continuum structures (both natural and artificial) in planar and in space. In particular, the expected impacts of the present work are twofold:

- at the biological level, to provide an effective and practical tool to analyze tendril-like plants on behaviors and growth evolution in response to external stimuli.
- at the engineering level, to demonstrate that clothoid spiral is reliable and accurate to model and describe slender, continuum morphologies both in 2D and in 3D, which may guide the design and control of the tendril-inspired biomimetic robot with variable stiffness along the body length.

Keywords: bio-inspiration, soft robotics, continuum structure, curling shape, tendril, climbing plants, clothoid curve, shape reconstruction, morphological analysis

PUBLICATIONS

During my Ph.D., I contributed the following publications:

[1] Jie Fan, Emanuela Del Dottore, Francesco Visentin, and Barbara Mazzolai. "Image-based Approach to Reconstruct Curling in Continuum Structures." In: *2020 3rd IEEE International Conference on Soft Robotics (RoboSoft)*. 2020, pp. 544–549. DOI: 10.1109/RoboSoft48309.2020.9115981.

[2] Jie Fan, Francesco Visentin, Emanuela Del Dottore, and Barbara Mazzolai. "An Image-Based Method for the Morphological Analysis of Tendrils with 2D Piece-Wise Clothoid Approximation Model." In: *Biomimetic and Biohybrid Systems*. 2020, pp. 80–91. ISBN: 978-3-030-64313-3.

[3] Jie Fan, Francesco Visentin, Emanuela Del Dottore, and Barbara Mazzolai. "Morphological Characterization of Thin, Continuum Biological Structures based on Non-constant Curvature Analysis." In: *International Journal of Computer Vision* (2022).

Notation: The third journal has been submitted.

If you want to lift yourself up, lift up someone else.

—— Booker T. Washington

ACKNOWLEDGMENTS

Many thanks to everybody I met during my Ph.D in Italy. Many thanks to all the encounters that made me accompanied with people who like me and those I like. Because of all of you, I spent an unforgettable journey in life.

First of all, I would like to express my heartfelt gratitude to my tutor, Dr. Barbara Mazzolai, for giving me an opportunity to study and work in Bioinspired Soft Robotics Laboratory I aspired, and her excellent guidance and support throughout my Ph.D. Meanwhile, I would like to thank my supervisor Prof. Paolo Dario for his inspiring talks, advice and guidance, especially for the two courses he taught that inspired me a lot at the beginning of my research. Both of their vision, values, passion and attitude towards research are to remain with me for the rest of my career and life.

I would also like to thank my co-tutors Dr. Emanuela Del Dottore and Prof. Francesco Visentin for helping me in my research's many technical aspects. . They always acted as the lights directing me in the proper direction. Their constructive suggestions and limitless patience, along with the flexibility to conduct research, are invaluable to me, which made the Ph.D study a pleasure.

In addition, I would like to thank my reviewers Prof. Cecilia Laschi and Prof. Michele Palladino for their preccious comments and questions on my thesis.

My heartfelt appreciation goes to all of my colleagues and friends at the Bioinspired Soft Robotics Laboratory. They created a harmonious atmosphere and a supportive environment. I could get timely assistance and encouragement making my research life full of laughter and happiness. In particularly, I would give my special thanks to Emanuela, Francesco, Alessio, Edoardo, Carlo, Fabian, Laura, Giovanna, Francesca, Ali, Goffredo, Dario, Saravana, Riddhi, Joe, Vincenzo, Corrado, Ebrahim, Majid, Serena, Serena Rosa, Amir, Kliton, Luca, Oscar, Daniele, Giada, etc.

Furthermore, I would like to thank my friends met in Pontedera who accompanied me during that time in Pontedera and Genoa. I appreciated all the nice moments of laughter and delicious dinners shared with you all: Prof. Hongbo Wang, Yanjun Liu, little Zhiyuan Wang, Dr. Yu Huan, Hong Shen, Prof. Baojun Chen, Dr. Linlin Wu, Qian Zhang, Dr. Xuyang Ren, Dr. Jun Pan, Prof. Dongdong Du, Dr. Rongrong Liu, Dr. Jiaqi Wang, etc.

Finally, my deepest gratitude goes to my family and my beloved Fei for their endless love, support, encouragement and understanding all the way along. Especially, thanks to Fei and my cat TRO for drawing stars around my scars. Besides, I'm grateful that Pfizer booster vaccine taught me how important to be alive.

Everyone I've mentioned helped me improve, grow, and become a braver and better person. They also made me more curious on robtoics and love Italy. Thank you all, without you, this thesis would not have been possible.

CONTENTS

I Background

1 INTRODUCTION 3
- 1.1 Continuum Structure in Nature 3
- 1.2 Continuum Structure in Robotics 6
- 1.3 Motivation and Objectives 10
- 1.4 Contribution and Outline 11

2 STATE OF THE ART 15
- 2.1 Kinematic-based Shape Representation 15
  - 2.1.1 Rotation Frame Representation 16
  - 2.1.2 Constant Curvature Representation 17
  - 2.1.3 Pseudo-Rigid Body (PRB) Representation 18
  - 2.1.4 Distributed Curve Representation 19
- 2.2 Dynamics-based Shape Representation 19
  - 2.2.1 Cosserat Rod Representation 19
  - 2.2.2 Lumped Multi-body Representation 21
- 2.3 Sensor-based Shape Representation 21
  - 2.3.1 Fiber Optical-based Sensor 22
  - 2.3.2 Electromagnetic-based Sensor 22
- 2.4 Vision-based Shape Representation 24
  - 2.4.1 Summary 25

II Theory

3 CURVE MODELING AND RECONSTRUCTION 31
- 3.1 Clothoid Curve 31
  - 3.1.1 Definition 31
  - 3.1.2 Fresnel Integrals 32
  - 3.1.3 Fitting of a Clothoid 33
  - 3.1.4 Construction of a Clothoid Segment 33
  - 3.1.5 3D Representation of Clothoid 34
  - 3.1.6 Piecewise Integration 36
- 3.2 Multi-view Reconstruction 36
  - 3.2.1 Camera Projection Model 36
  - 3.2.2 Reconstruction from Multiple Views 38
- 3.3 Fréchet Distance 39
  - 3.3.1 Continuous Fréchet Distance 39
  - 3.3.2 Discrete Fréchet Distance 40

III Contributions

4 NONLINEAR MORPHOLOGY ANALYSIS of 2D CURLING SHAPE RECONSTRUCTION 45
- 4.1 Introduction 45
- 4.2 Biological Morphology Experiment 45

4.3 Methodology 46
4.3.1 2D Clothoid Spiral 46
4.3.2 2D Reconstruction Framework 46
4.3.3 Sorting Unarranged 2D Points 47
4.3.4 Single-Segment Clothoid Representation 50
4.3.5 Piece-wise Clothoid Representation 52
4.4 Results and Analysis 53
4.4.1 Sorting Unarranged 2D Points 54
4.4.2 Results of Single-segment Clothoid 54
4.4.3 Results of Piece-wise Clothoid 56
4.4.4 Model Validation on Soft Robotic Continuum Artefact 57
4.5 Summary 57
5 NONLINEAR MORPHOLOGY ANALYSIS of 2D CURLING SHAPE PIECEWISE RECONSTRUCTION 61
5.1 Introduction 61
5.2 Biological Morphology Experiment 61
5.3 Methodology 62
5.3.1 Weighted Sorting Skeletonization 63
5.3.2 Discrete Curvature Estimation 64
5.3.3 Automatic Selection of Segment Number 65
5.3.4 2D Piece-wise Clothoid Representation 67
5.4 Results and Analysis 69
5.5 Summary 70
6 NONLINEAR MORPHOLOGY ANALYSIS of 3D CURLING SHAPE PIECEWISE RECONSTRUCTION 73
6.1 Introduction 73
6.2 Biological Morphology Experiment 73
6.2.1 Plant 73
6.2.2 Experiment Setup 74
6.2.3 Datasets Collection 75
6.3 Shape Reconstruction 76
6.3.1 Pre-processing 76
6.3.2 Ordering Skeleton Points 78
6.3.3 Mapping Points Between Views 82
6.4 Shape Modeling 83
6.4.1 Discrete Frenet-Serrat Point Fitting 83
6.4.2 Automatic Piecewise Fitting of Curvature & Torsion 85
6.4.3 Runge-Kutta Integration 87
6.4.4 Optimal Rotation & Translation 87
6.5 Results and Analysis 89
6.5.1 Accuracy of Stereo Reconstruction 89
6.5.2 Accuracy of Clothoid Fitting 90
6.5.3 Sensitivity of Fitting Parameters 92
6.5.4 Reconstruction From a Sequence of Frames 93

6.5.5 Analysis of Tip Motions 97
6.6 Summary 98
7 CONCLUSIONS & FUTURE DIRECTIONS 101
7.1 Contributions of This Work 101
7.2 Answers of Proposed Questions 102
7.3 Limitations & Future Directions 104
7.4 Appliications 105

IV Appendix
A DERIVATION OF PARTIAL DERIVATIVES 109

Bibliography 113

LIST OF FIGURES

Figure 1.1 The three key phases of tendril movements 4
Figure 1.2 The field of bioinspiration 6
Figure 1.3 The cycle process of biomimetics design 7
Figure 1.4 Examples of bioinspired robots, soft robots and continuum robots 9
Figure 2.1 Examples of continuum structures 16
Figure 2.2 Different modeling approaches for piece-wise slender continuum structures 17
Figure 2.3 Two typical dynamics modeling approaches for the piece-wise slender continuum structures 20
Figure 3.1 Illustration of Clothoid with different parameters 33
Figure 3.2 Illustration of Clothoid's transformation 34
Figure 3.3 Multiview perspective projection 37
Figure 3.4 Multiview reconstruction flowchart 38
Figure 3.5 Illustration of Fréchet Distance 39
Figure 4.1 Flowchart of shape reconstruction by 2D clothoid 47
Figure 4.2 Procedure of ordering unarranged skeleton points 48
Figure 4.3 Examples of sorting algorithm performance 54
Figure 4.4 Results of shape analysis for selected morphologies of natural tendrils 56
Figure 4.5 Results of shape analysis for selected configurations of continuum robot 59
Figure 5.1 Flowchart of shape reconstruction by 2D PCD 62
Figure 5.2 Weighted skeleton sorting algorithm procedure 63
Figure 5.3 Estimation of discrete curvature 65
Figure 5.4 Comparison of relationship between segment number and penalties 66
Figure 5.5 Dynamic programming procedure 67
Figure 5.6 Shape analysis of natural tendrils with PCD 69
Figure 5.7 Arclength and curvature evolution over time 70
Figure 6.1 Biological experiment setup and data collection procedure 74
Figure 6.2 Segmentation prepossessing procedure 77
Figure 6.3 Sorting points algorithm without cross-intersection 79
Figure 6.4 Sorting points algorithm with one cross-intersection 81
Figure 6.5 View re-projection and Fréchet distance-based mapping 83

Figure 6.6 Shape comparison of reconstruction accuracy between tendril skeletons and projections of the stereo reconstructed tendril 89
Figure 6.7 Shape comparison of fitting accuracy between projections of stereo reconstruction tendril and PCD fitted tendril 91
Figure 6.8 PCD fitting under different penalties for selected frames 92
Figure 6.9 Penalty values selection for PCD fitting by grid search method 95
Figure 6.10 Index location distribution of each segment connection points 96
Figure 6.11 Comparison of morphology evolution of tendrils after stimuli in 4 different regions 97
Figure 6.12 Comparison of curvature & torsion from initial state to final state 98
Figure 6.13 3D tip movement of tendrils 99

LIST OF TABLES

Table 2.1 Comparison of sensing techniques - Part 1 27
Table 2.2 Comparison of sensing techniques - Part 2 28
Table 4.1 Numerical results of shape reconstruction parameters for natural tendrils by single-segment clothoid and PCD 55
Table 4.2 Numerical results of shape reconstruction parameters for continuum artefact by single-segment clothoid and PCD 58
Table 6.1 Shape comparison of reconstruction accuracy between skeletonized tendril and projections of reconstructed tendril 91
Table 6.2 Shape comparison of reconstruction accuracy between projections of reconstructed tendril and PCD fitted tendril 93
Table 6.3 Sensitivity of fitting penalties 94

ACRONYMS

ODE	Ordinary Differential Equation
MLSM	Moving Least Squares Method
MSE	Mean Square Error
PCD	Piece-wise Clothoid
PCC	Piece-wise Constant Curvature
SST	Sum of Squares Total
SSE	Sum of Squares Error
ROI	Region of Interest
RGB	Red Green Blue
HSV	Hue Saturation Value
K-NN	K-Nearest Neighbour Search
TNB	Tangent/Normal/Binormal Unit Vectors
SVD	Singular Value Decomposition
BVP	Boundary Value Problems
FBG	Fiber Bragg Gratings
EM	Electromagnetic
PRB	Pseudo-Rigid Body
RPR	Revolute-Prismatic-Revolute Joints
EOM	Equations of Motions
COG	Center of Gravity
COM	Center of Mass
DH	Denavit-Hartenberg Parameters
PDE	Partial Differential Equation
SD	Standard Deviation
ME	Mean Error

Part I

BACKGROUND

1 INTRODUCTION

1.1 CONTINUUM STRUCTURE IN NATURE

Looking into nature, the observation of biological systems encompasses diverse aspects, from single cells to complex organisms, from animals (zoology) to plants (botany), from the structure of organisms (morphology) to that of function (physiology, behavior, locomotion), etc [101]. Such aspects allow animals and plants to develop different morphologies and peculiar strategies to adapt and survive in a variety of highly competitive environments. For example, it is common for soft-bodied animals and plants to exploit their bodies' softness and deformation properties to comply with challenges offered by the environments they live in. Hereby, a few examples are mentioned.

The octopus is a marine invertebrate soft animal, whose body is characterized by eight arms that can realize various behaviors, e. g., bending, curling, twisting by elongation and squeezing muscles. Owing to these characteristics, the octopus is able to deform its body to comply with contacted objects at any point along its arm length, facilitating the capture of preys and the complex manipulation. Moreover, they adapt their behaviors by switching from manipulation to locomotion [68].

Similarly, elephants use their dexterous and compliant proboscis (trunk) having virtually infinite degrees of freedom to manipulate objects of different sizes and stiffness [115]. Meanwhile, the flexibility and stretchability of trunk allows it to reach the water far away and leaves on tall trees by stretching the muscles.

Snakes have thin and slender flexible bodies. They mainly have four different gaits of terrestrial locomotion: lateral undulation, concertina gait, sidewinding motion and rectilinear gait and tracks [76], which help to coordinate muscular propulsion and whole-body motion in response to changes in the environment. Thanks to these specific locomotion gaits, snakes can easily adapt to various terrains, move fast in 2D planes, climb on slopes with different inclinations and pass through narrow passages. Snakes are even able to swim, burrow and manipulate objects by wrapping around them.

The examples mentioned above have commonalities. They are continuum structures, appendices or entire bodies, of animals characterized by thin and slender geometries, with the *length of shape* having more impact on shape deformation compared to the *thickness of shape*.

Such morphological characteristic is not common only among animals. Plants, on their side, are also characterized by slender and

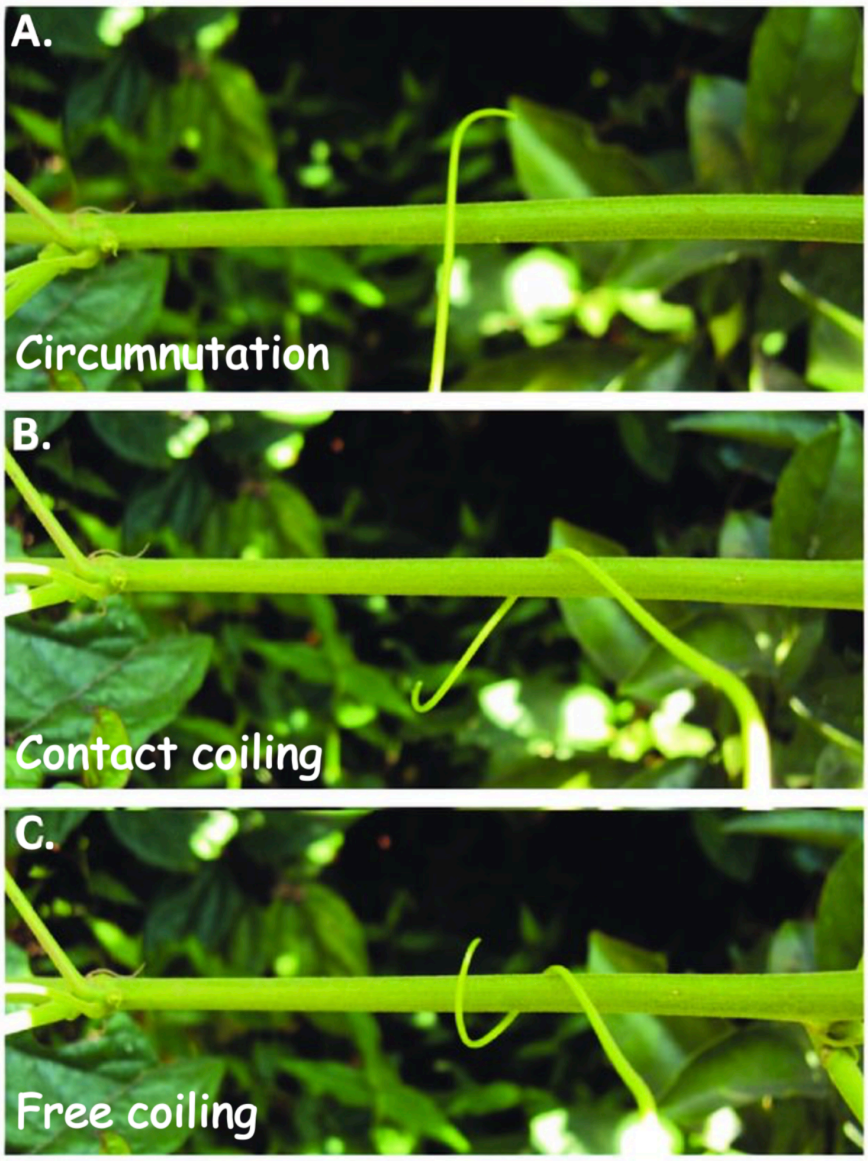


Figure 1.1: The three key phases of tendril movements [116].

continuum structures that deform, showing highly adaptive movements. Among many, climbing plants exceptionally provide interesting examples of continuum structures, which build up the main thin stem by growing and elongating cells from their apical extremities and contribute to exploring the environment. They span their shoots across voids, climb over existing structures, anchor around different kinds of supports, and finally flourish in remarkable species-specific attachment ways to race skywards for light and claim space. Based on different climbing mechanisms, Charles Darwin [11] categorized climbing plants by climbing organs, including twining stems, hooks,

leaf-bearers, adventitious clinging roots, adhesive pads, and tendril-bearers.

Among them, tendrils are specialized, long, slender filamentous organs. They are derived from reproductive structures and adopted to grasp and grow across supports by curling behavior. According to [22, 116], tendrils have three key-feature phases of movements (as illustrated in Figure 1.1): *circumnutation*, a characteristic circling movement, a strategy adopted to search for and approach a support; *contact coiling*, a strategy adopted to actively contact and confirm the ideal support and then coil around it; and *free coiling*, a strategy adopted to drag itself close to and then tightly grasp the support by coiling. The alternation of these phases requires significant morphological changes that suggest, although tendrils without specialized sensory cells [13], the extreme sensitivity of these organs to mechano-stimulation, i. e., a biological term *mechanosensing*. Jaffe [58] was the first to coin the term *thigmomorphogenesis* to describe the mechanically-induced responses in these plants' organs (i. e., morphological shaping).

Due to vast biodiversity, biologists from the 1870s started to study the irritation property of tendrils across different species. For instance, the tendrils of *Passiflora caerulea* are sensitive to contact with objects of different materials (e. g., glass, wood, metals, stones, fibers, parts of its own body and other plants) [18]. This leads to an uneven distribution of protoplasts in the epidermis [19], which results in body bending. Moreover, the rapidity and amount of response are determined by the force of impact and the roughness of object's surface rather than the composition of tendrils' body. The stimulus applied to tendrils is a crucial factor affecting their breaking strength since the number of xylem cells and the thickness of the cell wall of both the xylem and the pith increase upon contact triggering [9]. Such external stimulus can be transferred through tissues to non-disturbed distal regions, alerting the body morphology. In addition, *Passiflora* tendrils have receptors on both the ventral and dorsal surfaces that, when triggered, counteract each other's actions.

For *Peas*, the sensitivity of tendrils scattered along their body length is irregular, depending on the stage of maturity [57]. The response to the mechanical stimulus, therefore, depends on their age [57], the stimulated position [56] and the frequency of stimulation. Tendrils always curve along the ventral side after ventral stroking, and their curling capability decreases as the distance from the tip increases. The magnitude of response of *Pea* tendrils is influenced by both the amount and the frequency of the stimulus. Under the same amount of stimuli, it responds much more to a higher frequency of ventral stimulation than to a lower frequency. In addition, matured tendrils can exhibit maximum irritability with minimal change in thigmotropic sensitivity. Such generated sensitivity can be swiftly transferred from

the region where the *mechanostimulation* was received to the subjacent stem.

1.2 CONTINUUM STRUCTURE IN ROBOTICS

Nature constitutes a wonderful library of endless inspiration for creative minds for biology to technology transfer. The transition from *learning about nature* to *learning from nature* derives several concepts linked to bioinspiration, including biomimetics, bionics and biomimicry. Boundaries of these terms according to a specificity of analogies and related fields of application are presented in Figure 1.2. Although all of these concepts involve the comprehension of biological systems, they carry different purposes and underlying connotations, as well as varied significance for science and engineering.

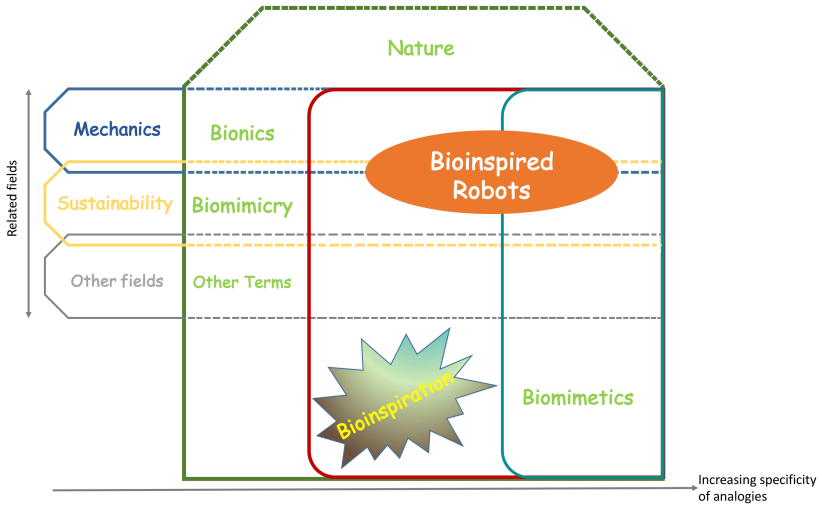


Figure 1.2: The field of bioinspiration (modified from [33]).

Some definitions have been proposed by (ISO/ TC266 2015) [55].

"Bioinspiration: a creative approach based on the observation of biological systems."

The boundary of bioinspiration covers both the divergent and convergent implementation phases of creativity (i. e., the process of fostering creativity from biological systems to deriving innovative design solutions) [33]. Thus, from an engineering perspective, bioinspiration is the nature-mentored strategy by which the properties, structures, functionalities, and exquisite mechanisms and principles of natural systems are extracted, concentrated, transferred, improved for custom purposes, and implemented in new technology.

"Biomimetics: interdisciplinary cooperation of biology and technology or other fields of innovation with the goal of solving practical problems through

the function analysis of biological systems, their abstraction into models, and the transfer into and application of these models to the solution."

Biomimetics, coined by the biomedical engineer Otto H. Schmitt [114], attempts to reproduce the biological systems. On the one hand, it draws inspiration from observing and analyzing living systems and converts them into biological models for solving human problems. On the other hand, as a problem-driven approach, biomimetics provides a working platform to test hypotheses formulated on such biological models. It allows us to examine our understanding of biological systems at all scales and know how they work without dealing with the complexity of natural systems [141]. Thus, the process model of biomimetics can be designed as a double symmetrical abstraction-specification cycle separated into two phases, as illustrated in Figure 1.3. The first phase is the transfer of biology to technology, whereas the second phase is the reverse [33].

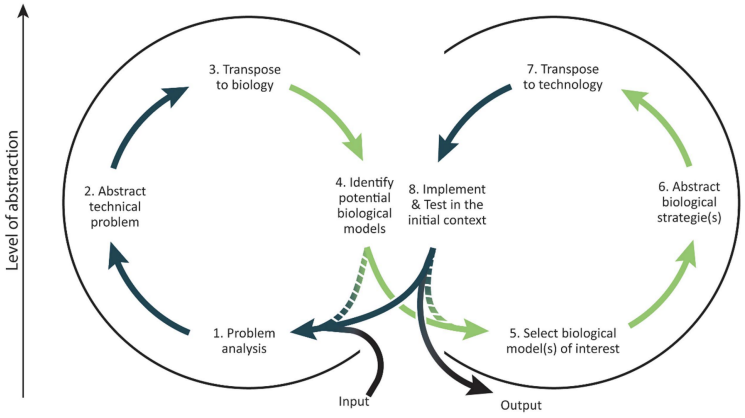


Figure 1.3: The cycle process of biomimetics design (extracted from [33]). The required contribution of biologists is marked with light green arrows (biology), while the contribution of technologists is in dark green arrows (technology).

"Biomimicry: Philosophy and interdisciplinary design approaches taking nature as a model to meet the challenges of sustainable development (social, environmental, and economic)."

Bio (life) - mimicry (imitating) was conceived by biologist Janine Benyus in her first book "Biomimicry: Innovation Inspired by Nature" [3]. From that, biomimicry could be accomplished via three levels: 1) mimicking natural forms, such as velcro strap mimicking burr, 2) mimicking natural processes with emphasis on structures and functions, and 3) mimicking natural ecosystems with the ultimate objective of obtaining sustainable solutions for establishing a balance between resources and the exploitation of nature. The key idea followed by biomimicry is that nature always operates on the principle of economy and optimal efficiency, with no waste. Its ultimate goal is to find

long-term solutions for achieving a tradoff between natural resources and exploitation.

"Bionics: technical discipline that seeks to replicate, increase, or replace biological functions by their electronic and/or mechanical equivalents."

Bionics emerged in the 1960s as a framework for developing artificial systems via studying biological systems. Until 1989, bionics became a scientific field that covers robotics, bioengineering technologies and life sciences [21]. Its ultimate goal is to develop biomimetic robots, human-centered healthcare, and assistive technologies.

From the above definitions and Figure 1.2, we can conclude that nature is a treasure trove of innovative inspiration from living systems. Bio-inspiration is a transition strategy for innovative ideas and design principles seeking from biological systems in nature, through which structural characteristics and functionality are pushed to new heights beyond what nature provides. Biomimetics focuses on methodological aspects of bio-inspiration. Biomimicry is concerned with philosophical aspects of bioinspiration part related to sustainability. Bionics focuses on bioinspiration's engineering and technological aspects, specifically involving robotics. Due to the ambiguous area division, these concepts overlap in the field of robotics, but they are all related to biological inspiration; thus we here collectively refer to them as bioinspired robots.

In robotics, there are many examples of bioinspired robots. For example, light-weight and free-moving insects inspired researchers to create flying robots capable of maneuvering in a small congested environment. Franceschini et al. [35] built an autonomous micro-helicopter robot outfitted with an optic-flow regulator and a bio-inspired optic-flow sensor. Such a fly-by-sight robot follows the same principle of navigation as insects to perform the tasks such as take-off, level flight, and landing via a visual-feedback loop. Taking inspiration from flying insects, Wood [145] designed the first insect-size robot (shown in Figure 1.4. **f.**). The gecko is able to climb along smooth vertical surfaces and ceilings thanks to its toes endowed with compliant hierarchical structures in its fingers, enabling directional adhesion. Stickybot [64] employs this biological structure and the gecko climbing mechanism to implement a force control strategy for attachment and detachment of its toes, ensuring feet-body balance (shown in Figure 1.4. **e.**). Snake-like robots (shown in Figure 1.4. **g.**) mimic the different locomotion gaits of biological snakes to coordinate muscular propulsion and whole-body motion in response to various environmental disturbances. [76, 152].

All of these examples are also biomimetics robots since they follow the cycle process of biomimetics design, which enables us "to kill two birds with one stone" [35] by unifying the creation of robots for real-world applications and the research of biological systems through robotic platforms. For instance, in [117], "*from insects to robots*" investigates how biological insects fly to achieve their agility and contributes

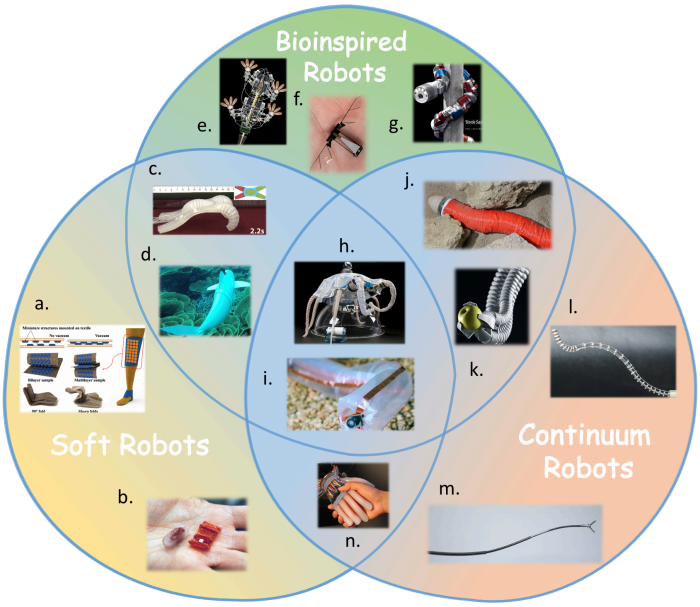


Figure 1.4: Examples of bioinspired robots, soft robots and continuum robots, classified by the whole shape forms. **a.** XoSoft wearable robot [108] **b.** degradable capsule origami robot [82] **c.** echinoderms inspired robot [120] **d.** SoFi soft robotic fish [80] **e.** bioinspired Stickybot [64] **f.** fly robot [145] **g.** Uncle Sam: snake-like robot [152] **h.** soft octopus robot [68] **i.** growing vinebot [16] **j.** plantoid robot [107] **k.** Festo elephant-trunk like robotic arm [34] **l.** tendon-driven continuum robot [89] **m.** concentric-tube robot [79] **n.** soft prosthetic hand [150]

to elegant robotic solutions, while "*from robots to insects*" suggests that robots as moving platforms are capable of testing biological hypotheses and could provide a possible explanation for the safe flying of insects in an unpredictable environment, thereby implying functions in the biological substrate.

When it comes to bioinspired robots, they should be associated with a cross-branch field – soft robotics, in which the robotic artefacts, as opposed to the conventional rigid counterparts, are inherently compliant for operation in an unstructured environment. Due to the use of soft materials [26, 150], soft actuators [80] and compliant structures and joints [68], such inherent or structural compliance endows robots with a variety of capabilities[69], such as squeezing(shortening), stretching(elongating), climbing, growing, and morphing, which rigid-link robots may not have.

Another branch that we are interested in is continuum robots, which are defined by [10] as "an actuatable structure whose constitutive material forms curves with continuous tangent vectors". Unlike rigid robots, which are constructed up of discrete links united by joints, the configuration of a continuum robot is dictated by an infinite-DOF elastic component. Thus, they could have continuous curvilinear struc-

tures at various scales: at large scales, such as Festo elephant-trunk [34] (Figure 1.4. **k.**), while at mini scales, like concentric-tube robot [79] (Figure 1.4. **m.**). Besides, the continuum robots can be categorized based on their actuation type (i. e., tendon/cable drive [68, 89], motors drive [107], EM drive [82], pneumatic drive [16], hydraulic drive [34], osmotic drive [124], shape memory effect [68], etc.) and structural design (i. e., single backbone, multi-backbone [89], concentric tube [79], etc.).

The three types of robots mentioned above are exemplified in the Figure 1.4. Bio-inspired continuum soft robots, as the overlap of these three, are emerging and attracting researchers' attention since they can shape at any point along the total length and adapt in complex morphologies by continuum elements to counteract unpredicted conditions (e. g., tendril-like soft robot [85]).

1.3 MOTIVATION AND OBJECTIVES

From the preceding, continuum structures are an indispensable and essential feature of biological and soft robotic systems. Such structures combine the typical characteristics of natural systems and can provide more intelligent solutions in a continuum mechanism with high compliance and adaptation when interacting with the external environment.

From the natural world, we chose the *passiflora* tendrils as the representation of ideal natural continuum structures, with focus on morphological changes resulting from mechanosensing. Many botanists investigated tendrils morphological changing capability focusing on their origin and development [129], flexibility property [140], and adaptive attachment [11] solely from a biological and biomechanical perspective. To this aim, different methodologies have been approached. Techniques such as histological analysis, in situ measurements of biological parameters, and micro-CT scans [63] are used most to study static morphological properties. However, few studies on the relationship between external stimuli (amount and duration of the exerted stimuli, the site of perception, etc.) and morphological changes have been conducted. Some of them were performed primarily around the 1890s ([9, 18, 19]) and most of these studies are qualitative of single-plane motions. Furthermore, they did not provide an analysis over time of the morphing in relation to external stimuli. The analysis required is particularly challenging in plants since they continuously grow following complex 3D patterns of movement. Image-based tracking methods could help to reinforce the motion analysis by providing more quantitative information. However, tracking plants' slender bodies poses several challenges to body recognition and reconstruction. A straightforward approach would be the use of markers along a moving body. This classic approach, however, has several limitations on its

applicability to plants. First of all, plants have continuously growing organs. It means that a new body part is always generated that cannot be marked in advance. Eventually, the position of markers on the body might impede the organ's movements. In addition, the added markers could be covered by leaves or other new growing sections of the plant body. To the best of our knowledge, until this thesis, no tool could analyze the evolution of tendril morphology upon external stimulation in three dimensions (details in Chapter 6).

In recent years, bio-inspired soft robotics have benefited from studing natural organisms, enabling dexterity and compliant structures for better adaptation, prompt response and safe interaction with the environment [69]. Continuum structures can shape at any point along the total length and adapt in complex morphologies to counteract unpredicted conditions.

Under a specific environmental context, the motion trajectory and workspace of continuum robots are determined not only by the end-effector, but also based on shape information whose kinematics cannot be described with traditional joint angles and link lengths. The measuring, modeling, and control of such kind of continuum geometry are still a challenge to date. Besides, there has been little discussion about the accurate reconstruction of slender, growing continuum structures, especially in thin size. The spatial description of such structures by an appropriate model can benefit the definition of shape configuration. In the literature, although the constant curvature hypothesis and piecewise constant curvature approximation have been adopted due to their simplicity and easy implementation [98], they do not dramatically correspond to continuous curling character – i.e., smooth transition between one straight line and one curve or between multiple curve segments.

From a very recent proposal in [90], we can see that taking inspiration from how nature has shaped continuum structures in animals and plants (e.g., their structural patterns, biomechanical properties, motion abilities) can help in designing more reliable artefacts with embodied functionalities (e.g., body-embedded reactive behaviors, morphing) that can simplify their control. Yet, biological information is underexploited due to a concerning lack of engagement from biologists. One of the reasons could be that there are limited available tools for observation and analysis.

1.4 CONTRIBUTION AND OUTLINE

The main contribution of this thesis is to propose an image-based marker-free approach associated with continuous model analysis (i. e., 2D and 3D Clothoid spirals) to provide the morphological description and reconstruction of natural thin-continuum shapes. We take tendrils of climbing plants as a biological model reference and analyze them

in 2D and 3D space. At the engineering level, it allows to description and reconstruction of artificial thin-continuum shapes and guides the design of tendril-inspired biomimetic intelligent devices.

This thesis will present a state-of-the-art survey on shape sensing and reconstruction of thin-continuum structures in Chapter 2, from model-based (i. e., kinematic and dynamics) to sensor-based and deepening to vision-based methods. Then, Chapter 3 introduces the essential theories of the clothoid spiral, the fundamental concepts of multi-view reconstruction and Fréchet distance that will be involved in subsequent chapters.

The main contributions of this thesis are subdivided into three chapters that tackle different dimensions (i. e., 2D and 3D), shape complexity (i. e., in-plane and off-plane) and data types (i. e., image and video):

I. 2D Shape Reconstruction *based on planar clothoid and piece-wise 2D clothoid curves*

Chapter 4 proposes two resolution approaches for the shape representation of both the natural tendril and artificial continuum structures: i) single-segment clothoid representation, with optimal curve parameters search; ii) piece-wise clothoid representation by assigned number of segments, with G^1 Hermite-fitting solution. Besides, we propose a novel algorithm to sort 2D unarranged points that addresses the issue of possible undesired branches and discontinuities in the skeletonized images.

Chapter 5 is the extension of the work in Chapter 4. We present an advancement of the sorting skeletonization algorithm, which can handle abrupt changes in the direction of the extracted points. In addition, we present an automatic method to identify the minimum number of 2D piece-wise clothoid spirals needed to represent a given tendril. This work allows us to properly describe the morphological evolution of a planar tendril after mechanical stimulation.

The main contributions of this part can be summarized as follows:

- at the engineering level, introduced and verified clothoid (piece-wise clothoid) curve can be used for shape representation of slender continuum structures with curling behaviors, including both natural and artificial ones;
- at the engineering level, proposed a 2D points-sorting algorithm for unarranged points;
- at the biological level, introduced a 2D practical tool to reconstruct temporal shapes and the morphology evolution of tendrils over time, and preliminary revealed the generated morphologies impacted by exerted stimuli with time and sensitive properties;

- at the biological level, analyzed the planar growth patterns to reveal the uneven distribution of the tendrils' sensitivity along the length.

II. 3D Shape Reconstruction *based on 3D piece-wise clothoid Curves*

Chapter 6 is based on the 2D work. First, it presents a stereo technique for shape reconstruction of 3D tendrils' morphology and the point correspondence relationship by using the minimum Fréchet distance between views. Then, it proposes an automatic piecewise 3D clothoid model to describe the reconstructed 3D tendrils.

The main contributions of this part can be summarized as follows:

- at the engineering level, presented a vision-based approach to reconstruct the 3D spatial shape of slender continuum structures from multi-view images;
- at the engineering level, proposed 3d piece-wise clothoid spirals to model and describe tendril shapes;
- at the biological level, introduced a 3D practical tool that can be adopted to characterize the morphological evolution over time of these organs organisms, in relation to the sensitive properties;
- at the biological level, analyzed the growth patterns to reveal the uneven distribution and transduction of the tendrils' sensitivity along the length.

Finally, Chapter 7 summarizes the relevant results of this work and provides the perspectives of future directions.

2 STATE OF THE ART

To target morphological analysis of biological continuum bodies, as well as the optimal shape control of continuum robots in well defined environments, shape sensing and 3D reconstruction are crucial steps.

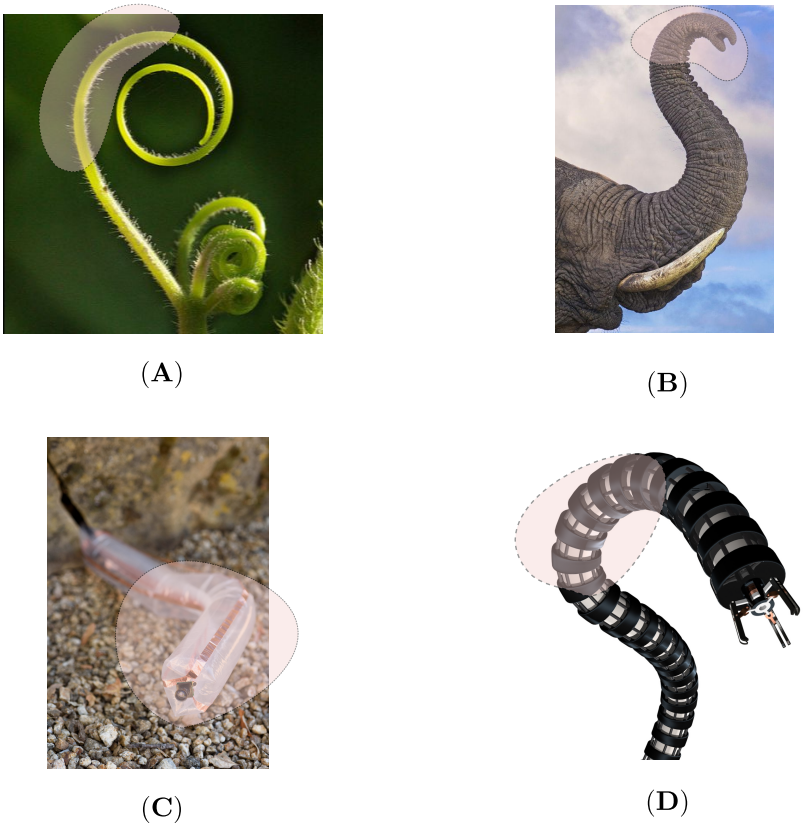
In this regard, there are a number of existing techniques, such as model-based, sensor-based and vision-based [111, 121, 138] methods, to provide shape sensing or reconstruction under different situations with advantages and disadvantages. Since a continuum structure has flexible, thin, and multi-directional movement, it requires approaches with fast response, high sensitivity and multi-dimensional measurements. For example, the model-based shape reconstruction can capture the kinematic and dynamics from both geometrical and physical properties. Still, it might fail with accuracy, demand for high complexity and thus high computational costs. The sensor-based shape sensing can provide portable and embeddable solutions but yet discrete components in continuum structures can introduce deviation in predictable behaviors. Meanwhile, vision-based sensing can directly measure the shape without complex mechatronics but using simple setups, e. g., RGB cameras. However, they are not easy to integrate into the bodies and still require solutions for efficient real-time 3D reconstruction.

In the following sections, I will review the state-of-the-art methods for shape sensing and reconstruction. The functionality, benefits, and limitations of each approach are discussed.

2.1 KINEMATIC-BASED SHAPE REPRESENTATION

Considering continuum structures, both the kinematic and dynamic models can address the shape reconstruction problem. A wide type of approaches are developed to describe natural structures, such as elephant trunks and tendrils, as well as continuum robots.

The most intuitive way to describe slender shapes is geometrical models. The differential geometry of framed curves can quantitatively describe the neutral axis of a slender object [128]. Typically, it can be divided into the parametric or non-parametric formulations of different curves, as reviewed in [123]. Given the continuum structure, as shown in Figure 2.1, the whole mechanism can divide into piece-wise segments for representation and modeling. In the following approaches, we only consider a sub-segment of the entire curve by piece-wise pattern.



(**A**) (**B**) (**C**) (**D**)

Figure 2.1: Examples of continuum structures both in nature and robotics. The partial slender mechanisms are circled inside the light red region. They are sensed and reconstructed with the methods reviewed in the following sections. (**A**) A plant tendril. (**B**) Elephant trunk. (**C**) Growing robot from [47]. (**D**) Tendon-driven continuum robot from [95].

2.1.1 *Rotation Frame Representation*

A generalized curve can be described in a rotation frame by a homogeneous transformation matrix, $\mathbf{T}(s) \in SE(3)$, as shown in Figure 2.2(A):

$$\mathbf{T}(s) = \begin{bmatrix} \mathbf{R}(s) & \mathbf{p}(s) \\ 0 & 1 \end{bmatrix} \tag{2.1}$$

The rotation frame $\mathbf{R}(s)$ is attached at the base of the piece-wise segment i, and connected with segment $i+1$. In [51], the authors defined the position vectors and orientation matrices by the following differential equations:

$$\begin{aligned} \frac{\mathrm{d}\mathbf{R}(s)}{\mathrm{d}s} &= \mathbf{R}(s)[\mathbf{u}(s)]_{\times} \\ \frac{\mathrm{d}\mathbf{p}(s)}{\mathrm{d}s} &= \mathbf{R}(s)\mathbf{v}(s) \end{aligned} \tag{2.2}$$

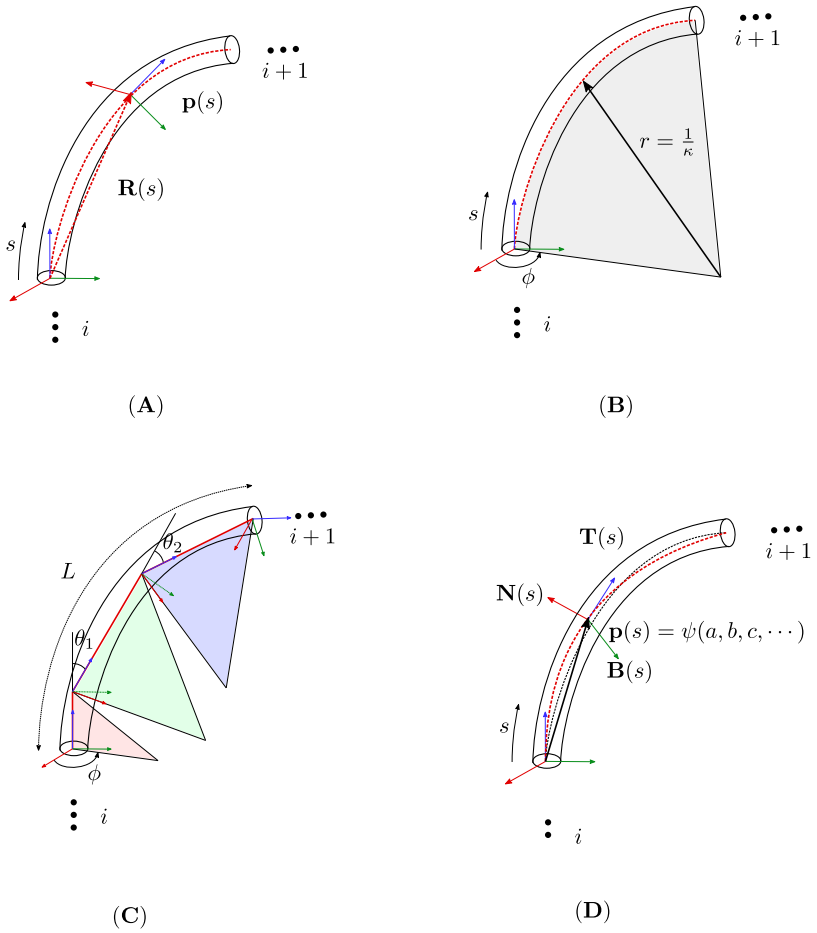


Figure 2.2: The illustration of different modeling approaches for piece-wise slender continuum structures. (**A**) Rotation frame representation with the position $\mathbf{p}(s)$ and the orientation matrix $\mathbf{R}(s)$ [51]. (**B**) The constant curvature model. (**C**) The pseudo-rigid body (PRB) model. (**D**) The distributed curve representation.

where $[\cdot]_\times$ is the skew-symmetric matrix of a vector from $\mathbb{R}^3$ to $\mathbb{SO}(3)$, and $\mathbf{v}(s)$ is the unit vector in the x, y and z directions. As long as the curve is assumed to be inextensible and shearless without axial deformation, we could get $\mathbf{v}(s) = [0, 0, 1]^T$. Meanwhile, $\mathbf{u}(s) = [\mathbf{u}(s)_T, \mathbf{u}(s)_N, \mathbf{u}(s)_B]^T$ a vector denoting an infinitesimal rotation of the attached frame.

2.1.2 *Constant Curvature Representation*

For simplification, the constant curvature [98] is the most used assumption of continuum shape approximation. It has been widely used for different types of continuum robots, such as the steering needle [99], soft manipulator [105], concentric tube [27], and tendon-driven manipulator [12, 132] etc.

As shown in Figure 2.2(B), to represent a point on the arc, the transformation matrix concerning the base frame can be given by:

$$\mathbf{T}(s) = \begin{bmatrix} \mathbf{R}_z(\phi)\mathbf{R}_y(\kappa s)\mathbf{R}_y(-\phi) & \mathbf{p}(s) \\ 0 & 1 \end{bmatrix} \tag{2.3}$$

where the point position is calculated as:

$$\mathbf{p}(s) = \begin{bmatrix} \frac{\cos\phi}{\kappa}(1-\cos\kappa s) \\ \frac{\sin\phi}{\kappa}(1-\cos\kappa s) \\ \frac{1}{\kappa}\sin\kappa s \end{bmatrix} \tag{2.4}$$

The curvature and bending angle are represented as:

$$\begin{aligned} \mathbf{k}(s) &= \sqrt{\kappa_x^2(s)+\kappa_y^2(s)} \\ \phi &= \arctan 2\left(\kappa_y, \kappa_x\right) \end{aligned} \tag{2.5}$$

However, it has been proved the approximation of a constant circular arc for most continuum structures will result in low accuracy [106, 112]. The drawback of this modeling method will introduce possible consequent deviation from the actual continuum mechanism. Despite this drawback, the constant curvature assumption remains primarily used because it reduces numerical complexity with respect to variable curvature models.

2.1.3 *Pseudo-Rigid Body (PRB) Representation*

In this formulation, the continuum structure is discretized into several segments, each acting as a rigid link. The connection between the segments can be assumed with torsion springs. This simplification allows the use of well-established classical rigid-body approaches. In [54, 100, 139], the Pseudo-Rigid Body (PRB) model was applied for both planar and 3D cases, as shown in Figure 2.2(C). Mathematically, the transformation between each link was performed by several consecutive rotations, which is given by:

$$\mathbf{T}_j(\gamma_j L) = \begin{bmatrix} \cos\theta_j & 0 & \sin\theta_j & \gamma_j L\sin\theta_j \\ 0 & 1 & 0 & 0 \\ -\sin\theta_j & 0 & \cos\theta_j & \gamma_j L\cos\theta_j \\ 0 & 0 & 0 & 1 \end{bmatrix} \tag{2.6}$$

Thus, after transform chain multiplication, the transformation matrix from the i^{th} sub-segment to the $i+1^{th}$ sub-segment will result as:

$$\mathbf{T}(L) = \mathbf{T}_z(\phi)\mathbf{T}_1(\gamma_1 L)\mathbf{T}_2(\gamma_2 L)\cdots\mathbf{T}_j(\gamma_j L)\mathbf{T}_z(-\phi) \tag{2.7}$$

It can be noticed that the rotation with z axis is denoted by $\mathbf{T}_z(*)$. The rotation by $-\phi$ can ensure no twist after the frame chain multiplication. This PRB representation has also been applied to different applications, such as catheters [42, 43, 139], tendon-driven continuum manipulators [93]. It has to be noticed that with the PRB-type models, the dynamics can be easily obtained using classical multibody Equations of Motions (EOM).

2.1.4 *Distributed Curve Representation*

Another way to describe the slender structure is using a finite number of distributed curves. It is expressed in curve parameters or a set of "modal" shape functions. The kinematics is formed with a linear combination of shape functions. The general form can be represented by:

$$\mathbf{C}(s) = \sum_{i=1}^{N} a_i \mathbf{\Phi}_i(s) \tag{2.8}$$

where a_i is the i^{th} coefficient and $\mathbf{\Phi}_i(s)$ is the respective shape function. The number of curve parameters depends on the specific modeling of shape functions. In general, it is selected by trigonometric functions such as $\sin(*)$ and $\cos(*)$, and approximated with a truncated Fourier series [88]. Some other forms of functions can also be expressed, such as polynomials [39], Taylor series expansion [40], Bézier curves [125, 147], PH curves [123], variable curvatures [78] and approximation of curvature as polynomial [14, 112].

2.2 DYNAMICS-BASED SHAPE REPRESENTATION

The dynamics model can reveal the internal mechanics and force relationships, as well as boundary conditions, including external forces, contacts etc. In particular, the deformation can be viewed as a beam backbone for slender structures. It can capture the shape information characterized by the non-linear mechanics in 3D space. In this section, two typical dynamics models will be introduced for shape representation, as shown in Fig. 2.3.

2.2.1 *Cosserat Rod Representation*

Classically, when referring to the mechanics of slender structures, the Cosserat rod theory [38] is applied to describe the shape deformation. A set of differential equations are needed to build and solve Boundary Value Problems (BVP). Different physical effects are integrated by taking advantage of bending, shearing and extension constraints. Many works have been done for modeling and control of continuum robots

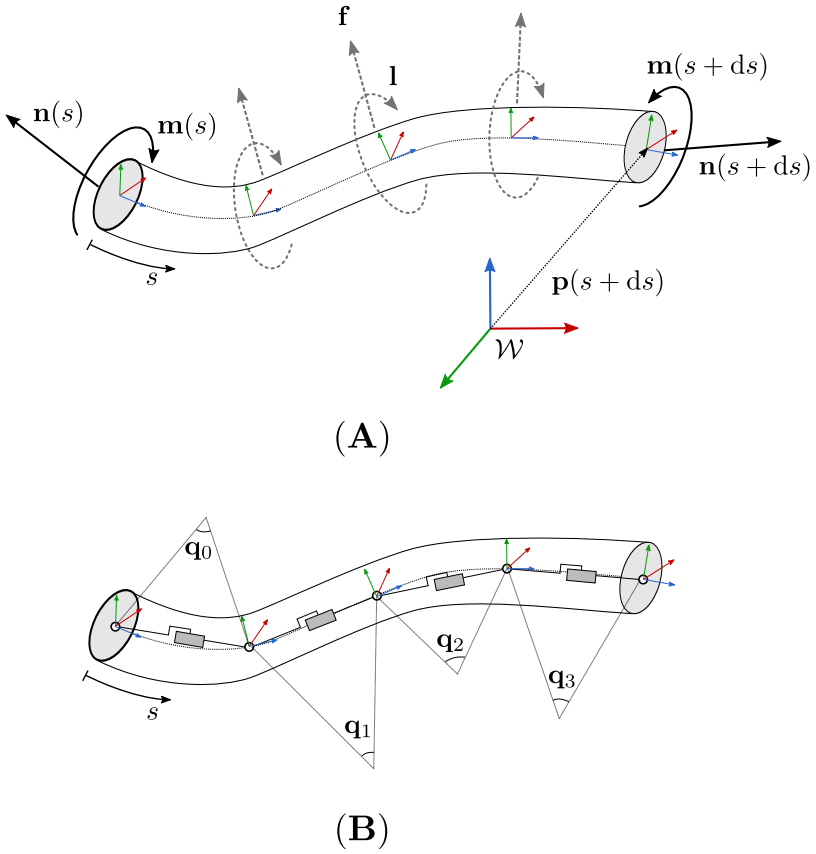


Figure 2.3: The illustration of two typical dynamics modeling approaches for the piece-wise slender continuum structures. (**A**) Cosserat rod representation. (**B**) Lumped multi-body representation, with a sequence of Revolute-Prismatic-Revolute Joints (RPR) joints.

[59, 87, 97, 132]. Taking the notation from [10] and shown in Figure 2.3(A), the quasi-static equilibrium form can be represented by a set of differential equations:

$$\begin{aligned} \partial_s \mathbf{n} + \mathbf{f} &= 0 \\ \partial_s \mathbf{m} + \partial_s \mathbf{p} \times \mathbf{n} + \mathbf{l} &= 0 \end{aligned} \tag{2.9}$$

where $\mathbf{n}$ and $\mathbf{m}$ are the internal force and moment interpreted at the curve length s. Meanwhile, $\mathbf{f}$ and $\mathbf{l}$ are the distributed force and moment applied externally.

The calculation of $\mathbf{n}$ and $\mathbf{m}$ is algebraically related to material constitutive law. For the tendon-driven robotic system, the internal force and moment of $\mathbf{n}$ and $\mathbf{m}$ are also affected by the boundary conditions, i.e., the coupled tendon termination. The 3D static model for continuum robots can be found in [97, 103].

More details about non-neglectable linear and angular momentum can be found in [38]. The mass density ρA, the mass moment of inertia $\rho \mathbf{J}$, and angular momentum $\rho \mathbf{J} \omega$ variables are accounted for each cross-section of the rod, especially for complex geometric features.

2.2.2 *Lumped Multi-body Representation*

As described in the previous section, a curve can be discretized into multiple segments. It can be viewed as a classical multi-body dynamic system with constraints. For example, the body can be augmented with multi-segments, which could be composed as a sequence of RPR joints, shown in Figure 2.3(B). The general form of equations of motion (EOM) is given by:

$$\mathbf{M}(\mathbf{q})\ddot{\mathbf{q}} + \mathbf{C}(\mathbf{q}, \dot{\mathbf{q}})\dot{\mathbf{q}} + \mathbf{N}(\mathbf{q}, \dot{\mathbf{q}}) = \mathbf{B}(\tau) \tag{2.10}$$

where $\mathbf{q}$, $\dot{\mathbf{q}}$, $\ddot{\mathbf{q}}$ are the robot configuration and its derivatives. $\mathbf{M}$ is the inertia matrix, $\mathbf{C}$ is the Coriolis and centrifugal matrix, and $\mathbf{N}$ is the gravity. The non-conservative term $\mathbf{B}$ is associated with generalized actuation and external forces.

It has to be noticed that in order to capture the motion with equations of rigid-body forms, some approximations need to be assumed. In [23, 62], the authors proposed the dynamically consistent augmented formulation by introducing an equivalent Denavit-Hartenberg Parameters (DH) parameterization. Each curve sub-segment's The Center of Mass (COM) is matched with an equivalent point mass in the approximated rigid-link model.

Similarly, the Center of Gravity (COG) based dynamic model is proposed in [41]. Both linear and angular kinetic energies are derived at the COGs. Through solving the integrated energy functions, the EOM terms can be obtained recursively. They also showed the efficient real-time performance numerically for a three-section continuum model.

Different from the Cosserat-rod in continuous form, the discretized approximation requires a large number of segments to guarantee accuracy. Usually, the parameterized spring, dampers and lumped masses must be identified regarding a continuum system. Although several other approaches formulated static force equilibrium [148], a lumped set of equations are still needed. Therefore, it will introduce more computational complexity. A reliable and accurate Matlab package has been developed for discretized lumped and reduced-order continuum models in [106].

2.3 SENSOR-BASED SHAPE REPRESENTATION

In addition, sensors can measure the deformation information as well. As an alternative to model-based strategies, the use of sensors on a physical body can allow its shape real-time measurement and estimation without requiring complex shape modeling. In recent years, the advancement of fabrication techniques has boosted various types of sensors, each with its challenges, pros and cons. Two important categories of sensors developed in the literature are fiber optical and

electromagnetic-based sensor, providing advancement in proprioception capabilities for soft continuum systems.

2.3.1 *Fiber Optical-based Sensor*

An optical fiber is a technology that transmits information in the form of light pulses and intensity along a glass, plastic or silicon fiber, given a light transmitter and a receiver. This technology can be used as sensors and embedded in soft continuum structures to detect shape deformations (strain and curvature) by looking at variations in the intensity, phase, polarization, and wavelength of the transmitted light. In general, intensity-modulated [113, 149], phase-modulated [153], and scattering-based [36] methods are applied for shape reconstruction.

Among these types of sensors, the Fiber Bragg Gratings (FBG) sensors [99] are extensively studied. The fabrication techniques of FBGs include photosensitivity, holography, phase masking, and a femtosecond laser. The reflected Bragg wavelength shifts with strain and temperature. The shift is measured using an interrogation system to characterize the FBG response. The strain, curvature and torsion along the continuum body are directly related to the wavelength shift on each fiber. The FBGs provide advantages with a more extended working range, miniature size, fast response, high sensitivity and repeatability. Therefore, the curvature and torsion features can be suitable for shape detection and estimation in many applications. It has been applied to different types of continuum robots, such as tendon-driven manipulators [2], steerable catheters [15], concentric-tube robots [24], soft material robots [36, 143], needles [92], etc. Regarding the integration of fibers, both straight [118] and helical [144] configurations are evaluated. Thus, it could provide additional measurements, such as elongation and compression [50]. It should also be noted that the ability for torsion and force sensing can also be found in several works [15, 94, 142, 146].

In conclusion, the fiber optical-based sensor, particularly the FBG-based, is a promising approach for the shape reconstruction of slender structures. The measurement benefits from the millimeter-level diameters of the fibers. However, the sensor is more accurate regarding small deflections due to a lower strain transfer ratio. The stretchability of the sensor would be limited for more significant deformation of the C-shape and S-shape. To improve the performance, the design and configurations should be optimized for setups, such as the number of fibers, fiber core numbers, reducing induced strain on the fibers, etc.

2.3.2 *Electromagnetic-based Sensor*

Another method relies on measuring the deployed physical sensors' position and orientation within the detected objects. One representa-

tive sensor of this type is the electromagnetic (Electromagnetic (EM)) tracking system. Due to its advantages of real-time performance, size miniaturization and accuracy, it has been widely used in many applications, such as surgical navigation [136], control of continuum robot [61] and soft robot [71], and reconstruction of intravascular catheterization interventions [122]. The functional principle is to use a pre-generated electromagnetic field to measure the pose of the EM receivers within a known workspace. Compared to FBG-based sensors, it has greater flexibility over large deformation and freedom from line-of-sight. More importantly, they have no effect on the mechanical properties of the robots, which will be beneficial for modeling and control.

However, only a few sensors can be discretely attached to the objects, e. g., at the end-effector for distal tip tracking. As a result, only discrete posture information can be captured, which is the primary drawback of this technique. To reconstruct the entire shape, it has to combine with other approaches, such as the robotic kinematic models. For example, in [133], the authors extended a Kalman filter to combine data from EM trackers with kinematic models and determine the robot's motion. Similarly, probabilistic fusion was applied to the biopsy needle [109] and catheters [25, 37]. Most of these works configured the EM trackers only at key points of the body frame, such as at the tip and the base. The fusion technique can estimate the shape parameters using measured curvature information. By mounting three EM sensors along a cable-driven continuum robot [126], the shape reconstruction is performed by fitting cubic or quadratic Bezier curves based on the robot section length and the pose data obtained from EM tracking. With this hybrid approach, shape reconstruction remains an estimation that might fail in accuracy.

Apart from discrete setups, EM sensors are limited by measurement inaccuracies due to the distortion of the magnetic field induced by magnetic and conductive objects. Therefore, the interference generated by electronic and metal instruments in the workspace would reduce the effectiveness and reliability of EM tracking. For this, a calibration procedure with a motion model using EKF-SLAM (simultaneous localization and mapping) was proposed in [110] for dynamic field distortion compensation. A motion model based on observations from redundant EM sensors was developed to achieve dynamic field distortion compensation via real-time distortion mapping, allowing for simultaneous localization and calibration. Meanwhile, measurement accuracy is limited in a small workspace, where high and uniform accuracy is concentrated in the tracking volume's center. To improve the performance, [96] developed an EM servoing control paradigm for centering the field generator using a robot manipulator.

In addition to the shape reconstruction function, the contact force was estimated combined with the Cosserat-rod theory by using EM

tracking [104]. It can therefore benefit other sense modalities as well. In recent years, commercial EM tracking systems have been developed, such as the NDI Aurora [86]. Numerous applications can benefit from their diverse sorts of sensors. In terms of sensor configuration, an EM tracker can be equipped on the objects either externally or internally [127, 151].

2.4 VISION-BASED SHAPE REPRESENTATION

Shape sensing based on computer vision has become increasingly popular in recent years. They rely on image data, which is easy to obtain and inexpensive, to monitor and infer the geometry of objects. Typically, this approach requires no major hardware modifications and integration over the detected objects. In the literature [91], many approaches to shape reconstruction for a general object have been proposed. In general, most of these works characterize the reconstruction with a finite set of points or geometry features (such as contours, boundaries of the surface, edges) in 2D images by outputting 3D parameterized shapes such as curves, polygons, etc., or non-parameterized shape such as meshes. Stereopsis is the fundamental theory governing the multi-view source of images. Most dense reconstruction techniques have difficulties with thin, long, or slender constructions.

In particular, for thin structures, curve skeletons, which are 1D structures, are frequently used to abstract the topology and geometry of 3D shapes. [73] used a deformable primitive to break down the detailed surface into a multi-layer set of 1D curves. Similarly, in [53], the 3D point cloud is represented as a curve skeleton without prior assumptions on the shape geometry or topology. In conclusion, creating an efficient technique for calculating a generalized skeleton representation for a thin-structured object is essential. To significantly increase the utility of the curve skeleton, such a skeletonization approach should be able to accept general input beyond the closed surface, such as point clouds or images directly. Therefore, the detection of edges, curves and lines in images is essential for sparse abstractions. [130] proposed a probabilistic formulation of reconstruction based on multiple calibrated 2D views. The reconstructed curve lies at the intersection of a set of image distributions. More fundamentally, the authors proposed a reconstruction framework based on differential geometry of general curves [29]. The curve tangent, curvature, curvature derivative, and torsion of a space curve are derived for a pair of stereo images. Additionally, the differential curve motion is estimated according to the camera motion. Further, it was extended by representing the topological connectivity of image curves with a 3D graph in [134]. A novel technique for reconstructing continuous 3D wires using a set of image curve segments is investigated in [77]. The cubic B-spline

is used to parameterize the curve shape. And a global optimization algorithm is developed to solve the view correspondence problem concerning smoothness. Apart from only using image information, the physical simulation of the rod was exploited for the reconstruction of thin tubular structures [81]. Some extension works have been applied for surface reconstruction using curves in [74, 135].

While the above methods explore similar characteristics of thin objects, they fundamentally focus on general object reconstruction within the computer vision and graphics field. Only a few papers use vision-based approaches to solve the reconstruction for slender/thin structures, such as continuum robots and plant tendrils. In [17], a reliable and effective stereo-vision-based shape detection technique is presented for continuum robots. The Self-Organizing Map (SOM) structure was applied to approximate the shape curve from segmented 2D images. The closed-loop shape control can be developed according to the reconstruction as image feedback. The real-time 3D reconstruction of continuum robots based on two arbitrary camera views is proposed in [20]. It is based on a closed-form analytical solution of quadratic curves in 3D space. In the meanwhile, segmentation and feature extraction are developed at high-speed image processing algorithms. In [102], the technique makes use of the catheter robot's differential kinematic models in combination with optical flow analysis of the images. The mask shape of the catheter in 2D images is optimized using the particle swarm algorithm. In [32], instead of direct modeling with the shape, the eye-in-hand visual servoing framework is proposed by a local Gaussian process regression for inverse mapping. The 3D shape of the flexible robot is reconstructed by minimizing an energy function in [137]. The model is based on a graph allowing for the displacement of the shape's constituent points over the entire 3D space.

In medical robotics, the source of images varied from endoscopic to X-ray/MRI/CT images. Thus, several different approaches have been proposed for continuum robots for these specific images, such as fluoroscopy, endoscopy, and ultrasound. The detailed approaches in this category will not be reviewed here because they are not particularly interesting to us. The related view papers can be found in [121, 138].

2.4.1 *Summary*

In conclusion, the advantages, disadvantages and applications of shape sensing techniques for slender continuum structures are summarized in Table 2.1 and Table 2.2.

The model-based technique for shape reconstruction from these two tables lies in two parts. One is based on kinematics, which mainly introduces three approaches: the constant curvature assumption is simple, and the most used but with low accuracy; the PRB equals to

the piecewise rigid body, lacking continuity; the distributed curve is a more accurate approximation depending on the characteristics of different curves – variable curvature – appropriate to describe the continuous shape. The other is based on dynamics, Cosserat Rod and lumped multi-body, considering the integration of bending, torsion, shearing and extension of physical strain to reflect dynamics physical properties of elastic, material and external force, etc. The complexity of modeling, computation and form is obviously high. Sensor-based approaches mainly introduced FBG and EM. They both are in mini size, easy to be integrated along the body, and able to realize real-time response. FBG sensors are extremely expensive, and their accuracy is limited to C-shape and S-shape. While EM sensors are more flexible over large deformation but have high requirements for workspace. Vision-based approaches are affordable, simple to deploy the setup and able to obtain direct shape measurements.

The combination of vision and nonlinear curve model approach is a promising solution for the reconstruction of thin, slender continuum structures and will be detailed in depth in the following chapters, where it is applied for the shape reconstruction of tendrils.

Sensing	Model-based Approach				
Categories	Kinematic-based			Dynamics-based	
Methods	Constant Curvature	Pseudo-Rigid Body (PRB)	Distributed Curve	Cosserat Rod	Lumped Multi-body
Advantages	• simple • direct transformation from actuation and end-effector pose	• piece-wise model equivalent to classical rigid body • possible to obtain dynamics by multi-body EOM	• more accurate approximation • able to describe variable curvature shapes	• integration of bending, torsion, shearing and extension to reflect elastic physical effects • continuous form related to material constitutive law • reflecting dynamics regarding force and torsion	• direct linkage to the generalized actuation and external forces, such as gravity, tension, etc. • solver for multi-body EOM using classical libraries
Constraints	• low accuracy • needs complex transformation calculation for multi-segments	• low accuracy • lumped parameters increase computation complexity	• needs optimization approach to fit the distributed parameters • intensive computation complexity	• complexity of mathematical modeling • high computation load • lacking analytical solution for Partial Differential Equation (PDE)-form motion equations	• discretized approximation reduced accuracy • requires large-sized segments which increases computation complexity
Applications	• steering needle [99] • soft manipulator [105] • concentric tube [12, 27, 132]	• catheters [42, 43, 139] • tendon-driven continuum manipulator[93]	• continuum robot [40, 147] • tendon-driven flexible robot [14, 125] • pneumatic robotic arm(Festo's Bionic Handling Assistant) [78, 123]	• tendon-driven robot [103] • parallel continuum robot [132] • pneumatic or hydraulic robotic finger [132] • multi-segments soft manipulator[59, 97]	• pneumatic soft robotic arm [23] • multi-segments continuum arm [41] • hybrid rigid-flexible robot [106]

Table 2.1: The comparison over advantages, constraints and applications regarding different sensing techniques.

Sensing	Sensor-based Approach		Vision-based Approach
Methods	Fiber optical-based (FBG)	Electromagnetic-based (EM)	Vision-based
Advantages	• able to be integrated along body for strain, curvature, torsion and force sensing • long working range • miniature size • fast response • high sensitivity and repeatability	• real-time performance • miniature size • high accuracy within workspace • more flexibility over large deformation and freedom from line-of-sight • could be equipped on the object either externally or internally	• able to direct measure of the shape without complex mechatronic setups • no need to modify the integration of the detected object • cheap and affordable
Constraints	• accuracy limited for larger deformation of C-shape and S-shape due to limited stretchability • expensive for integration	• discretized sensory information for pose estimation, such as keypoints • whole shape reconstruction must be combined with other data, such as kinematic models • receivers must be deployed within known workspace by a pregenerated electromagnetic field • measurement accuracy limited in a small workspace • interference effect induced by magnetic and conductive object significantly	• needs complex implementation of computer vision algorithm • accuracy is limited by imaging quality
Applications	• tendon-driven manipulators [2] • steerable catheter [15] • concentric-tube robots [24] • soft material robots [36, 143] • needles [92]	• surgical navigation [136] • continuum robot [61] • soft robot [71] • intravascular catheters [122]	• wire art [77] • surgical continuum robot [17, 102, 137] • soft manipulator [32] • catheter [20]

Table 2.2: The comparison over advantages, constraints and applications regarding different sensing techniques.

Part II

THEORY

3

CURVE MODELING AND RECONSTRUCTION

This chapter is the foundation for the following chapters. First, it introduces the essential theories on the clothoid curve in the plane and the space form separately. Then, the multi-view reconstruction is presented. Finally, the Frèchet distance for the similarity of curves is introduced.They are the bricks for constructing the methodologies in the following chapters.

3.1 CLOTHOID CURVE

The Clothoid curve has been given several names throughout its history, including "*Euler spiral*," "*Cornu spiral*," "*Spiro curve*," and "*Glover's spiral*." These specific names have witnessed the fact that the investigation of the curve has gone through several different stages, and each term originated from a completely distinct application [72]. First, *as the definition for an inverse problem of elastic springs with pre-curved shape.* It was proposed by James Bernoulli in 1694. Next, *as a graphical computation method for light diffraction patterns.* Around 1818, Augustin Fresnel independently derived the correspondent integrals (later known as Fresnel integrals) for the principle of light, which is equivalent to the definition of the clothoid by mathematical transformation. Later, Alfred Marie Cornu precisely plotted the spiral of the Fresnel integrals. Finally, *as an engineering problem for railway track design.* Arthur Talbot, in his work "The Railway Transition Spiral", introduced a transition curve to ensure a smooth riding experience and derived exactly the same integrals as the aforementioned.

Recently, this transition curve has been applied in various fields, such as in computer graphics for font design, roller coaster design; in autonomous driving for optimal trajectories planning and following [67]; in medicine for the reconstruction of elastin fibers in vascular models [66]; in robotics for continuum structure reconstruction [30, 31].

3.1.1 *Definition*

According to Alfred Gray [1], the clothoid is "one of the most elegant of all plane curves." It forms the curve whose curvature grows linearly with the arc length. When the curvature is signed, a clothoid is odd symmetric with regard to an inflection point, displaying a double spiral structure.

In parametric form, a general 2D clothoid curve is given by the differential equations as follows:

$$\begin{aligned} x'(s) &= cos(\alpha(s)), & x(0) &= x_0 \\ y'(s) &= sin(\alpha(s)), & y(0) &= y_0 \\ \alpha'(s) &= \mathcal{K}(s), & \alpha(0) &= \alpha_0 \\ \alpha(s) &= \frac{k_1}{2}s^2 + k_2 s + \alpha_0 \end{aligned} \tag{3.1}$$

where $\alpha(s)$ is the direction (angle) of the tangent curve $(x'(s), y'(s))$ at point $(x(s), y(s))$ with respect to the arc length parameter s.

According to [7], the solution of the above ODE function is:

$$\begin{aligned} x(s) &= x_0 + \int_0^s \cos\left(\frac{1}{2}k_1\tau^2 + k_2\tau + \alpha_0\right) \mathrm{d}\tau \\ y(s) &= y_0 + \int_0^s \sin\left(\frac{1}{2}k_1\tau^2 + k_2\tau + \alpha_0\right) \mathrm{d}\tau \end{aligned} \tag{3.2}$$

where x_0, y_0 are the origin of the clothoid curve.

The curve has a characteristic that the curvature is an affine(linear) function of arclength as:

$$\mathcal{K}(s) = k_1 s + k_2 \tag{3.3}$$

Note that, there are two special cases: when $k_1 = 0$, the curve is a circle, and when $k_1 = k_2 = 0$, the curve is a straight line. This affine property allows a smooth transition between straight line and curve segments.

3.1.2 *Fresnel Integrals*

In terms of the traditional Fresnel integrals, the above ODE solution can be reformulated as in [7]. The Fresnel integrals are defined through the following equations:

$$\begin{aligned} \int_0^s \xi^k cos(\frac{a}{2}\xi^2 + b\xi + c)\ \mathrm{d}\xi &= s^{1+k}\mathbb{X}_k(as^2, bs, c) \\ \int_0^s \xi^k sin(\frac{a}{2}\xi^2 + b\xi + c)\ \mathrm{d}\xi &= s^{1+k}\mathbb{Y}_k(as^2, bs, c) \end{aligned} \tag{3.4}$$

where

$$\begin{aligned} \mathbb{X}_k(p, q, r) &= \int_0^1 \xi^k cos(\frac{p}{2}\xi^2 + q\xi + r)\ \mathrm{d}\xi \\ \mathbb{Y}_k(p, q, r) &= \int_0^1 \xi^k sin(\frac{p}{2}\xi^2 + q\xi + r)\ \mathrm{d}\xi \end{aligned} \tag{3.5}$$

According to [7], Equation 3.5 defined as Fresnel integral momenta, can be calculated accurately with defined parameters. It is based on the asymptotic expansions with Lommel function. A Matlab/C++ library has been provided for numerical computation in [5].

Therefore, the solution of ODE in Equation 3.1 are derived by:

$$\begin{aligned} x(s) &= x_0 + s\mathbb{X}_0(k_1 s^2, k_2 s, \alpha_0) \\ y(s) &= y_0 + s\mathbb{Y}_0(k_1 s^2, k_2 s, \alpha_0) \end{aligned} \tag{3.6}$$

3.1.3 *Fitting of a Clothoid*

Definition 3.1.1 (G^1 Hermite Interpolation)**.** Given two points (x_0, y_0), (x_1, y_1), and two angles α_1 and α_2, find a clothoid curve segment in form of Equation 3.6 that satisfies the following boundary conditions:

$$\begin{aligned} x(0) = x_0, \;\; x(L) = x_1, \;\; x'(0) = \cos(\alpha_0), \;\; x'(L) = \cos(\alpha_1) \\ y(0) = y_0, \;\; y(L) = y_1, \;\; y'(L) = \sin(\alpha_0), \;\; y'(L) = \sin(\alpha_1) \end{aligned} \tag{3.7}$$

where L is the curve length.

As discussed in [7], the G^1 Hermite interpolation problem may have an infinite number of solutions. Actually, the curve can be found as long as the curve satisfies $\alpha(0) = \alpha_0 + 2k\pi$ and $\alpha(L) = \alpha_1 + 2l\pi$, with $k, l \in \mathbb{Z}$.

Regarding our topic, the goal is to represent the 3D continuum shape with clothoid segments. Consequently, the G^1 solution fits our single-segment fitting problem quite well. It guarantees there is at least one single curve can be obtained, which can be optimized using our following proposed algorithm, as detailed in Chapter 4.

3.1.4 *Construction of a Clothoid Segment*

From the above definition of the clothoid, we can define a clothoid basis as a curve primitive. Then, we can conclude the following pipeline for construction of a general clothoid segment shape with the curve primitive as,



$L = 10$	k_1	k_2
A.	0	0
B.	0.01	0.01
C.	0.05	0.01
D.	0.08	0.01
E.	0.12	0.02
F.	0.18	0.08

Figure 3.1: The illustration of a series of Clothoid curves with different parameters

- define the origin point $(x_0, y_0) = (0, 0)$, the initial angle $\alpha_0 = 0$, the curvature parameters k_1, k_2, and the curve length L
- compute the curve ODE using Equation 3.6 for curve length $[0, L]$
- Trim the curve segment by bounding the curve length with $[l_1, l_2]$, where $l_1, l_2 \in [0, L]$
- perform `translate` $(\mathcal{T})$, `rotate` $(\mathcal{R})$, `scale` $(\mathcal{S})$ to obtain a transformed curve segment

The examples of the clothoid and their transformed curve segment regarding different parameters is shown in Figure 3.1 and Figure 3.2, respectively.

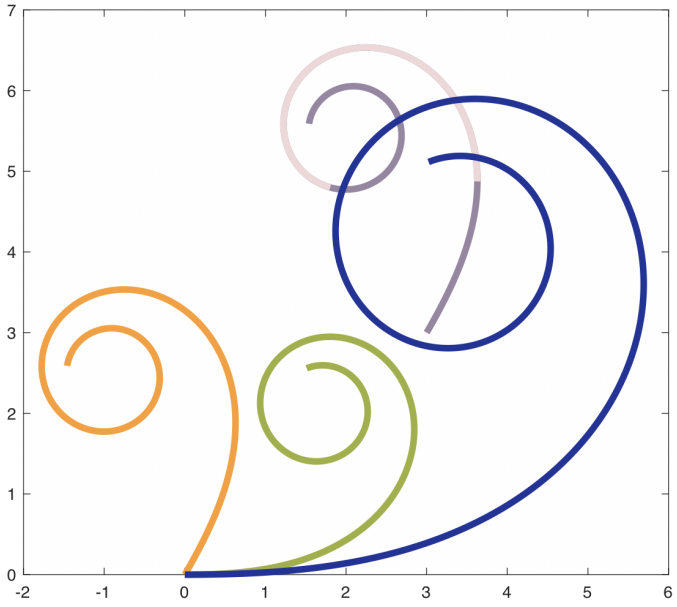


Figure 3.2: The illustration of Clothoid curves with different transformations: original curve (green), translated curve (purple), rotated curve (orange), scaled curve (blue), trimmed curve (pink).

3.1.5 *3D Representation of Clothoid*

The first attempt to extend the 2D planar clothoid spline to 3D space was proposed in [44] . Given an initial polygon under the TNB frame, an iteration algorithm is proposed to refine the polygon by introducing the discrete curvature binormal vector to determine inserted vertices and ensure the curvature linearly distributed on each edge and vertex. However, this study only considers the curvature and ignores the

other essential factor regarding the 3D curve, i. e., torsion. Meanwhile, this approach can only generate 3D discrete clothoid splines. In work [46], Harary et al. define a new type of 3D clothoid curve without a predefined polygon, which considers both curvature and torsion and assures their linearity characteristics. It can produce continuous rather than discrete clothoid spirals for 3D curve completion in terms of continuous differential geometry.

In order to take into consideration the torsion, an affine relationship similarly as Equation 3.3 can be given as:

$$\mathcal{T}(s) = \tau_1 s + \tau_2 \tag{3.8}$$

According to [46], the following definition can be given for 3D clothoid with a set of differential equations in TNB frame.

Definition 3.1.2 (3D Clothoid Curve)**.** The 3D clothoid curve $\mathcal{C}(s)$ fulfills Equation 3.3, Equation 3.8 and the initial following conditions:

$$\begin{aligned}
&\frac{\mathrm{d}\mathcal{C}(s)}{\mathrm{d}s} = \mathbf{T}(s) \\
&\frac{\mathrm{d}\mathbf{T}(s)}{\mathrm{d}s} = (k_1 s + k_2)\,\mathbf{N}(s) \\
&\frac{\mathrm{d}\mathbf{N}(s)}{\mathrm{d}s} = -(k_1 s + k_2)\,\mathbf{T}(s) + (\tau_1 s + \tau_2)\,\mathbf{B}(s) \\
&\frac{\mathrm{d}\mathbf{B}(s)}{\mathrm{d}s} = -(\tau_1 s + \tau_2)\,\mathbf{N}(s) \\
&\mathcal{C}(0) = \mathbf{c}_0,\ \mathbf{T}(0) = T_0,\ \mathbf{N}(0) = N_0,\ \mathbf{B}(0) = T_0 \times N_0
\end{aligned} \tag{3.9}$$

It has been proved in [46], the 3D clothoid have the following properties,

- **Invariance to similarity transformations** : translation, rotation, and scaling
- **Symmetry** : the starting point $\mathbf{c}_0$ and end point $\mathbf{c}_L$ can be switched
- **Extensibility** : a curve segment between $\mathbf{c}_m$ and $\mathbf{c}_n$ coincide with $\mathcal{C}$, where $m, n \in [0, L]$
- **Smoothness** : The tangent, i.e., $\frac{\mathrm{d}\mathcal{C}(s)}{\mathrm{d}s}$ at each curve point is finite.
- **Roundness** : $\mathcal{C}$ is a circle if it interpolates two point-tangent pairs that are on a circle.

The above properties guarantee the unique existence of a 3D clothoid curve. It can be used with our three-dimensional model of the slender continuum structure in terms of curvature and torsion linearity. For our algorithm presented for reconstruction, we reformulated the 3D curve into a discrete representation with the above Frenet-Serret equations. More details can be found in the Section 6.4.

3.1.6 *Piecewise Integration*

Principally, the clothoid spiral satisfies a function that penalizes the curve's change in curvature (in the 2D case) and torsion (in 2D and 3D cases). An energy cost can be evaluated according to $\mathcal{K}$ and $\mathcal{T}$:

$$\mathbf{E}(\mathcal{K}, \mathcal{T}) = \int \left(\frac{\mathrm{d}\mathcal{K}}{\mathrm{d}s}\right)^2 + \left(\frac{\mathrm{d}\mathcal{T}}{\mathrm{d}s}\right)^2 \mathrm{d}s \tag{3.10}$$

In fact, the solution minimizes the L_2-norm of the variation of curvature and torsion. As referred to for 2D curves, the variation of curvature is known as MVC (or minimum variation curve) [83]. It is also the curve that minimizes the L_∞-norm of the curvature variation, subject to endpoint constraints.

Suppose the above curve is discretized into several piece-wise clothoid spiral segments. Then, the G^2-continuity can be guaranteed. There are endless solutions available if the endpoints are not subject to any additional constraints. Thus, we proposed an approach with optimization over the number of segments in our subsequently developed algorithm for the 3D piece-wise reconstruction. The definition of G^2 Hermite Interpolation problem is given as follows. It should be noted that the $u(s)$ inside the definition can be interpreted as an optimization or a control variable.

Definition 3.1.3 (G^2 Hermite Interpolation)**.** Given two points (x_0, y_0), (x_1, y_1), and two angles α_1 and α_2, and two curvatures $\mathcal{K}_0$ and $\mathcal{K}_1$, find a clothoid curve segment in the form of Equation 3.9 that satisfies the following boundary conditions:

$$\begin{aligned} &x(0) = x_0, \;\; x(L) = x_1, \;\; x'(0) = \cos(\alpha_0), \;\; x'(L) = \cos(\alpha_1) \\ &y(0) = y_0, \;\; y(L) = y_1, \;\; y'(L) = \sin(\alpha_0), \;\; y'(L) = \sin(\alpha_1) \\ &k_1 = u(s), \;\; \mathcal{K}(0) = \mathcal{K}_0, \;\; \mathcal{K}(L) = \mathcal{K}_1 \end{aligned} \tag{3.11}$$

where L is the curve length, and $u(s)$ is a piece-wise constant function to be determined.

3.2 MULTI-VIEW RECONSTRUCTION

The process of estimating the 3D structure of a scene from a set of 2D images is called multi-view reconstruction. In our case, we consider n pinhole cameras to observe a set of curve points, as shown in Figure 3.3.

3.2.1 *Camera Projection Model*

A 3D point $\mathbf{p} \in \mathbb{R}^3$ in the regular world frame ${}_r\mathcal{W}$, observed by a camera at position $\mathbf{t} \in \mathbb{R}^3$, with orientation $\mathcal{R} \in \mathbf{SO(3)}$ and intrinsic

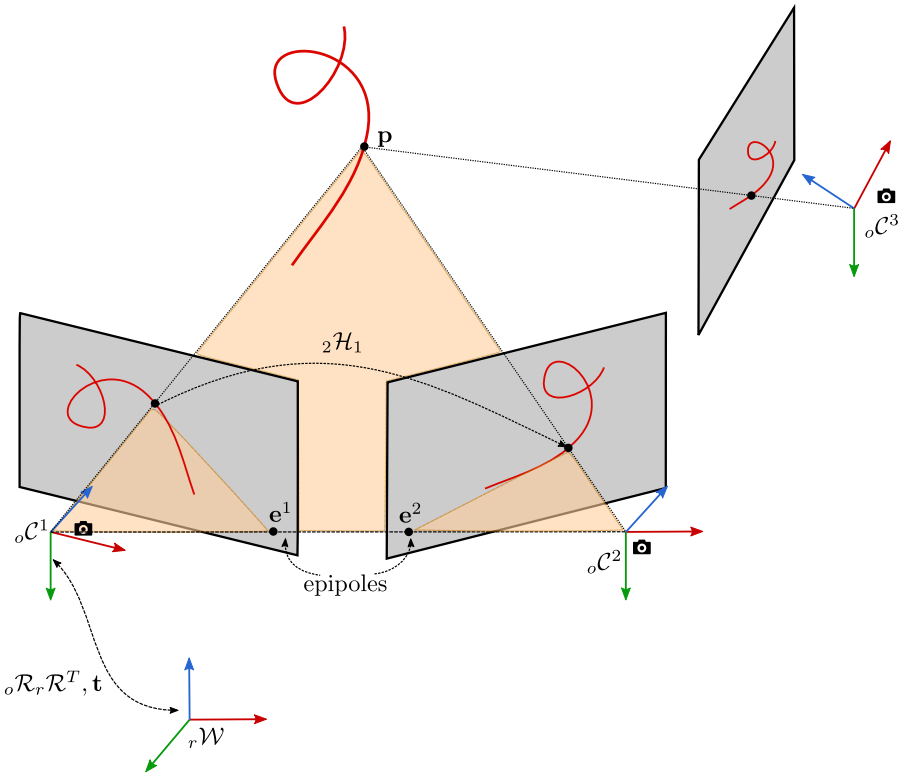


Figure 3.3: The perspective projection of a space curve at point $\mathbf{p}$. The camera frame are denoted by ${}_o\mathcal{C}^1, {}_o\mathcal{C}^2, {}_o\mathcal{C}^3$. The world frame is ${}_r\mathcal{W}$. The epipoles between view 1 and view 2 are given by $\mathbf{e}^1$ and $\mathbf{e}^2$, and the homography matrix between them is given by ${}_2\mathcal{H}_1$.

parameters $\mathcal{K} \in \mathbb{R}^{3\times3}$, then the projected pixel coordinates $\mathbf{z} \in \mathbb{R}^3$ is given by:

$$\mathbf{z} = \mathcal{P}\mathcal{K}\pi\left({}_o\mathcal{R}_r\mathcal{R}^T\left(\mathbf{p}-\mathbf{t}\right)\right), \quad \mathcal{P} = \begin{bmatrix}\mathbf{I} & 0\end{bmatrix} \in \mathbb{R}^{2\times3} \tag{3.12}$$

with $\pi(\mathbf{x})$ is the canonical projection function for a vector $\mathbf{x} \in \mathbb{R}^3$:

$$\pi(\mathbf{x}) = \frac{1}{\mathbf{e}_3^T\mathbf{x}}\mathbf{x} \tag{3.13}$$

and ${}_o\mathcal{R}_r$ is the rotation matrix from a regular coordinate frame (x= forward, y = left, z = up) to an optical frame ${}_o\mathcal{C}$ (x= right, y = down, z = forward):

$${}_o\mathcal{R}_r = \begin{bmatrix}0 & -1 & 0\\ 0 & 0 & -1\\ 1 & 0 & 0\end{bmatrix} \tag{3.14}$$

The camera intrinsic parameters $\mathcal{K}$ can be obtained by:

$$\mathcal{K} = \begin{bmatrix}fs_u & fs & c_u\\ 0 & fs_v & c_v\\ 1 & 0 & 0\end{bmatrix} \tag{3.15}$$

with focal length f [meters], pixel scaling factor s_u, s_v [[pixels/meter], principal point c_u, c_v [pixels], and a skew factor s [pixels/meter] that scales non-rectangular pixels.

3.2.2 *Reconstruction from Multiple Views*

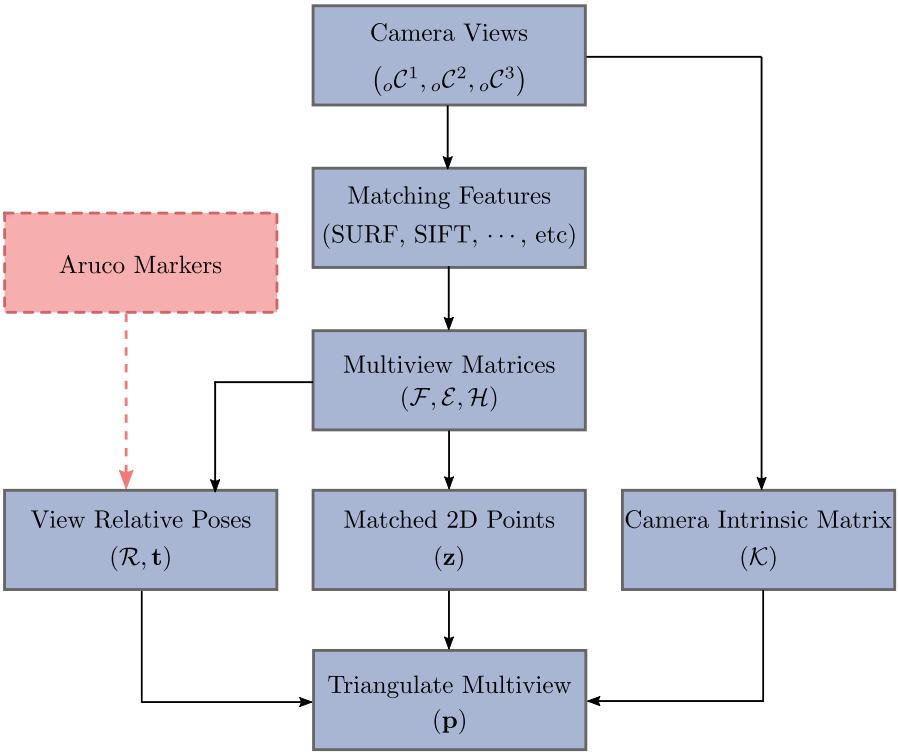


Figure 3.4: The flow chart of reconstruction from multiple views.

- **Matching Features** : the matching features require point correspondences between camera views. Different feature descriptors can be obtained, such as SURF, SIFT etc. Alternatively, the correspondence points across the views can be found with a tracking algorithm. In MATLAB, the functions such as `detectSURFFeatures`, `matchFeatures`, and `vision.PointTracker` can be applied.
- **Multiview Matrices** : the multiview-related matrices, including fundamental matrix $\mathcal{F}$, essential matrix $\mathcal{E}$, and homography matrix $\mathcal{H}$ can be found by MATLAB functions, i.e., `estimateFundamentalMatrix`, `estimateEssentialMatrix`, and `homography` [28], respectively.
- **View Relative Poses** : the orientation and the location of each camera in the coordinate system of the reference camera (such as view 2 in Fig. 3.3) can be found by inputting the multiview matrix to the `relativeCameraPose` function in MATLAB. Alternatively, the relative poses can be calibrated with ArUco markers, as shown in the dashed block in Fig. 3.4.

- **Matched 2D Points** : the matched 2D points are the target points for triangulate reconstruction. It links the pairwise matches of points across multiple views. Generally, it can be found using `imageviewset.findTracks` function in MATLAB. In our case, We introduce the matching approach by re-projecting each view (with segmentation) into a reference view and determining correspondences using the introduced Fréchet distance in Section 3.3.
- **Triangulate Multiview** : the locations of 3D target points $\mathbf{p}$ that correspond to points $\mathbf{z}$ matched across multiple views taken with calibrated cameras $\mathcal{K}$, can be reconstructed with `triangulateMultiview` in MATLAB.

It should be noticed that each above step can be obtained directly with exited libraries in MATLAB or OpenCV.

3.3 FRÉCHET DISTANCE

The Fréchet distance [131] was named after by Maurice Fréchet in 1906 as an effective metric for measuring curve similarity, which reflects the intuitive notion of resemblance. It can be illustrated as the relationship between a man and a dog (shown in Figure 3.5.**A**):

In the man-dog scenario, suppose that a man is walking his dog on a leash and is constrained to walk on one path while his dog is on another. Both are free to go forwards at their own pace, but they are not permitted to go backward. The Fréchet distance between the two curves is the shortest possible length of a leash.

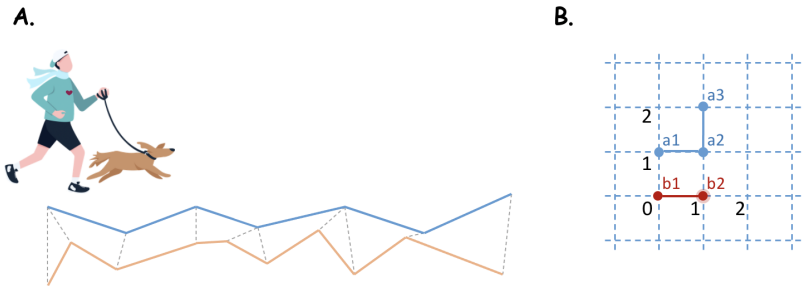


Figure 3.5: **A.** The illustration of man-dog Fréchet distance **B.** A simple example of discrete Fréchet distance

3.3.1 *Continuous Fréchet Distance*

The walking path can be regarded as a continuous curve that takes account into both the points' position and order along the curves.

Mathematically, this distance metric between two curves is a process defined from parameterized continuous curves to the standard definition for the Fréchet distance as:

Definition 3.3.1 (Continuous Parameterized Curve)**.** A curve $\mathcal{A} \in \mathbb{R}^d$ is a continuous parameterized curve if it can be represented by a continuous mapping $f : [a, b] \mapsto \mathbb{R}^d$, where $a, b \in \mathbb{R}$, $a \leq b$ and $[\mathbb{R}, d]$ is a metric space.

Definition 3.3.2 (Monotone Reparameterization)**.** A monotone reparameterization α is a continuous non-decreasing function $\alpha : [0, 1] \mapsto [0, 1]$ such that $\alpha(0) = 0$ and $\alpha(1) = 1$.

Definition 3.3.3 (Continuous Fréchet Distance)**.** Given two continuous curves $\mathcal{A}, \mathcal{B} \in \mathbb{R}^d$ in a metric space, the Frèchet distance is defined as:

$$\delta_F(\mathcal{A}, \mathcal{B}) = \inf_{\alpha,\beta} \max_{t\in[0,1]} \{\mathtt{dis}(\mathcal{A}(\alpha(t)), \mathcal{B}(\beta(t)))\} \tag{3.16}$$

where α, β are the monotone reparameterizations over the range $[0, 1]$, $\mathtt{dis}(\cdot, \cdot)$ represents the Euclidean distance, and inf is the infimum.

3.3.2 *Discrete Fréchet Distance*

In 1994, Eiter and Mannila approximated the Fréchet distance as the discrete Fréchet distance by polygonal curves with nodes. Then, the walking path can be regarded as a set of discrete points. Thus, the Fréchet distance is described in the followings:

Definition 3.3.4 (Discrete Fréchet Distance)**.** Given two polygonal curves $\mathcal{S}_p$ and $\mathcal{S}_q$ in a metric space, they are composed by the order-preserving sets of points. Let $\mathcal{S}_p = \{u_1, ..., u_p\}$ and $\mathcal{S}_q = \{v_1, ..., v_q\}$ be the corresponding sequences. A coupling between them can be identified as:

$$(u_{a_1}, v_{b_1}), (u_{a_2}, v_{b_2}), \ldots, (u_{a_m}, v_{b_m}) \tag{3.17}$$

where $a_1 = 1$, $b_1 = 1$ and $a_m = p$, $b_m = q$. The coupling has to respect the order of the points by $a_{i+1} = a_i + 1$ and $b_{i+1} = b_i + 1$. Then, taking into account the points' position and order along the curves, we define the discrete Fréchet distance denoted $\delta_F(\mathcal{S}_p, \mathcal{S}_q)$ by :

$$\delta_F(\mathcal{S}_p, \mathcal{S}_q) = \inf_{a_i,b_i} \max_{i=1,\ldots,m} \{\mathtt{dis}(u_{a_i}, v_{b_i})\} \tag{3.18}$$

where dis represents the Euclidean distance between one pair of points, and inf is the infimum over all parameterization of a_i and b_i.

This equation can be interpreted as: for every possible function u_{a_i} and v_{b_i}, it should find the largest distance between the man and his

dog as they walk along their respective path. Then, it needs to keep the smallest distance found among these maximum distances.

To understand it more intuitively, a simple example of the calculation of discrete Fréchet distance is visually illustrated. In Figure 3.5.**B**, there are two sets of polylines or polygonal curves with positions:

$$\mathcal{S}_p = \{a1, a2, a3\} = \{(0,1), (1,1), (1,2)\}$$
$$\mathcal{S}_q = \{b1, b2\} = \{(0,0), (1,0)\}$$

Taking into account that the start and end points of both curves must be matched with respect to the ordering of points, we have to respect the ordering direction without going back, the possible coupling matches could be

$$M_1 : (b1, a1), (b2, a2), (b2, a3)$$
$$M_2 : (b1, a1), (b1, a2), (b2, a3)$$

then, we find the minimum distances for each match.

$$\begin{aligned} min\,\{M_1\} &= min\,\{\texttt{dis}(b1, a1), \texttt{dis}(b2, a2), \texttt{dis}(b2, a3)\} \\ &= min\,\{1, 1, 2\} = 2 \\ min\,\{M_2\} &= min\,\{\texttt{dis}(b1, a1), \texttt{dis}(b1, a2), \texttt{dis}(b2, a3)\} \\ &= min\,\{1, 1.4, 2\} = 2 \end{aligned}$$

Thus, the discrete Fréchet distance in this example is equal to two.

In this thesis, we will use the discrete Fréchet distance to find the correspondent relationship of points by the similarity of curves among perspectives for multi-view reconstruction in Chapter 6.

Part III

CONTRIBUTIONS

4

NONLINEAR MORPHOLOGY ANALYSIS OF 2D CURLING SHAPE RECONSTRUCTION

This chapter is extracted from
"Image-based Approach to Reconstruct Curling in Continuum Structures"
J. Fan, E. Del Dottore, F. Visentin, B. Mazzolai
In 3rd IEEE International Conference on Soft Robotics (RoboSoft) 2020

4.1 INTRODUCTION

In this chapter, we have observed that *Passiflora* tendrils can produce various morphological changes in response to stimuli, i. e., called the curling shape or the tendril-like shape. According to the complexity of morphologies, we propose two approaches for 2D curling shape reconstruction and analysis. One is represented by a one-segment clothoid model, the other is represented by a piece-wise clothoid model. The proposed approaches have been validated on both a continuum biological and artificial structures. In detail, we design the morphology experiment in Section 4.2, review the definition of clothoid with Fresnel Integrals in Section 4.3.1, present the algorithm for sorting unarranged 2D points in Section 4.3.3. We then detail the single-segment and piece-wise curling model representations, respectively, in Section 4.3.4 and Section 4.3.5. Section 4.4 provides the results and error analysis. Finally, we conclude in Section 4.5 with discussions and future works.

4.2 BIOLOGICAL MORPHOLOGY EXPERIMENT

As mentioned in Chapter 1, the *Passiflora caerulea* is endowed with thigmoresponsive movements. It is an ideal plant to observe and analyze the curling behavior of tendrils. The plants we used were purchased from the local flower store and kept in the same growing chamber at $23°C$, with 70% relative humidity and a light cycle of $12/12h$. We chose those matured tendrils (the average length of about $15cm$) for conducting the experiment.

The preliminary aim of the experiment is to verify the existence of tendrils' curling behavior after the external stimuli (ignoring the

environmental factors). Meanwhile, it provides different generated morphologies by stimulation to verify our proposed methodology.

To do so, we first continuously stimulated the the tendril's ventral part (without the preference of the specific region) for 1 minute with a wooden stick. Then, we observed the changes in the shape and recorded the final shape after 4 minutes. We repeatedly executed the above experimental steps and selected those representative shapes of specimens providing the data support for the verification of model-based approaches.

From the multiple experiments, we found that the tendrils' curling ability after the stimuli vary, and the distal end of a *passiflora* tendril is much more sensitive than other ventral counterparts. This biological characteristic corresponds to Jaffe's study on *pea tendrils* [57]. According to the complexity of morphology, the shapes of selected data vary from less than one curl, to at most one curl, and to more than one curl. They are utilized in the following sections.

4.3 METHODOLOGY

4.3.1 *2D Clothoid Spiral*

As mentioned in Chapter 3, a clothoid, also named Cornu or Euler spiral, is a kind of curve with an affine property between curvature $\mathcal{K}$ and arc length s.

The affine property characterizing the clothoid is ideal for following the changes in the shape of natural structures. For this reason, we used this approach to represent and reconstruct curling structures, such as tendrils and tendril-like artificial structures.

4.3.2 *2D Reconstruction Framework*

The entire process is described by the flowchart in Figure 4.1.

The pre-processing stage comprises image resizing (800×1080 pixels) and binarization. Then, we segment the tendril part by applying Otsu's thresholding, and then fill the holes. In fact, segmentation and binarization could produce non-connected components that should instead be reconnected (binary closing operation). However, the operation might not ensure a complete connection of the components. The obtained binary image can now be processed to find its morphological thinning skeleton, which is likely composed by multiple components $\mathcal{P} = \{\mathcal{P}_1, \mathcal{P}_2, \cdots\}$. Due to possible discontinuities, identifying the most significant component, aggregating all the others, and better approximating a continuum curling structure are not trivial. To overcome the issue, we propose a 2D points-sorting algorithm (see Section 4.3.3).

Once obtained the sorted skeleton points, we can then proceed with either of the two options, according to specific application re-

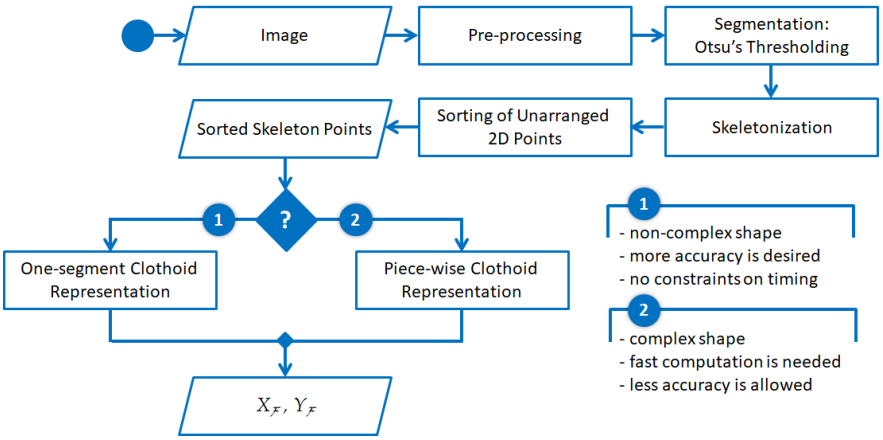


Figure 4.1: Flowchart of the methodology adopted for the shape representation and reconstruction in tendrils and continuum tendril-like artificial structures. $X_{\mathcal{F}}$ and $Y_{\mathcal{F}}$ are the results of the clothoid curve model fitting.

quirements: i) fitting the skeleton with a single segment or ii) using a piece-wise clothoid representation.

4.3.3 *Sorting Unarranged 2D Points*

Ordering unarranged points after skeletonization is a crucial part of the process since it defines the path to follow to identify the object in the scene and its whole actual shape.

After segmentation and skeletonization, we first choose a random point, p_0, as the starting one from the 2D skeleton points $\mathcal{P}$. We then select a prescribed direction ($\circledast : \mathcal{A}$ or $\mathcal{B}$) for sorting. Once finished, the whole process is also applied in the opposite direction. To ensure the direction consistency of all points, we flip the order of those points in $\mathcal{B}$ direction into $\mathcal{A}$. By merging the two sets, we obtain the ordered set of points $\mathcal{Q}_{\mathcal{I}}$ that will be used in the shape reconstruction (see algorithm 1).

The ordering procedure is detailed in algorithm 2. Given an arbitrary point p_c (during the first iteration, p_0 is initially selected), we collect its neighbours $\in \mathcal{P}$ into a new set $\mathcal{P}_o$ (from the function `CollectNeighboringPoints` in algorithm 3 explained below). Then, we calculate the scalar product between the vectors of the set $\{p_c - p_i : \forall p_i \in \mathcal{P}_o\}$ and the direction vector of the fitting line $\overline{\mathcal{L}}_o$ (of set $\mathcal{P}_o$), to divide them into two classes, $\mathcal{P}_+$ and $\mathcal{P}_-$. We need to go through both $\mathcal{P}_+$ and $\mathcal{P}_-$ to find the last ordered point p_l. If p_l is not found, the collecting-neighbours procedure is repeated in the loop after incrementing d_c by d_e. The next possible ordered point p_o is obtained by picking the one with the shortest Euclidean distance from p_c. p_o can be inserted into $\mathcal{Q}_{\mathcal{O}}$ and p_c updated by this new point (p_o). It is worth noting that p_l is found according to the direction expressed

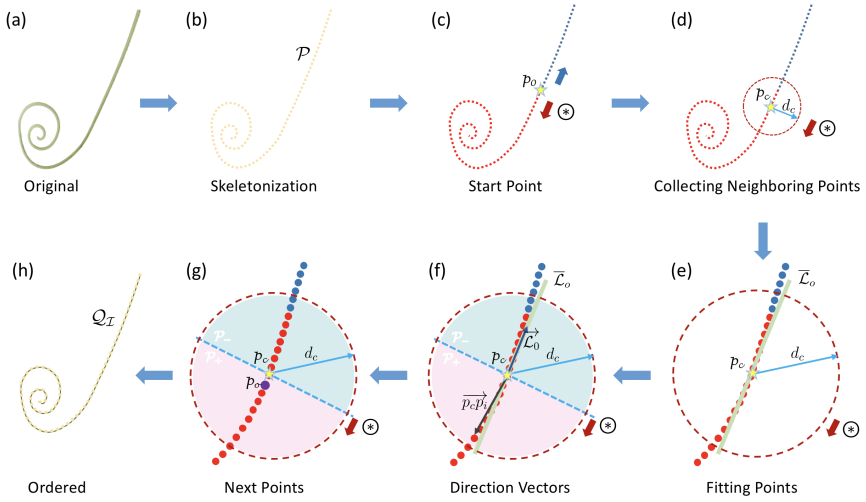


Figure 4.2: Procedure of ordering unarranged skeleton points. (a) a *passiflora* tendril with curling morphology, (b) unsorted skeleton points $\mathcal{P}$ after the pre-processing step, (c) a random point p_0 in the skeleton selected as the start point, marked by a yellow star, and a prescribed direction for points ordering, here taking the red arrow direction as an example for the following steps. (d) For a point to be sorted p_c, collecting its neighboring points within a circle with a radius d_c, (e) all the collected neighboring points fitted into a straight line $\mathcal{L}_o$ by MLSM. (f) After the points collection, the scalar product between the direction vector $\overrightarrow{\mathcal{L}_o}$ of the fitting line and each vector starting from p_c towards each neighbouring point p_i used to divide them into two classes $\mathcal{P}_-, \mathcal{P}_+$ (g) The next sorting candidate point P_o is obtained by picking the one with the nearest Euclidean distance from p_c, along the sorting direction (or in class $\mathcal{P}_+$). (h) The same process to sort points in the other direction. After ordering all the points in two directions, merge them to one unified direction according to the prescribed direction and get the ordered skeleton $\mathcal{Q}_I$

Algorithm 1: Ordering the unorganized skeleton points $\mathcal{P} \in \mathbb{R}^m$ into points $\mathcal{Q}_\mathcal{I} \in \mathbb{R}^n$, giving an initial starting point p_0.

Input : $\mathcal{P}$
Output: $\mathcal{Q}_\mathcal{I}$
// The size of $\mathcal{Q}_\mathcal{I}$ might be different from $\mathcal{P}$
Function `Main()`:
  $p_0 \leftarrow \mathcal{P}$
  // Select a starting point p_0 in $\mathcal{P}$
  $\mathcal{Q}_\mathcal{A} \leftarrow$ `OrderingPoints`$(\mathcal{A}, p_0, \mathcal{P})$
  // Indicate direction by $\mathcal{A}$
  $\mathcal{Q}_\mathcal{B} \leftarrow$ `OrderingPoints`$(\mathcal{B}, p_0, \mathcal{P})$
  // Indicate direction by $\mathcal{B}$
  $\mathcal{Q}_\mathcal{I} \leftarrow \mathcal{Q}_\mathcal{A} \cup p_0 \cup \mathcal{Q}_\mathcal{B}$
return $\mathcal{Q}_\mathcal{I}$

Algorithm 2: Ordering points of $\mathcal{P}$ with a given direction $\circledast$ at point p_0, given initial collecting distance d_0, increment collecting distance d_ϵ, current collecting distance d_c, maximum break distance d_B, maximum collecting distance d_M, maximum correlation index of local points ρ_0.

Input : $\circledast$, p_0, d_0, d_ϵ, d_B, $\mathcal{P}$, d_M, ρ_0
Output: $\mathcal{Q}_\mathcal{O}$

Function `OrderingPoints`($\circledast$, p_0, $\mathcal{P}$):
  $p_c = p_0$, $d_c = d_0$, $\mathcal{Q}_\mathcal{O} = \varnothing$, $p_l = \varnothing$ // Initialization
  while $d_c \leq d_B$ **do**
    $\mathcal{P}_+, \mathcal{P}_- = \varnothing$, $p_o = \varnothing$ // Reset as empty
    $\mathcal{P}_o, d_o, \overline{\mathcal{L}_o} \leftarrow$ `CollectNeighbouringPoints`(p_c, d_c, $\mathcal{P}$, d_M, ρ_0)
    for p_i *in* $\mathcal{P}_o$ **do**
      $\overrightarrow{v_c} \leftarrow \overline{\mathcal{L}_o}$ // Get direction vector of line $\overline{\mathcal{L}_o}$
      $\overrightarrow{v_i} = p_c\text{-}p_i$ // Get direction vector of line $\overline{p_c p_i}$
      if $\langle \overrightarrow{v_i}, \overrightarrow{v_c} \rangle \geq 0$ **then**
        // $\langle \cdot, \cdot \rangle$ denotes scalar product
        $\mathcal{P}_+ \leftarrow \mathcal{P}_+ \cup p_i$ // Insert p_i to $\mathcal{P}_+$
      else
        $\mathcal{P}_- \leftarrow \mathcal{P}_- \cup p_i$ // Insert p_i to $\mathcal{P}_-$
      end
    end
    if $p_c == p_0$ & $\circledast == \mathcal{A}$ & $\mathcal{P}_- \neq \varnothing$ **then**
      $p_l \leftarrow \texttt{argmin}_{p_l \in \mathcal{P}_-} \|p_l, p_0\|$
      // $\|\cdot, \cdot\|$ is Euclidean-distance
    else
      if $p_c == p_0$ & $\circledast == \mathcal{B}$ & $\mathcal{P}_+ \neq \varnothing$ **then**
        $p_l \leftarrow \texttt{argmin}_{p_l \in \mathcal{P}_+} \|p_l, p_0\|$
        // Ensure ordering direction at the first point
      end
    end
    if $p_l \neq \varnothing$ & $p_l \in \mathcal{P}_+$ & $\mathcal{P}_- \neq \varnothing$ **then**
      $p_o \leftarrow \texttt{argmin}_{p_o \in \mathcal{P}_-} \|p_o, p_0\|$
    else
      if $p_l \neq \varnothing$ & $p_l \in \mathcal{P}_-$ & $\mathcal{P}_+ \neq \varnothing$ **then**
        $p_o \leftarrow \texttt{argmin}_{p_o \in \mathcal{P}_+} \|p_o, p_0\|$
      end
    end
    $d_c = d_o + d_\epsilon$
    // Increase collecting distance (no satisfied p_o)
    if $p_o \neq \varnothing$&$p_o \notin \mathcal{Q}_\mathcal{O}$ **then**
      $\mathcal{Q}_\mathcal{O} \leftarrow \mathcal{Q}_\mathcal{O} \cup p_o$ // Insert p_o to $\mathcal{Q}_\mathcal{O}$
      $p_l = p_c$ // Update p_l
      $p_c = p_o$ // Update p_c
      $d_c = d_0$ // Reset collecting distance
    end
  end
  return $\mathcal{Q}_\mathcal{O}$
End Function

by $\circledast$. This iterative process is returned when the maximum break distance d_B is reached. It is natural to understand that there are no more candidate points at the end of the direction $\circledast$ for ordering even if d_c is increased.

The `CollectNeighboringPoints` process is modified from [70] as detailed in algorithm 3 . A point is considered to be neighbour if it lies within a circle distance with a radius d_o. The size of the radius d_o must be determined to reflect the range of the collected points. We hereby introduce the concept of *Correlation* based on the probability theory. From the data analysis point of view, we further introduce the idea of Diamond plots [4] to ensure the *correlation's* accuracy. The combination of them is applied to compute the appropriate radius d_o. All neighbouring points should also fit in a straight 2D-line ($\overline{\mathcal{L}}_o$) obtained by applying the Moving Least Squares Method (MLSM). As an ideal result, the fitting should achieve at least a tolerance of correlation ($\rho_c \geq \rho_0 \geq 0.9$). However, this case might never be satisfied due to the possible limited number of skeleton points. For this reason, we additionally defined a maximum collecting distance d_M ($\leq d_B$) to ensure a break out of the loop. Meanwhile, we select the maximum *correlation* index ρ_c within a distance d_M, for ensuring proper collecting range d_c, which is incremented in a loop by a fixed distance collecting distance d_ϵ in each `while` loop. The collected neighbouring points set $\mathcal{P}_o$, the corresponding collecting distance d_o, and the fitting line $\overline{\mathcal{L}}_o$ are returned when the control condition ($\rho_c < \rho_0$ or $d_o < d_M$) is satisfied.

4.3.4 *Single-Segment Clothoid Representation*

For simple configurations, i. e., less than or at most one curl, a single segment of the clothoid curve can be enough to follow the shape of a tendril-like object. Since, in this case, we are interested just in a single segment of the whole characteristic clothoid curve, the start l_a and the end l_b point needs to be defined.

This section aims to provide a solution to automatically find the proper parameters of the model defined in Section 4.3.1. It is worth mentioning that k_2 only affects the initial curvature when $s = 0$. For simplicity, without effect on curling shape representation, we assign $k_2 = 0$, $\alpha_0 = 0$, and $(x_0, y_0) = (0, 0)$ as the origin of the xoy coordinate system in Equation 3.6.

As a first step, we create a set of clothoid points (X, Y) according to the cardinality of $\mathcal{Q}_\mathcal{I}$. We explicitly defined the starting clothoid curve length as $s = l_a$ and the end as $s = l_b$ with respect to the xoy frame. Then, we can generate (X, Y) by interpolating the points between l_a and l_b, given a fixed constant distance Δ defined as the averaged points distance between the extremities. It is given by Equation 4.1 as follows:

Algorithm 3: Collecting neighboring points of point p_c, given maximum collecting distance d_M, increment collecting distance d_ϵ, current collecting distance d_c, threshold of collecting correlation ρ_0.

Input : p_c, d_c, d_ϵ, d_M, ρ_0, $\mathcal{P}$
Output: $\mathcal{P}_o$, d_o, $\overline{\mathcal{L}_o}$

Function `CollectNeighboringPoints`$(p_c, d_c, \mathcal{P})$:
- $\rho_c = 0$, $k = 0$, $\mathcal{R}_o = \varnothing$, $\mathcal{D}_o = \varnothing$, $\overline{\mathfrak{L}_o} = \varnothing$
- // Initialization
- **while** $\rho_c \leq \rho_0$ & $d_c \leq d_M$ **do**
  - $k = k + 1$
  - // Increase step counter
  - $P_o(k) \leftarrow \{p \in \mathcal{P} : \ \|\mathrm{p}, \mathrm{p_c}\| \leq d_c\}$
  - // Points set within distance d_c
  - $\overline{L_o}(k) \leftarrow \texttt{LSLineFit}(P_o(k))$
  - // Least-square line fitting
  - $\theta_o(k) \leftarrow \texttt{ANGLE}(\overline{L_o}(k))$
  - // Angle between $\overline{L_o}(k)$ and x axis
  - $\widehat{P}_o(k) \leftarrow \texttt{ROT}(P_o(k), \pi/4 - \theta_o)$
  - // Rotate $P_o(k)$ by $\pi/4 - \theta_o$
  - $\rho_c(k) \leftarrow \texttt{CORR}(\widehat{P}_o(k))$
  - // Correlation (X, Y) of points set $\widehat{P}_o(k)$
  - $D_c(k) = d_c$
  - $d_c = d_c + d_\epsilon$
  - // Increase collecting distance
- **end**
- $j \leftarrow \texttt{argmax}_{j \in [1,k]} \ \rho_c(j)$
- // Fitted line with maximum correlation
- $\mathcal{P}_o = P_o(j)$
- $d_o = D_c(j)$
- $\overline{\mathcal{L}_o} = \overline{L_o}(j)$
- **return** $\mathcal{P}_o$, d_o, $\overline{\mathcal{L}_o}$

End Function

$$
\begin{aligned}
X &= \{x(s, k_1, k_2, \alpha_0) \mid s = l_a + j \cdot \Delta, \ \ j \in \mathbb{Z}\} \\
Y &= \{y(s, k_1, k_2, \alpha_0) \mid s = l_a + j \cdot \Delta, \ \ j \in \mathbb{Z}\} \\
\Delta &= \frac{l_b - l_a}{N - 1}, \ \ j = 0, 1, 2, \cdots, N - 1
\end{aligned} \tag{4.1}
$$

where x and y are given by Equation 3.6, N is the number of ordered points from the image skeleton and Δ represents the constant interpolation distance. It's worth mentioning that the interpolation distance in the xoy frame is constant. However, the distance between any two adjacent ordered points in the image frame varies. Regardless, the distance is small enough relative to the whole length of the skeleton (with relative enough N). Meanwhile, the following affine

transformation will alter the interpolation distance as well. Thus, we could ignore the fitting error caused by point distance interval.

Next, to implement the parameter identification, we need to introduce the affine transformation for the clothoid curve. The transformation from the xoy frame to the image frame accounts for a scale matrix $\mathcal{S}(w_s, h_s, x_s, y_s)$, a rotation matrix $\mathcal{R}(\beta, x_r, y_r)$, and a translation matrix $\mathcal{T}(x_t, y_t)$. It results in:

$$\begin{bmatrix} X_{\mathcal{F}}^T \\ Y_{\mathcal{F}}^T \\ 1_{1\times N} \end{bmatrix} = \mathcal{R}(\beta, x_r, y_r)\mathcal{S}(w_s, h_s, x_s, y_s)\mathcal{T}(x_t, y_t) \begin{bmatrix} X_{\mathcal{I}}^T \\ Y_{\mathcal{I}}^T \\ 1_{1\times N} \end{bmatrix} \tag{4.2}$$

where $X_{\mathcal{F}}$ and $Y_{\mathcal{F}}$ are the resulting fitted points with respect to the ordered points ($X_{\mathcal{I}}$ and $Y_{\mathcal{I}}$) from the skeletonized image. The set of required parameters (Θ) are the followings: width scale (w_s), height scale (h_s), rotation angle (β), curvature parameters (k_1, k_2, and α_0), start length (l_a), and end length (l_b). They are chosen to define the fitting curve. In our case, we set $k_2 = 0$ and $\alpha_0 = 0$ without affecting the fitted shape. Note that x_i, y_i, with $i \in \{r, s, t\}$, are introduced since the transformation is performed with respect to a fixed point $(x_t(1), y_t(1))$, i. e., the starting point of the ordered skeleton in the image frame.

We can then formulate the single-segment clothoid fitting problem as an optimization problem that needs to minimize the Mean Square Error (MSE) of the fitted curve with the points of the skeleton:

$$\begin{aligned} \min_{\Theta} \quad & \frac{1}{2N}[(X_{\mathcal{F}} - X_{\mathcal{I}})^{\mathsf{T}}(X_{\mathcal{F}} - X_{\mathcal{I}}) + (Y_{\mathcal{F}} - Y_{\mathcal{I}})^{\mathsf{T}}(Y_{\mathcal{F}} - Y_{\mathcal{I}})] \\ \text{s.t.} \quad & \Theta = \{w_s, h_s, \beta, k_1, l_a, l_b\} \\ & \Theta_{\min} \leq \Theta \leq \Theta_{\max} \end{aligned} \tag{4.3}$$

To solve the problem, we compute its partial derivatives and use the gradient descent algorithm to find the globally optimal solution (see the Appendix A).

4.3.5 *Piece-wise Clothoid Representation*

In the presence of complex shapes – i. e., more than one curl or alternate curvatures – the single-segment clothoid representation might not be sufficient for capturing the shape. Moreover, solving the optimization problem in Equation 4.3 can be computationally expensive and thus unsuitable for real-time analysis or where fast computation is required. In such cases, a better approach would be to segment the element to be analyzed into multiple sections and then find the corresponding clothoid segment for each section. To ensure the sequential selection of segments, we consider both the position of the points and the curvature $\mathcal{K}$ of each segment.

Thus, the multi-segment fitting problem leads to a minimization of both coordinate and curvature errors. However, these two errors can

not be optimized simultaneously due to more conservative geometric constraints related to the shape of the curve. They have trade-off relationship under a determined number of segments. In addition, we need to guarantee a smooth curvature transition between any of the two adjacent segments. Therefore, we formulate the fitting problem as G^1 Hermite interpolation between two given points (namely, start and end point at each segment) with assigned tangent direction. The start/end points of the whole clothoid are manually selected. By applying [6] and by solving Ordinary Differential Equations (ODEs) in Equation 3.6 we can find a clothoid with minimal length (i. e., minimum $|l_b - l_a|$) that satisfy the requirements.

When connecting several clothoids into one curve, it is crucial to ensure continuity and smooth the curvature between connecting points. The value of l_a and l_b is here determined by dividing the ordered points of the skeleton into M segments and selecting the extremities as starting (l_a) and ending (l_b) points. To compute the curvature direction, we select an adjacent point (at a fixed arbitrary distance $d = 30$) from which we computed the tangent. It is shown as the following:

$$\alpha_s(i) = \texttt{arctan}\frac{Y_{\mathcal{I}}(j+d) - Y_{\mathcal{I}}(j)}{X_{\mathcal{I}}(j+d) - X_{\mathcal{I}}(j)}$$
$$\text{when } j = \lfloor \frac{N}{M} \rfloor \cdot (i-1) + 1,\ i \in \mathbb{Z},\ 1 \leq i \leq M$$
$$\alpha_e(i) = \begin{cases} \texttt{arctan}\dfrac{Y_{\mathcal{I}}(j+d) - Y_{\mathcal{I}}(j)}{X_{\mathcal{I}}(j+d) - X_{\mathcal{I}}(j)}, \\ \quad \text{when } j = \lfloor \frac{N}{M} \rfloor \cdot i + 1,\ i \in \mathbb{Z},\ 1 \leq i \leq M-1 \\ \texttt{arctan}\dfrac{Y_{\mathcal{I}}(j) - Y_{\mathcal{I}}(j-d)}{X_{\mathcal{I}}(j) - X_{\mathcal{I}}(j-d)}, \\ \quad \text{when } j = N,\ i = M \end{cases} \tag{4.4}$$

where $\alpha_s(i)$ and $\alpha_e(i)$ are the tangent directions of the start and end points with respect to segment number i.

4.4 RESULTS AND ANALYSIS

We evaluated the accuracy and the performance of the proposed methods by analyzing a set of images of *Passionflower*'s tendrils and an artificial continuum device that is able to perform two-dimensional bending. As an evaluation index for both approaches, we computed the R^2 value of the fit. The R^2 [60] is given in Equation 4.5 as a measure of goodness for the fitting. It depends on two sums of squares : Sum of Squares Total (SST), which indicates how far the data are from the mean, and Sum of Squares Error (SSE), saying how far the data (points in the skeleton) are from the model's predicted values.

$$R^2 = 1 - \frac{SSE}{SST} \tag{4.5}$$

$R^2 = 1$ represents the best optimal fit.

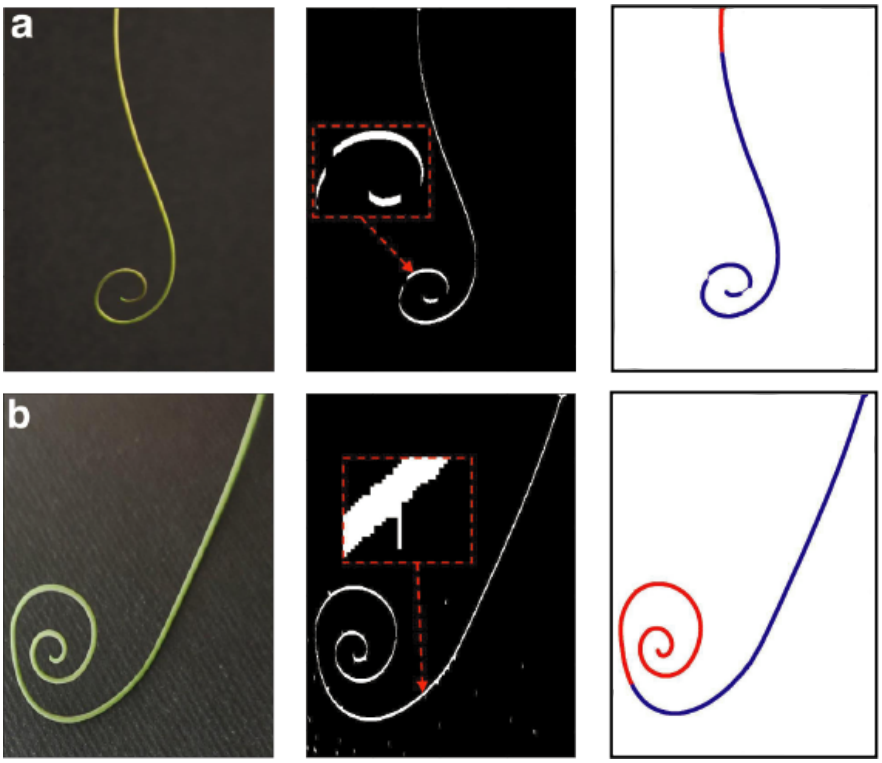


Figure 4.3: Two examples of the analyzed *Passionflower* tendrils (left pictures). a) Tendril with a single curl, and b) with multiple curls. In the middle, the results of the pre-processing phase, while on the right, visual results of the sorting algorithm. Red and blue represent opposite directions with the starting point located at the connection.

4.4.1 *Sorting Unarranged 2D Points*

The first set of evaluations has been done to test the performances of the proposed sorting algorithm. We considered the peculiar situation that might cause errors in the reconstruction. As shown in Figure 4.3 the skeleton points were correctly sorted even in the presence of discontinuities (Figure 4.3a), excessive noise or small branches (Figure 4.3b).

4.4.2 *Results of Single-segment Clothoid*

For the single-segment clothoid, we evaluated the partial derivatives of the cost function (Equation 4.3), and we extracted the six parameters used for optimal shape fitting. An example of the computed parameters are reported in Table 4.1, together with the goodness index and the computational time.

		T1			T2			T3		
Single-Segment	Opti-paras	(1634.4, 2182.3, 1.8, 3.3, 0.0, 0.7)			(1768.8, 1823.5, 4.0, 39.3, 0.3, -0.6)			(1394.5, 1240.6, 1.8, 10.8, -0.3, 1.5)		
			R^2	Time (s)		R^2	Time (s)		R^2	Time (s)
			0.998	131.692		0.968	91.817		0.989	144.173
Piece-wise		R^2_{PCC}	R^2_{PCD}	Time (s)	R^2_{PCC}	R^2_{PCD}	Time (s)	R^2_{PCC}	R^2_{PCD}	Time (s)
	1-Seg	0.896	0.986	0.128	0.353	0.697	0.120	-0.551	-0.148	0.136
	2-Seg	0.989	0.997	0.213	0.903	0.920	0.184	0.841	0.841	0.213
	3-Seg	0.997	0.999	0.273	0.963	0.966	0.246	0.920	0.950	0.282
	4-Seg	0.999	1.000	0.344	0.980	0.981	0.313	0.962	0.978	0.354
	5-Seg	1.000	1.000	0.402	0.986	0.985	0.364	0.983	0.985	0.414
	6-Seg	1.000	1.000	0.451	0.990	0.987	0.410	0.990	0.991	0.469

Table 4.1: Numerical results of the single-segment clothoid representation with optimal parameters search. The optimization problem was solved in MATLAB with gradient descent method, interior-point algorithm, a step tolerance of 10^{-4}, a central finite difference type, a finite difference step size of 10^{-6}, maximal iterations of 1000, and a random seed. Examples of optimal parameters (w_s, h_s, β, k_1, l_a, l_b) are reported in the first row (Opti-paras). The goodness R^2 of the approach is reported together with the computational time. The goodness of the piece-wise approach was tested with the clothoid representation (R^2_{PCD}) and compared with constant curvature model (R^2_{PCC}). Time refers to the computational time of computing the piece-wise clothoid fitting.

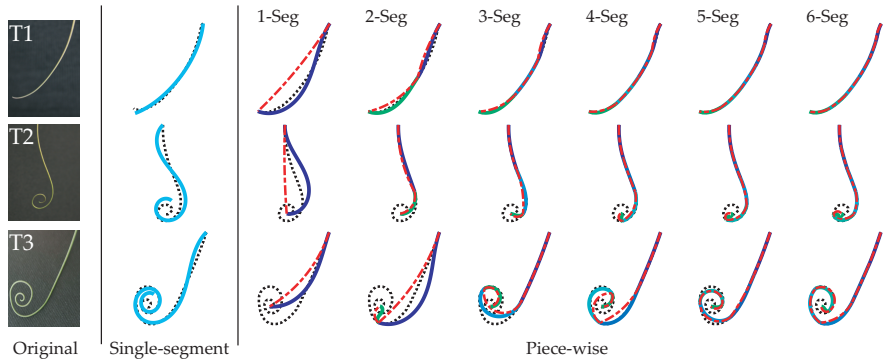


Figure 4.4: Three selected results of tendrils' shape analysis. On the row T1, a tendril with simple curvature, on row T2, tendril with a single curl, and on row T3, tendril with more than one curl. The first column shows the original 2D images. Results of the single-segment clothoid representation with optimal parameters are shown in the second column followed by the results of the piece-wise clothoid representation (up to 6 segments). Black dashed lines represent the skeleton extracted from the images. Red dashed lines represent the curves obtained with piece-wise constant curvature fitting. Colored solid lines (different colors match the segments) represent the curves obtained with piece-wise clothoid fitting.

As expected, the simpler the curve, the more accurate the result ($R^2 = 0.998$ with tendril T1 in Figure 4.4). However, the resolution of the optimization problem drastically affects the computational time, on average $\geq 122\ s$ over the three tendrils.

4.4.3 *Results of Piece-wise Clothoid*

We then evaluated our Piece-wise Clothoid (PCD) curve by comparing the fitting with the one computed using Piece-wise Constant Curvature (PCC) (Table 4.1 and Figure 4.4). The results show that all the curves obtained good fitness with a number of segments greater than five ($R^2 > 0.98$). Nevertheless, with the simpler shape tendril T1 (Figure 4.4) we could reach the best goodness ($R^2_{\text{PCD}} = 1$) evaluating the PCD with 4 segments, and a slightly worse performance obtained by the PCC, which reached $R^2_{\text{PCC}} = 1$ with 5 segments. Generally, the two approaches (PCC and PCD) are comparable in terms of goodness when increasing the number of segments but for low segmentation (≤ 4) the PCD method has better accuracy (case 1-Seg, $R^2_{\text{PCD}} = 0.986 > R^2_{\text{PCC}} = 0.896$).

As expected, by using the optimal curve parameters, we obtained a better accuracy with regards to 1-Seg piece-wise clothoid. In this case, the improvement increases with shape complexity (1% with T1, 28% with T2 and 115% with T3). However, the piece-wise method is faster (max $0.47s$ with 6-Seg in T3), suggesting that it can better fit the needs of real-time analysis.

4.4.4 *Model Validation on Soft Robotic Continuum Artefact*

Here we developed a soft robotic artefact to evaluate the model behaviour. The artefact is made of three rectangular actuators in series (total dimension $100mm(l) \times 20mm(b) \times 4mm(w)$), having each of two inflatable chambers made with two layers of silicons with different stiffness to obtain bending behavior upon actuation. The two adjacent chambers are coupled together in order to obtain antagonistic behavior.

In detail, the casting procedure has a three-step fabrication as follows. First, the bottom layer is manufactured with silicone (Ecoflex 0020, Smooth-ON), reinforced with a piece of textile fabric, acts as an in-extensible layer ($100mm(l) \times 20mm(b) \times 3mm(w)$). Second, a thin layer of silicone ($100mm(l) \times 20mm(b) \times 1mm(w)$) is used as an inflatable balloon when actuated. This layer is glued to the top of the bottom layer. An aluminum foil as a sacrificial material is embedded between these two layers to have uniform bonding at the border. Next, each actuator is equipped with pneumatic tubes for air supply/actuation. The actuator can bend in two opposite directions by pressurizing into each individual opposite chamber facing the bottom side of the textile-reinforced layer. Upon sequential actuation, the actuator allows demonstrating the antagonistic/bi-directional behaviour. Then, we connect the three actuators made by the same casting processing in series to have different bending shapes. Last, to avoid the overinflation of the whole artefact and to restrict its expansion of the ballooning silicone layer, a pouch is customized with expandable fabric to have uniformly elastic expansion while bending. Each of the actuators is actuated by electro-valves (Parker TX-1, 006) and controlled using a control unit to have a different sequence of bending/manipulation.

We evaluated our model by setting three different curves on the soft robotic artefact (first column in Figure 4.5). The sorting-points algorithm worked properly (third column in Figure 4.5) despite the irregular shape of the artefact, whose extracted skeleton presented many large branches and discontinuities (second column in Figure 4.5).

As for the natural tendrils, by selecting the optimal curve parameters, higher accuracy is obtained compared to the 1-Seg of the piecewise clothoid fitting (Table 4.2), with an improvement of 2% with C1, 4% with C2 and 5% with C3.

Also, the PCD performed generally better when less segmentation was applied (Figure 4.5), also reaching the best goodness earlier with regards to the PCC fitting (Table 4.2), with an execution time of $\sim 0.4\ s$.

4.5 SUMMARY

This chapter proposed a marker-less image-based approach to reconstruct the shape of continuum biological (e.g., tendrils of climbing

		C1			C2			C3		
Single-Segment	Opti-paras	(2209.7, 2435.5, 1.8, 0.3, 9.7, 10.2)			(1628.6, 1959.5, 0.7, 26.8, -0.4, 0.3)			(1683.3, 2159.1, 3.3, 3.8, 1.0, 0.5)		
			R^2	Time (s)		R^2	Time (s)		R^2	Time (s)
			0.998	114.437		0.997	132.018		0.980	132.401
Piece-wise		R^2_{PCC}	R^2_{PCD}	Time (s)	R^2_{PCC}	R^2_{PCD}	Time (s)	R^2_{PCC}	R^2_{PCD}	Time (s)
	1-Seg	0.944	0.978	0.106	0.745	0.958	0.106	0.942	0.929	0.102
	2-Seg	0.994	0.988	0.170	0.968	0.994	0.169	0.962	0.992	0.164
	3-Seg	0.999	0.998	0.226	0.999	0.999	0.227	0.992	0.997	0.222
	4-Seg	0.999	0.999	0.292	0.998	0.999	0.310	0.998	0.999	0.287
	5-Seg	0.999	1.000	0.336	0.999	1.000	0.363	0.998	1.000	0.332
	6-Seg	1.000	1.000	0.375	1.000	1.000	0.405	0.999	1.000	0.373

Table 4.2: Numerical results and goodness of the analysis for the soft continuum robot. The optimization problem for the single-segment clothoid fitting was solved as for the biological case. Examples of optimal parameters (w_s, h_s, β, k_1, l_a, l_b) are reported in the first row (Opti-paras). The goodness R^2 of the approach is reported together with the computational time (in seconds). The goodness of the piece-wise approach was tested with the clothoid representation (R^2_{PCD}) and compared with constant curvature model (R^2_{PCC}). Time refers to the computational time of computing the piece-wise clothoid fitting.

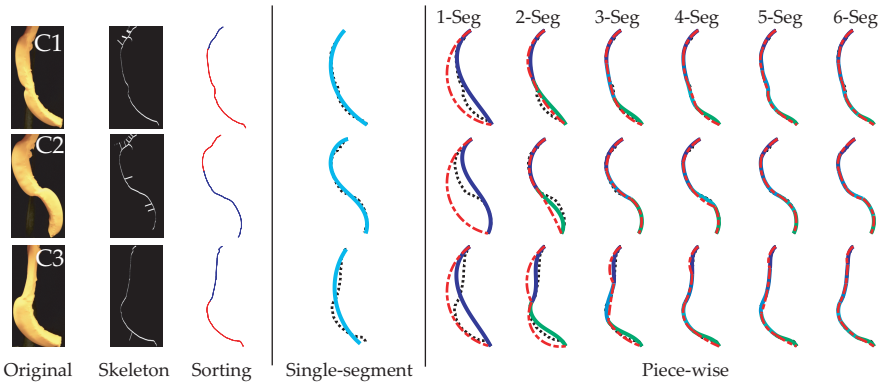


Figure 4.5: Results of shape analysis for three configurations of the soft continuum robot. C1 have the three chambers inflated in the same direction, C2 has opposite inflation over the chambers, and C3 has only the last chamber inflated in one direction. The first column shows the robot configuration. The second column shows the picture after skeletonization. The third column shows the results of the sorting algorithm. The fourth column has results of single-segment clothoid fitting with optimal parameters search; while the other columns show the results of piece-wise approach with the constant curvature fitting (red dashed lines) and the clothoid curve fitting (colored solid lines, different colors represent different segments). Black dashed lines represent the skeleton.

plants) and artificial (continuum soft robots) structures that can deform into coils or curls with variable curvature that depends on the arc length. The proposed method is based on 2D clothoid curves, for which we explore two resolution approaches: i) single-segment clothoid representation, with optimal curve parameters search; ii) piece-wise clothoid representation, with G^1 Hermite-fitting solution.

Besides, we proposed a novel algorithm to sort 2D unarranged points that addresses the issue of possible undesired branches and discontinuities.

We numerically evaluated the performance of the solutions and compared them with a constant curvature fitting. We obtained an improvement of more than 100% in tendril and up to 5% with a soft continuum robotic artefact, demonstrating the feasibility and the reliability of my approach. The proposed model would be applied for shape representation and reconstruction on both long slender living organisms and continuum soft robots with curling-like behavior.

However, the proposed shape description method by piece-wise clothoid curve is used with a fixed number of segments to represent the curling shape, maybe not with the optimal number, which will be solved in the next chapter.

5

NONLINEAR MORPHOLOGY ANALYSIS OF 2D CURLING SHAPE PIECEWISE RECONSTRUCTION

This chapter is extracted from
"An Image-Based Method for the Morphological Analysis of Tendrils with 2D Piece-Wise Clothoid Approximation Model"
J. Fan, F. Visentin, E. Del Dottore, B. Mazzolai
In Biomimetic and Biohybrid Systems 2020

5.1 INTRODUCTION

In this chapter, we extend the previous work in Chapter 4 and present an image-based method, which approximates curling structures with the clothoid model in Fresnel Integral with rational approximated form. This approach can achieve the full automatic selection of the optimal number of segments and properly represent different configurations (both in temporary state and shape evolution) of natural tendrils. This work will be organized as follows: Section 5.3 presents each step of the proposed image-based morphology reconstruction method. Section 5.4 provides the analysis and results. Then, we conclude in Section 5.5 with discussions and future work.

5.2 BIOLOGICAL MORPHOLOGY EXPERIMENT

The experiment in this chapter is the further observation of morphological changes in Section 4.2. In this section, we paid attention not only to the temporary state, like the final shape, but also to the whole evolution of tendrils' morphology. In the previous experiment, we observed the existence of the curling behavior of Passiflora caerulea after mechanical stimulation. In the meantime, the curling ability varies from the ventral stimuli exerted by a wooden stick. The stimulated region in the process of stroking was not assigned. While in this experiment, the tendrils have been ventrally stimulated along all their length, i. e., the region of stimulation ranging from the base to the tip of the tendrils.

In detail, the plants were purchased and kept in the same environmental preference as the previous one (in the growing chamber at

$23°C$, with 70% relative humidity and a light cycle of $12/12h$). Since matured tendrils have the maximum irritability in their thigmotropic movement, it is easier to observe the whole evolution of morphological changes within a short period of time. The length of tendrils we chose is about $15 - 20cm$ (achieved the mature stage) for conducting the experiment. All the specimens were go-and-back stroked by one same wooden stick for one minute in the ventral part from the base to the tip of the tendrils. Subsequently, the stimulated tendril was firmly attached to a substrate to provide a stable reference point, and its morphological evolution was recorded for four minutes. Finally, the collected data is used for shape configuration reconstruction in the following steps.

5.3 METHODOLOGY

The image-based method for the morphological analysis of tendrils and tendril-like structures is composed of five key macro steps, as shown in Figure 5.1.

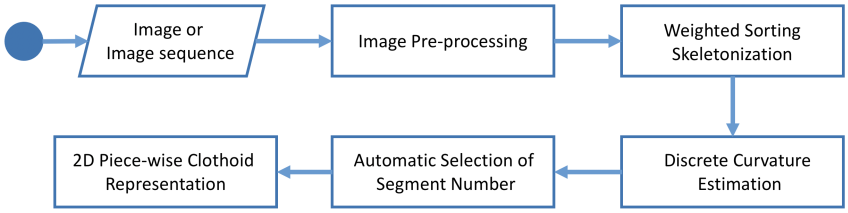


Figure 5.1: The complete flowchart of the proposed method. To perform the morphological analysis, we start by pre-processing the acquired images and by performing the skeletonization to extract the points within the region of interest. Then, we sort the unordered skeleton points. Next, we estimate the curvature/arclength relationship for each point which is used to compute the minimum number of segments required to represent the tendril. Finally, we fit a 2D clothoid for each segment to obtain the entire tendril structure.

The first step consists of a pre-processing stage that includes the image resizing (300×380 pixels), distortion correction and binarization. Then, we apply a classic segmentation method (Otsu's thresholding) to identify the tendril part, and we fill the holes to find the largest Region of Interest (ROI). We can now extract the skeleton while preserving the topology structure in the ROI.

The points extracted from the skeleton cannot be directly used for the curvature fitting due to the possible presence of branches, holes, unordered regions and sharp corners, which prevent understanding of the correct sorting direction. I have proposed a sorting skeletonization algorithm to address most of the mentioned issues [30]. Here we address the specific issue introduced by the presence of sharp corners. An example of this condition is shown in Figure 5.2a and Figure 5.2b.

In the following sections, we describe in detail each of the successive steps. Starting from the weighted sorting algorithm, then I explain how to realize the discrete curvature estimation, the automatic selection of segments, and the shape fitting using the clothoid spirals.

5.3.1 *Weighted Sorting Skeletonization*

To define the shape direction from the unordered skeleton points obtained from the pre-processing phase, in [30], I proposed the `CollectNeighboringPoints` algorithm based on the Moving Least Squares Method (MLSM). The algorithm starts from a randomly chosen starting point (p_s, yellow circled point in Figure 5.2c) in the skeleton, and it first orders the points in one direction (red arrow), then in the other one (blue arrow). For each point of the skeleton (as in the case of p_t shown in Figure 5.2c), it fits a line $L : y = ax + b$ (solid blue line in Figure 5.2d) over the N neighboring points $p_i = (x_i, y_i), i \in [1, N]$ collected within a local circular area of radius R.

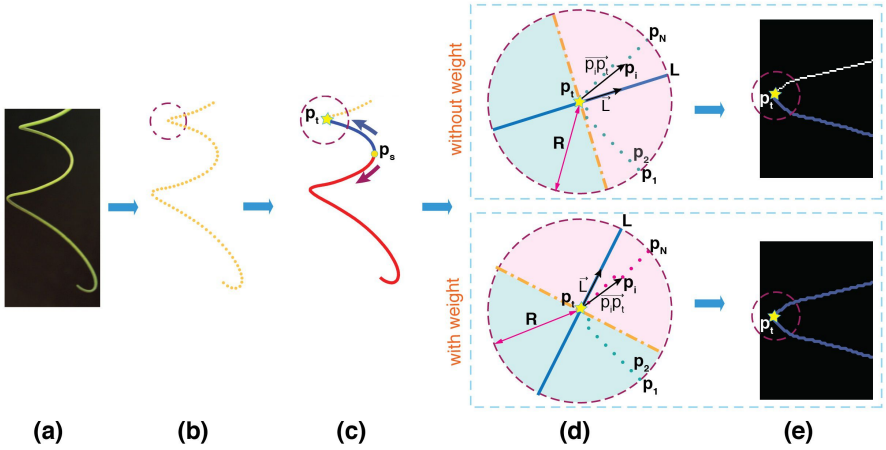


Figure 5.2: Previous [30] and current skeleton sorting algorithm procedures. (a) A *passionflower* tendril with complex morphology. (b) The unordered skeleton points extracted from the pre-processing step. The dashed circle highlights the case of sharp curvature. (c) An evolution of the sorting algorithm starting from point p_s. The following sequence shows how the case is approached by the previous (without weights, top row) and the current (with weights, bottom row) algorithm. (d) The neighbours of p_t are collected within a local circular area of radius R. The blue solid line denotes the fitting line, and the yellow dash-dotted line defines two classes. (e) The sorting results. In the case without weights, the points remain unordered (white line), while when weights are used, all the points of the skeleton are collected and ordered (blue line).

The sorting direction is determined based on a two-object classifier, where each class represents one of the two possible directions. The classification is achieved by performing the cross-product of the

vectors of the neighboring points over the direction vector of the fitting line L. This operation is iterated until reaching both ends of the skeleton with all the sorted and collected points.

Figure 5.2d shows the classification of the points into two regions (cyan and magenta areas in the figure) separated by a yellow dash-dotted line. The results (Figure 5.2e) show that without using weights, a portion of the points in the skeleton remains uncollected (white line above the critical point p_t, Figure 5.2e top view). This is because the fitting line L cannot classify the points into two correct categories, and the classifier identifies all the candidate points p_i as belonging to the same class of the current point p_t. As a consequence, we cannot determine the next point to be sorted. p_t is treated as an end-point of the skeleton, and then the sorting loop ends.

To solve this problem, we introduced tuning weights w_i, for each neighbouring point p_i, within the radius R, assigned according to the ratio of the Euclidean distance $r = ||p_i - p_t||^2$, as follows:

$$w_i = e^{-r^2/R^2} \tag{5.1}$$

In this way, we can strengthen the importance of the closest points around the target sorting point p_t. The fitting then provides a nonlinear diminishing fitting weight for each p_i by minimizing the function:

$$\mathcal{E}_{p_t}(p_1, p_2, \cdots, p_N) = \min_{a,b} \sum_{i=1}^{N} (ax_i + b - y_i)^2 w_i \tag{5.2}$$

The classifier in the weighted sorting algorithm is now able to separate the points into two classes, and all the skeleton points are included and sorted (blue line, Figure 5.2e bottom view). The sorted points set is denoted as P_{srt} in the following.

5.3.2 *Discrete Curvature Estimation*

We now calculate the discrete curvature for the sorted skeleton. Discrete curvature for the planar curve can be estimated by computing circumcircle for every triplet (p_{i-1}, p_i, p_{i+1}) at point p_i (Figure 5.3b). We assigned a sliding window distance ($d = 50$) to choose neighbouring points p_{i-d} and p_{i+d} along the skeleton. Then, we obtained the circumcenter, the correspondent radius R_i, from each triplet, and the corresponding curvature k_i, defined as:

$$k_i = \frac{1}{R_i} \qquad where\ R_i = R_{circle}(p_{i-d}, p_i, p_{i+d}) \tag{5.3}$$

Then, each point with its own curvature is mapped from pixel-value space to arclength-curvature ($s - k$) space. In this chapter, we compute the arclength for each point s_i, by integration of the Euclidean distance over every two adjacent points:

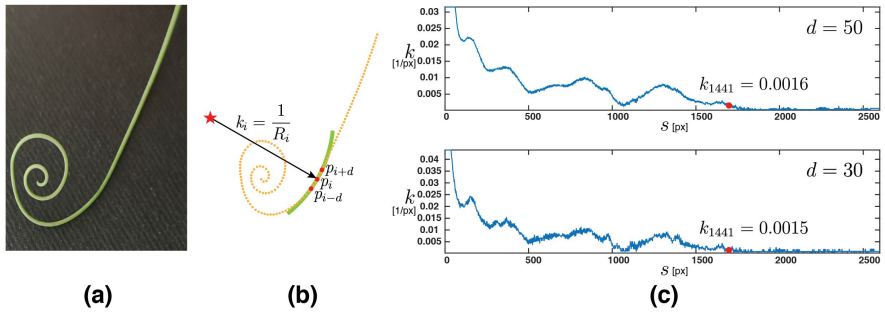


Figure 5.3: (a) Displays a natural *passionflower* tendril. (b) Shows the sorted skeleton in yellow points, and the green colored arc shows the fitting circumcircle at point p_i for the triplet (p_{i-d}, p_i, p_{i+d}) with the given curvature $k_i = 1/R_i$. (c) Demonstrates the planar curvature estimation from discrete skeleton points using $d = 50$ (top) and $d = 30$ (bottom). An example of the curvature at point p_{1441} is given as a red dot.

$$s_i = \sum_{j=1}^{i} ||p_j - p_{j+1}||_2 \tag{5.4}$$

The sliding window distance should be defined on the base of the image resolution. This ensures that the curvature is a constant among the triplet points. Also, the choice of the sliding window distance affects the whole curvature smoothness. For example, the case of $d = 30$ presents more noises with respect to a window of $d = 50$ (Figure 5.3c).

5.3.3 *Automatic Selection of Segment Number*

This subsection aims to define an optimal number of piece-wise clothoid curves to describe natural tendril and tendril-like structures and thus analyse their morphologies. An essential step is to define a method that automatically splits the curve into the minimal sequence of pieces of linearly varying curvature. To solve the problem, we use dynamic programming[1] with an up-sweep approach. This allows to transfer the optimization of the whole shape into a series of optimal sub-problems. The problem is formalized as finding the minimum path (minimum number of segments) from a certain point p_i, up to an ending point p_j (with $i < j$), both selected from the set of the sorted list of skeleton points $P_{srt} = \{p_1, p_2, \cdots, p_M\}$, having the minimum fitting error defined as:

$$\mathcal{J}(p_i, p_j) = \min_{i<k<j} \left\{ \mathcal{J}(p_i, p_k) + \mathcal{J}(p_k, p_j),\ \mathcal{E}_{seg} + \mathcal{E}_{fit}(p_i, p_j) \right\} \tag{5.5}$$

where $\mathcal{J}(p_i, p_j)$ denotes the $M \times M$ cost matrix of fitting errors over the connected piece-wise segments. On the right hand of the

1 Bellman k-segmentation algorithm: https://justinwillmert.com/articles/2014/bellman-k-segmentation-algorithm/

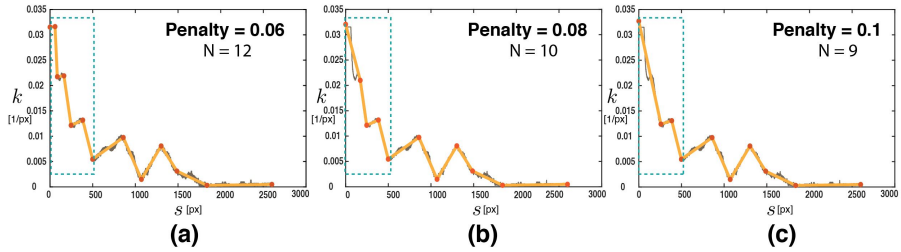


Figure 5.4: Results for the automatic selection of segment number with different penalties. The larger the value we choose, the less segments we have (yellow lines), and more error is introduced. The green dashed boxes show the segmentation differences.

cost equation $\mathcal{J}(p_i, p_k)$ denotes the specific configuration from p_i to a point p_k which lies in between the start and the end point. Similarly, $\mathcal{J}(p_k, p_j)$ denotes the configuration from p_k to the endpoint p_j.

The constant ϵ assigns a penalty factor to the path from p_i to p_j treated as a single segment. Figure 5.4 shows the fitting obtained with three penalties. The lower the value of $\mathcal{E}_{seg}$, the higher the number of segments, thus the higher the accuracy. It represents a compromise between the fitting accuracy and the total number of segments. In this chapter, we assigned $\mathcal{E}_{seg} = 0.03$.

The second error factor, $\mathcal{E}_{fit}(p_i, p_j)$, describes the minimal sum of the fitting errors caused by using linear regression on the segment from point p_i to p_j. It is defined by:

$$\mathcal{E}_{fit}(p_i, p_j) = \min_{a_{ij}, b_{ij}} \left(\sum_{t=i}^{j} \left| a_{ij} \cdot s_t + b_{ij} - \kappa_t \right|^2 \right) \tag{5.6}$$

where a_{ij} and b_{ij} are the slope and intercept of the least-square fitting line for all the points p_t between p_i and p_j. Both the a_{ij} and b_{ij} should be stored in an $M \times M$ dimensional matrix, in order to recover the final optimal piece-wise line segments for sorted skeleton points set $P_{srt} = \{p_1, p_2, \cdots, p_M\}$. The parameters s_t and κ_t are calculated by Equation 5.4 and Equation 5.3, respectively.

We apply the dynamic programming method to update the matrix $\mathcal{J}$ by traversing all pairs of (p_i, p_j) (shown in Figure 5.5). It demonstrates the characteristic up-sweep updating scheme. $\mathcal{J}$ is a strictly upper triangular matrix. Each value inside the matrix represents the obtained minimal cost for points pairing (p_i, p_j). First, the diagonal elements in $\mathcal{J}$ are initialized to zeros. Then, the up-sweep update method is applied to update the minimal cost recurrently. We need to repeat for all points pair of $(p_i, p_j), i, j \in [1, M]$ by moving up a row in the $\mathcal{J}$ matrix towards the upper right corner. It is worth mentioning that the updates only take the smaller cost values either divided into two segments by k, i.e., $(p_i, p_k) - (p_k, p_j)$, or treat (p_i, p_j) as a single segment, after traversing all $k \in (i, j)$ as given by Equation 5.5. A segment-path matrix $\mathcal{S}(p_i, p_j)$ initialized with -1 with the dimension

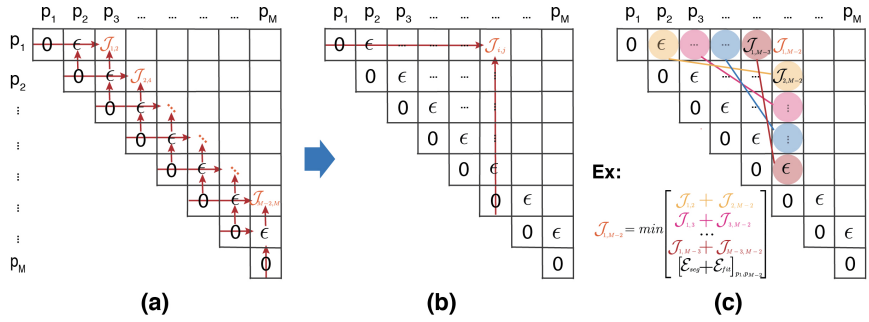


Figure 5.5: The dynamic programming procedure. (a, b) indicates the updating is characterized by up-sweep scheme. (c) gives an example of updating of $\mathcal{J}_{1,M-2}$ (simplified for $\mathcal{J}(p_1, p_{M-2})$). It selects the minimal cost value while traversing all $i < k < j$ (divide into two segments), compared with treating as a single segment.

of $M \times M$ is generated for the reconstruction of the optimal regression path (i.e., at which points the segments are created). It is defined as:

$$\mathcal{S}(p_i, p_j) = \begin{cases} -1, & \text{if } \mathcal{J}(p_i, p_k) + \mathcal{J}(p_k, p_j) < \mathcal{E}_{seg}(p_i, p_j) + \mathcal{E}_{fit}(p_i, p_j) \\ k, & \text{others} \end{cases} \tag{5.7}$$

Finally, the algorithm will reconstruct the optimal regression of segments by going through the segment-path matrix recurrently. It starts from the top right corner of $\mathcal{S}$, i.e., $\mathcal{S}(p_1, p_M)$, until reaching -1 for all listed pair of $\{(p_1, p_{s_1}), (p_{s_1}, p_{s_2}), \cdots, (p_{s_{n-2}}, p_{s_{n-1}}), (p_{s_{n-1}}, p_M)\}$ in $\mathcal{S}$. Notice that the segment path is reconstructed in a recurrent loop, while it may not go over all pairs of (p_i, p_j) that existed between (p_1, p_M). The optimized piece-wise segmentation points with a total of n segments are given as:

$$P_{seg} = \{p_1, p_{s_1}, p_{s_2}, \cdots, p_{s_{n-1}}, p_M\} \tag{5.8}$$

Then, from the optimized cost, we select n elements, p_{s_i} with $i = 1, \ldots, n$, that identify the junction points of the piece-wise segments.

5.3.4 *2D Piece-wise Clothoid Representation*

Once the number of segments is selected, the algorithm begins the fitting with the 2D piece-wise clothoid spirals. The Cartesian coordinates of a 2D clothoid spiral can be parameterized by Fresnel integrals form defined as $\pi B \begin{pmatrix} \mathcal{C}(l) \\ \mathcal{S}(l) \end{pmatrix}$. For the computational efficiency, here we choose a rational approximation with 1.7×10^{-3} error [48], obtained by evaluating the error of polynomial approximation of the equations:

$$\begin{aligned} \mathcal{C}(l) &= \int_0^l \cos\frac{\pi}{2}\tau^2\, d\tau \approx \frac{1}{2} - R(l)\sin\left(\frac{1}{2}\pi\left(A(l) - l^2\right)\right) \\ \mathcal{S}(l) &= \int_0^l \sin\frac{\pi}{2}\tau^2\, d\tau \approx \frac{1}{2} + R(l)\cos\left(\frac{1}{2}\pi\left(A(l) - l^2\right)\right) \end{aligned} \tag{5.9}$$

having:

$$\begin{aligned} R(l) &= \frac{0.506l + 1}{1.79l^2 + 2.054l + \sqrt{2}} \\ A(l) &= \frac{1}{0.803l^3 + 1.886l^2 + 2.524l + 2} \end{aligned} \tag{5.10}$$

where l denotes the arclength along the clothoid from its initial position.

From normalization based on integration by substitution, we have each clothoid point as:

$$\begin{aligned} x &= \pi B \cdot \mathcal{C}(l') = \frac{\pi B}{\alpha}\int_0^{l'} \cos\tau^2\, d\tau \\ y &= \pi B \cdot \mathcal{S}(l') = \frac{\pi B}{\alpha}\int_0^{l'} \sin\tau^2\, d\tau \end{aligned} \tag{5.11}$$

where $l' = \alpha l$ with $\alpha = \sqrt{\frac{\pi}{2}}$ is the normalized arclength, and $\frac{\pi B}{\alpha}$ is the scaling factor of the clothoid segment, which is a non-negative parameter that defines the degree of linear curvature variation. We can then deduce:

$$\begin{aligned} \kappa &= \frac{2\alpha^2 l}{\pi B} = \frac{l}{B} \\ s &= \frac{\pi B}{\alpha} l' = \pi B l \end{aligned} \tag{5.12}$$

For each defined segment (from p_{s_i} to p_{s_j}, with $i < j$), we can calculate the segment arclength by:

$$s(p_{s_j}) - s(p_{s_i}) = \pi B \left| l(p_{s_j}) - l(p_{s_i}) \right| = \pi B^2 \left| \kappa(p_{s_j}) - \kappa(p_{s_i}) \right|, \tag{5.13}$$

and extract the scaling factor:

$$B = \sqrt{\frac{s(p_{s_j}) - s(p_{s_i})}{\pi \left| \kappa(p_{s_j}) - \kappa(p_{s_i}) \right|}} > 0. \tag{5.14}$$

The clothoid approximation of the shape is then obtained by interpolating with the points of each obtained segment by Equation 5.11, with successive rotation and translation to extract the final clothoid points approximating the curling shape.

5.4 RESULTS AND ANALYSIS

We evaluate the accuracy and performance of the proposed method by analyzing a set of configurations of a natural tendril captured in 2D RGB images (digital camera Canon EOS 550D with Lens Canon EF-S 18-55mm f/3.5-5.6 IS II) extracted from the Supplementary Video[2] which records the changes in the morphology of a *passionflower* tendril, taken place in about 4 minutes after being stimulated with a wooden stick for about 1 minute.

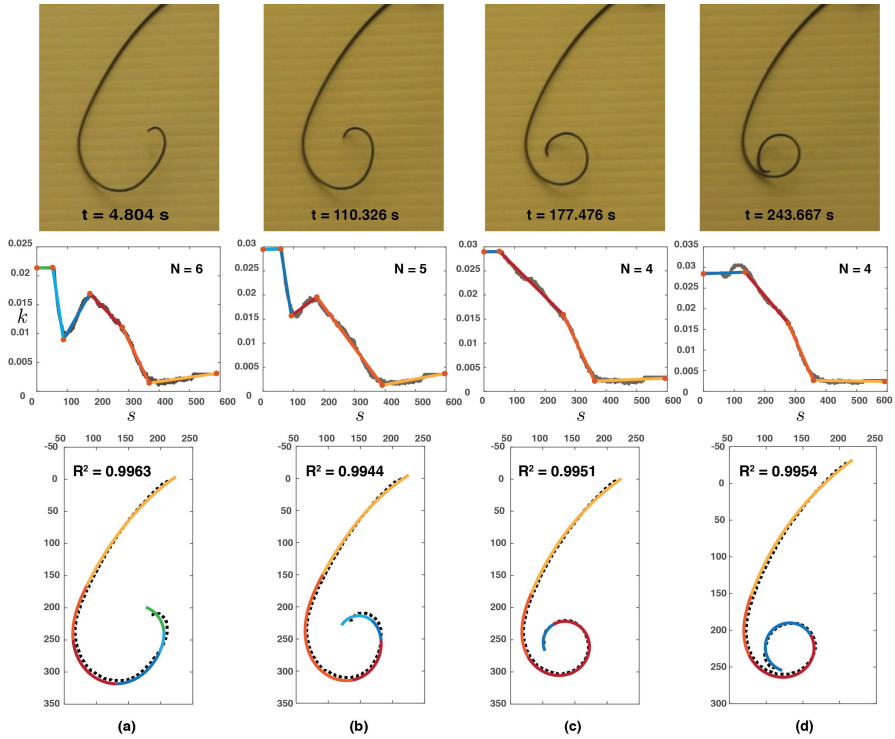


Figure 5.6: Results of our methodology for natural tendril morphology analysis. In the first row, four images extracted from a video[2] of *passionflower* tendril changing its morphology in time after being rubbed. The second row provides the relationship between the arclength S and the curvature k. The third row shows the morphological representation with the corresponding piece-wise clothoid spiral. The black dashed lines denote the extracted skeleton, coloured solid lines denote each piece of the clothoid curve. Corresponding segments have same colors in second and third row.

From the whole frame sequence, I choose four representative images and analyzed the morphologies. Figure 5.6 shows the arclength-curvature relation established for each point of the skeleton (second row) and the minimum segments (third row) obtained by our program.

We adopt R^2 to quantify the curve fitting error, with $R^2 = 1$ expressing the best fitting. Our approach demonstrated to be highly

2 Video link : https://youtu.be/DmbInPlpT1U

accurate for the analysis of curling shape morphologies, all the results show $R^2 > 0.994$, even with the minimum retrieved number of $N = 4$ segments.

Our approach can then be purposely adopted to analyze the changes over time in the morphology of continuum adaptive structures, like living growing tendrils. Figure 5.7 shows an example of such analysis for the morphological evolution of our *passionflower* tendril after the induced stimulation. It can be noted that a portion of the tendril does not change curvature in time, even though previously stimulated (see Supplementary Video[2]), while the most apical region is more dynamic in curvature variation. This result might suggest a well-localized zone for coil actuation, independent from the region of stimulation. However, a deeper and more focused analysis is worth establishing the relation between the provided stimulus and connected behaviour.

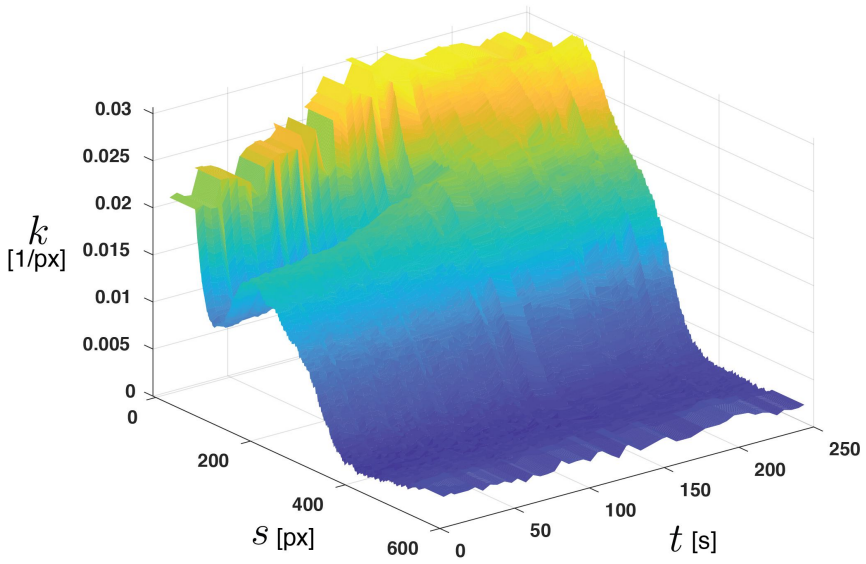


Figure 5.7: Arclength and curvature evolution over time of the tendril after stimulation.

5.5 SUMMARY

In this chapter, we presented an image-based reconstruction approach based on 2D piece-wise clothoid model. This method describes and analyzes the different morphologies assumed by a natural tendril after mechanical stimuli. Starting from our previous work [30], we further improved the sorting skeletonization algorithm with tuning weights, which is able to solve the problem of the direction vector being misled by the occurrence of sharp corners. In addition, we presented an automatic quantity selection method by dynamic programming to identify the optimal segment number of the 2D piece-wise clothoid to fit the curling shape.

Our method is quantitatively verified by a set of representative images extracted from a video[2] showing the shape variation in a *passionflower* tendril. We find that from 4 to 6 segments were enough to describe with high accuracy ($R^2 > 0.9$) the tendril shape across different stages of curling evolution.

However, we analyzed only 2D images of tendrils having relatively limited complexity. We actually neglected highly self-occluded tendrils or interference from non-interest regions. This condition can easily occur in nature but that can be better analyzed in a 3D extension of the present work, which will be implemented in the next chapter.

6

NONLINEAR MORPHOLOGY ANALYSIS OF 3D CURLING SHAPE PIECEWISE RECONSTRUCTION

This chapter is extracted from
"An Image-Based Method for the Morphological Analysis of Tendrils with 2D Piece-Wise Clothoid Approximation Model"
J. Fan, F. Visentin, E. Del Dottore, B. Mazzolai
Submitted to International Journal of Computer Vision 2022

6.1 INTRODUCTION

Based on the previous two chapters' work on 2D planar curling shape reconstruction, we extend to the 3D case in this chapter by considering the off-plane situation. The work of this chapter is structured as follows: Section 6.2 introduces the setup of biological experiment for morphology observation and data collection. Then we present in details the algorithms of shape reconstruction starting from the preprocessing of the videos, ordering skeleton up to the identification of the correspondence between the points. The section also contains the mathematical definition of the piecewise Clothoid spiral, the model we used for the reconstruction of the generated 3D point cloud. Considering the evolution of tendrils' morphology as an example, in Section 6.5 we present a validation of the proposed methodology providing both the results of the process and some consideration on the different morphological, temporal evolutions. Finally, discussion, conclusion, and future works are presented in Section 6.6.

6.2 BIOLOGICAL MORPHOLOGY EXPERIMENT

6.2.1 *Plant*

In order to prove the capabilities of the proposed three-dimensional reconstruction methodology, we decided to focus on a single species of plant, the *Passiflora caerulea*, and use the extracted features to analyze the curling behavior and movement of its tendrils. The plants were purchased from a local flower store during winter time and all the experiments were carried out in the same season. All the specimens

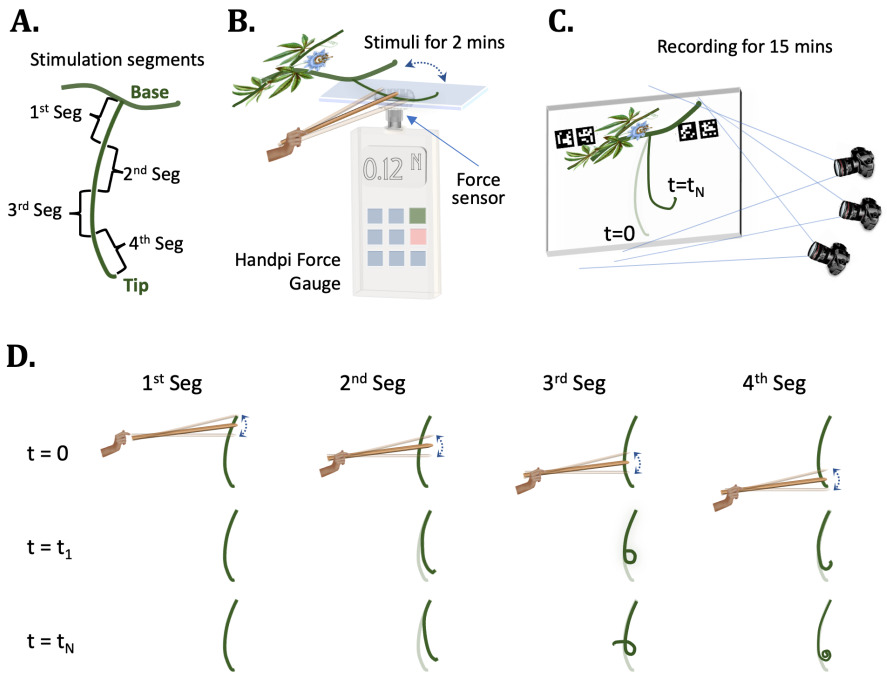


Figure 6.1: Biological experiment setup and data collection procedure. **A**. Definition of the portions of the tendril stimulated in the experiments. In this work we subdivide each tendril in four segments and we only stimulated one using a wood stick. **B**. Measurements of the applied force during the experiments. To ensure that the stimulus remains the same for all the experiments, we first measured the interaction with a precision load cell, then we replicate the same motion over the selected portion of the tendril. **C**. Experimental setup. After the stimulation, the main stem of the plant was taped on a panel leaving the tendril hanging free. On the panel, there are unique markers used to facilitate the processing of the data and to identify common features in the three views used for the 3D reconstruction. **D**. Schematic representation of the stimuli-induced morphological changes occurred over time in the four experimental sets.

tendrils in the experiments were chosen from the same plant, that was kept in a growing chamber at 23 °C, with 70% relative humidity and a day/night cycle of 12/12 hours. Since matured tendrils can show maximum irritability and little change in their thigmotropic sensitivity, we chose tendrils on their maturity phase, having a length of about $14.8 - 24\ cm$.

6.2.2 *Experiment Setup*

In our previous studies [30, 31], we focused only on the two-dimensional analysis of the morphology change in the tendril as a consequence of a contact occurred in a single area. In this work, we focus on the extension to the 3D and further analyse the effects of a constant force

applied on different points along the length of the tendril. In fact, since the sensitivity of a tendril is not evenly distributed along its body, and decreases as the distance from the tip increases [56, 57], we divided the tendril into four stimulation portions (namely **S1**, **S2**, **S3**, and **S4**) whose located length is evenly divided along the total length of a tendril (shown in Figure 6.1A). The first portion starts from the stem (base of the tendril) while the last part is close to the tendril apical extremity. One portion corresponds to one experimental set. We repeated the same experimental procedure in each portion using four different tendrils from the same plant of *Passiflora caerulea* for a total of sixteen experiments divided into four groups (see Figure 6.1A).

To ensure a consistent stimulation, we verified the force applied by first adhering one side of a glass slide on a digital Force Gauge (Handpi Force Gauge HP-50) equipped with a highly sensitive force sensor (with 0.01 N resolution, 10 N capacity), and the other side on the tendril dorsal side (illustrated in Figure 6.1B).

Then, we continuously stimulate back and forth the selected segment for 2 minutes (frequency: $f = 40$ times/min, stroking force: $F = 0.12$ N) using a wooden stick. After the stimulation, the tendril was let hanging free and the main shoot was taped on a whiteboard (shown in Figure 6.1C), to limit possible oscillations and interference introduced by the motion of the stem that can cause unwanted contact with other parts of the plant. In addition, to limit other possible environmental stimuli affecting the results, we performed the experiments in the same growing chamber under consistent environmental settings as defined in the above subsection.

6.2.3 *Datasets Collection*

The response of the tendril is quite rapid showing initial movements already after few seconds after the stimulus. However, to fully complete its motion, the tendril requires different timing depending on the location of contact. Thus, we decided to acquire 15 minutes of video enough to cover the whole motion for each considered case. Three cameras (Pentax WG-III with Lens $25 - 100$ mm) were placed in different, fixed positions having a relative angle of 60° and at a distance from the tendril of 50 cm. As reference, we located multiple ArUco markers close to the tendril under observation (Figure 6.1C). A schematic representation of all the considered cases and relative outputs are depicted in Figure 6.1D. From the experiments we observed that the morphological changes of tendrils in response to the same stimulus applied on different segments can be divided into two categories: the ones that produce curling on a plane (stimulus performed in the **S1**, **S2**, and **S4** segment), and the one that curls off-plane (segment **S3**) which visually generates a sort of cross-intersection of the tendril (Figure 6.1D, third column, bottom row). This initial ob-

servation guided the development of the algorithm used for the 3D reconstruction.

6.3 SHAPE RECONSTRUCTION

Reconstructing such tendril-like slender structure with and without cross-intersection in traditional curve-based and feature points-based methods is extremely difficult due to their peculiar characteristics such as lack of features, fine elements, smoothness, and self-occlusions. We present a novel vision-based method to reconstruct its spatial morphologies in three-dimensional space.

After the morphology experiment, we directly obtain data in video format from three different but close perspectives (namely by $\mathcal{V}_1$, $\mathcal{V}_2$ and $\mathcal{V}_3$). In each scenario, the ArUco markers on the background (see Figure 6.1-**C**) are used for the extraction of camera parameters (i. e., both intrinsic parameters matrix $\mathbf{K}$ and extrinsic parameters matrix $[\mathbf{R}|\mathbf{t}]$) and their correspondent corners points simultaneously detected in all views are prepared for the homography transformation process in the following section. The key part of shape reconstruction is to seek the points correspondence from the interest tendril in all perspective images. Here, considering the tendril structure with the peculiar characters of thin and not long element, we extract the target tendril from each view $\mathcal{V}_{i=1,2,3}$, thin and skeletonize them into discrete and disordered points, then order and correspond them after view re-projection (i. e., re-project $\mathcal{V}_1$ and $\mathcal{V}_3$ to $\mathcal{V}_2$ using perspective projection of camera matrices). To achieve this goal, we decomposed the overall procedure of shape reconstruction into 3 sub-tasks :

- Segmentation of target tendril from complex environment;
- Re-order skeletonized tendril with/without the cross-intersection occurrence;
- Perform points correspondence after re-projection of perspectives.

6.3.1 *Pre-processing*

The process starts with the acquisition of the data from three different perspectives (namely $\mathcal{V}_1$, $\mathcal{V}_2$, and $\mathcal{V}_3$) using the cameras. The objective is to match the correspondence between the images, extract the points, and reconstruct a three-dimensional model of the tendril. A crucial step is the extraction of the cameras parameters, needed for the reconstruction. We used the ArUco markers (Figure 6.1C) placed on a flat surface to compute the cameras parameters (i. e., both intrinsic parameters matrix, $\mathbf{K}$, and extrinsic parameters matrix, $[\mathbf{R}|\mathbf{t}]$) and a set

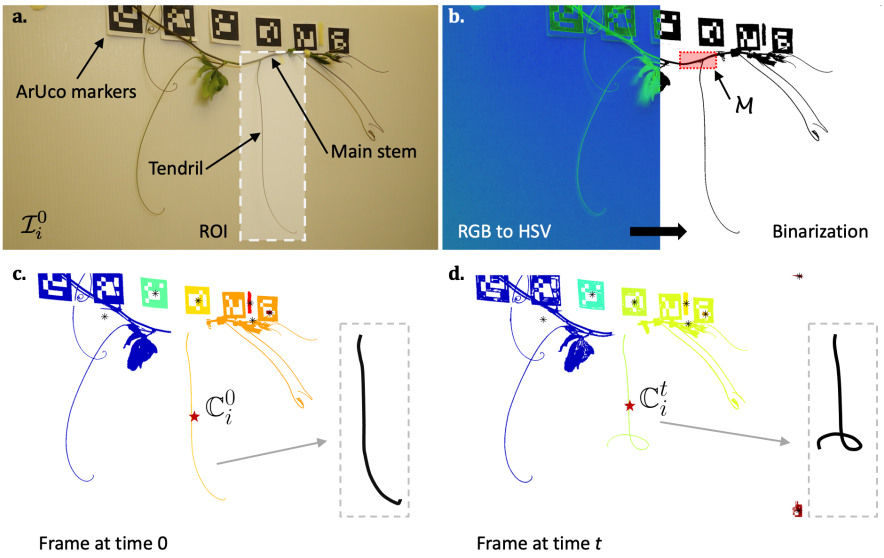


Figure 6.2: Steps involved in the prepossessing of each of the captured videos. **A**. The first frame of each video, $\mathcal{I}_i^0$ ($i = 1,2,3$), is processed in a semi-automatic fashion, the user is asked to select a ROI which contains the element to be analysed (i.e., a tendril). The ArUco markers are attached to the background and they serve as fixed correspondence between the images captured by the three cameras, but also to retrieve the cameras parameters. **B**. The RGB image is then converted in HSV color space (left) and thresholded to extract the foreground (i.e., the selected tendril) from the background (right). Again, we ask the user to select the connection point between the main stem and the tendril in order to avoid the segmentation algorithm to proceed further into selecting points not belonging to the tendril. **C**. Using the connected components algorithm each set of pixels is labeled according to its connections with the neighbouring ones. Then, the centroid, $\mathbb{C}_i^0$ (i is the $i-th$ camera), for the pixels contained in the ROI is computed and stored to automate the process for the following frames. The result of this phase is a set of pixels belonging to the tendril. **D**. The results of the automatic extraction of the tendril using the updated centroid, $\mathbb{C}_i^{t-1}$ (where $t-1$ is the time frame and i is the i-th camera), and considering only the portion of the image contained in the ROI defined in $\mathcal{I}_i^0$.

of their corner-points used to match the three views by a homography transformation.

Before proceeding with the 3D-reconstruction, each frame has to be processed to extract the Region of Interest (ROI) that contains the tendril and to isolate it from the background. The problem is not simple to solve automatically since the scene is cluttered by the presence of stem, leaves, other tendrils. For this reason, a semi-automatic procedure has been developed: the user selects only for the initial frame ($\mathcal{I}_i^0$, $i = 1,2,3$ corresponding to each view $\mathcal{V}_{i=1,2,3}$) the ROI, while for the followings it is automatically updated. In addition, to

avoid the algorithm to select unwanted pixels from the stem, the user is asked to draw an additional, rectangular region at the intersection point between the tendril and the main stem. This area is used as a keep-out mask, $\mathcal{M}$, in the segmentation process. The image is then converted from Red Green Blue (RGB) to Hue Saturation Value (HSV) color space to highlight the difference between the background and foreground. In fact, the living tendril has not a uniform color that can be directly processed in the RGB space. The resulting image is then binarized by thresholding. The segmentation is performed by computing the connected components which returns sets of pixels and their relative labels. Only the labeled pixel-set contained in the ROI is then further processed by computing their centroid, $\mathbb{C}_i^0$. All the remaining are then removed from the image producing an output of only a series of unordered pixels belonging to the selected tendril. Figure 6.2 depicts the steps involved in the pre-processing of the data.

For the remaining frames, $\mathcal{I}_i^t$ $(i = 1, 2, 3;\ t = 1, \ldots, m)$, the selection of the correct labeled set of pixels is done automatically. At time t, for each labeled set of pixels is computed the centroid and, $\mathbb{C}_i^t$ is selected the one that minimizes the distance from the selected one in previous frame, $\mathbb{C}_i^{t-1}$, by the use of K-Nearest Neighbour Search (K-NN).

6.3.2 *Ordering Skeleton Points*

The pre-processing phase returns a set of unordered pixels which represent the skeleton of the tendril. In order to perform all the remaining steps and to ensure a correct three-dimensional reconstruction, those points should be ordered. During the experiments, we noticed that the change in the morphology of the tendril either happens in-plane or off-plane. We hereby define the ordering direction which corresponds to the direction of natural growth or to the direction that goes from base to tip of tendril as the correct one (see Figure 6.1-**A**). According to the observation of distinctly different morphological changes (with-/without cross-intersection) after the application of stimuli in specific locations, we should order these unarranged points by different cases as well.

(a) ***without cross-intersection (in-plane)*** In our previous research [30], we proposed the `CollectNeighboringPoints` algorithm based on the Moving Least Squares Method (MLSM) to sort a set of planar points set without intersection. This algorithm needs to start from a random chosen point in the skeleton, and to order the points in one predefined direction, then sort the remaining points in an opposite direction, and finally merge them together.

We first choose the midpoint $\mathbf{p}_m$ of the lower boundary of the rectangle mask $\mathcal{M}$ and find one closest point in the segmented skeleton to $\mathbf{p}_m$ as the starting point $\mathbf{p}_s$ by K-NN algorithm (as shown in Figure 6.3-**A**). Next from $\mathbf{p}_s$, for each point $\mathbf{p}_k$ encountered in the skeleton, we

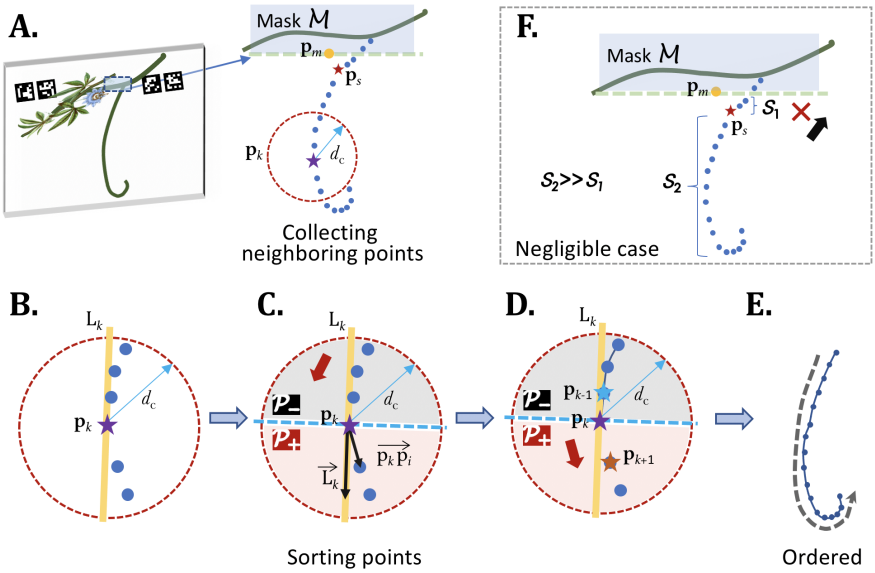


Figure 6.3: The sorting algorithm of the disordered points without cross-intersection. The algorithm starts from point $\mathbf{p}_s$, which is obtained from its closest middle bottom point $\mathbf{p}_m$ of the mask $\mathcal{M}$. The subfigures from left to right are **A.** collecting neighboring points around the current point $\mathbf{p}_k$ (marked as a purpler star) within an appropriate collection radius d_c; **B.** fitting all the collected neighbors in a straight line $\mathbf{L}_k$ by MLSM; **C.** and then classify the collected neighboring points into $\mathcal{P}_+$ and $\mathcal{P}_-$. **D.** The next sorting candidate point $\mathbf{p}_{k+1}$ (marked as brown star) is the nearest point to $\mathbf{p}_k$. It lies in the class which is different from $\mathbf{p}_{k-1}$ (marked as azure star). **F.** Both direction from point $\mathbf{p}_s$ will be sorted into set $\mathcal{S}_1$ and $\mathcal{S}_2$. However, we only consider the direction which has a larger length, i. e., $\mathcal{S}_2 >> \mathcal{S}_1$. The final sorting result is shown in subfigure **E.**

collect its neighbouring points along the prescribed direction (either to base or to tip end in our experiment) within an appropriate collection radius $d_c \leq R$ (R is a pre-defined value, representing the maximum radius for points collection). All the selected neighbouring points should be fitted into a 2D straight line, i. e., $\mathbf{L}_k : Ax + By + C = 0$ obtained by MLSM. Meanwhile, it should satisfy a correlation index ($\rho_k \geq 0.9$) by increasing the collection radius d_c, in order to include more data points (shown in Figure 6.3-**B**). After the points collection, the sorting direction is determined by a two-sides classifier, where each class represents one of the two possible directions (Figure 6.3-**C**). For the correct linear fitting and accurate classification [31], we introduce tuning weights w_i for each neighbouring point $\mathbf{p}_i$. It is based on the distance distribution with respect to $\mathbf{p}_k$, by indicating the contributed importance for fitting. Here, w_i is define by,

$$\begin{aligned} w_i &= e^{-0.01r^2/R^2} \\ r &= \|\mathbf{p}_i - \mathbf{p}_k\|_2 \end{aligned} \tag{6.1}$$

The classification is achieved by performing the cross product between the vectors of the collected neighbouring points $\overrightarrow{\mathbf{p}_k\mathbf{p}_i}$ over the direction vector of the fitting line $\overrightarrow{\mathbf{L}_k}$. According to the results, we divide them into two classes,

$$\begin{aligned} \mathbf{p}_i \in \mathcal{P}_+ &: \overrightarrow{\mathbf{p}_k\mathbf{p}_i} \times \overrightarrow{\mathbf{L}_k} > 0 \\ \mathbf{p}_i \in \mathcal{P}_- &: \overrightarrow{\mathbf{p}_k\mathbf{p}_i} \times \overrightarrow{\mathbf{L}_k} < 0 \end{aligned} \tag{6.2}$$

where $\mathcal{P}_+$ and $\mathcal{P}_-$ are the classified two point sets. It is easily accessible to find the previous sorted point $\mathbf{p}_{k-1}$ falls into one of the classified sets. Therefore, the next sorting candidate point $\mathbf{p}_{k+1}$ will lie inside the other set, which is opposite to $\mathbf{p}_{k-1}$. It is obtained by picking the one with nearest Euclidean distance from $\mathbf{p}_k$ (as shown in Figure 6.3-**D**)). Then this algorithm is iterated to update the sorting candidate points. As Figure 6.3-**F**, we are able to obtain $\mathcal{S}_1$ and $\mathcal{S}_2$ until both directions from $\mathbf{p}_s$ are sorted. For the sake of simplification, we compare the number of points in $\mathcal{S}_1$ and $\mathcal{S}_2$, and delete the shorter one. It is because our specific choice of the starting point $\mathbf{p}_s$ ensures a negligible part from $\mathbf{p}_s$ to the base (normally less than three points for our experimental setup) regarding our reconstruction.

(b) ***with cross-intersection (off-plane)*** Compare to the above algorithm, this section needs a process involving cross-intersection occurring in the 2D images. When the cross-intersection appears, the algorithm is divided into two categories according to whether the tip of the tendril is far away from the intersection, as shown in Figure 6.4. Subfigure **A** is the case with the tip close to cross-point. Subfigure **B** is the other case, where the tendril segment from the cross-point to the tip cannot be ignored.

For case **A**, we are able to first find the cross-point through a binarized image with curve segments. This cross-point $\mathbf{p}_c$ is the junction of the curve edges, which is indicated by the red triangular marker in subfigure **A-b**. We apply the function `findendsjunctions.m` from the edge linking and line segment fitting package introduced by Peter Kovesi [65]. Similarly, we can reuse the above sorting algorithm without cross-intersection for the tendril segment from initial point $\mathbf{p}_s$ (marked by red star) to the cross-point $\mathbf{p}_c$. We denote this sorted segment by $\mathcal{S}_1$. For the segment from $\mathbf{p}_c$ to tip end (denoted as $\mathcal{S}_2$), the above proposed algorithm may result into two possible sorting directions, i.e., clockwise and counterclockwise, as shown by the arrows in subfigure **A-e**. To simplify coding, we can just select one of the sorting direction, and then reverse the result to solve both possible cases. We name by $\mathcal{S}_2$ and $\mathcal{S}_2^*$, and $*$ indicates the reverse ordering of $\mathcal{S}_2$. However, one of them (clockwise sorting shown in the subfigure) is not consistent with the natural growing direction. It could be suffered from the image resolution, inaccurate skeletonization or noisy points close to the cross-point. Thus, we propose the following rules to filtering out these cases. Firstly, we select the last N_1 number of points from

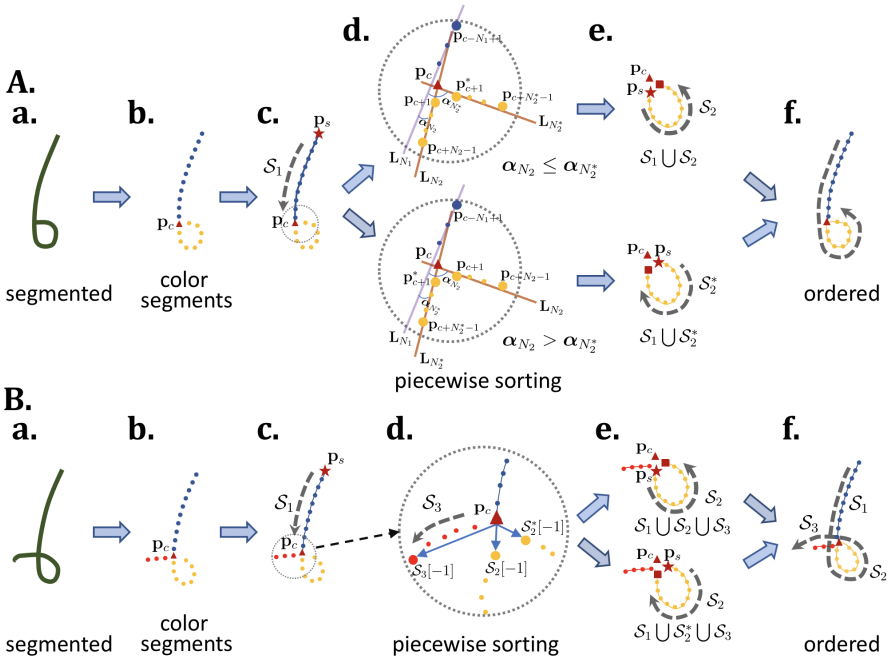


Figure 6.4: the sorting algorithm while one cross-intersection. **A.Tip close to cross-intersection:** the segmented tendril with disordered points are divided into several points sets and colored in pieces. Then, the sorting algorithm starts from the starting point (red star) and ends at the point marked by red square. The grey dash line represents the sorting direction. The circle numbers represent the current sorted points set, while the rest points sets are in semi-transparent color. In this case, it needs the user input to decide the sorting direction for the second points set. Finally, we obtain the ordered skeleton in purple. **B.Tip far away from cross-intersection:** the first three steps are the same as **A**. Next, for the second points set, there are three options chosen by user input, which depends on the distance among the vectors and manual confirmation. Then, we sort the third points set and obtain the whole ordered skeleton.

segment $\mathcal{S}_1$, i. e.$\{\mathbf{p}_{c-N_1+1}, \mathbf{p}_{c-N_1+2}, \cdots, \mathbf{p}_c\}$. For $\mathcal{S}_2$, we select the first N_2 and N_2^* number of points respectively, i.e., $\{\mathbf{p}_c, \mathbf{p}_{c+1}, \cdots, \mathbf{p}_{c+N_2-1}\}$, or $\left\{\mathbf{p}_c, \mathbf{p}^*_{c+1}, \cdots, \mathbf{p}^*_{c+N_2-1}\right\}$. Then for each of these point sets, we fit them into 3 lines, and denoted as $\mathbf{L}_{N_1}$, $\mathbf{L}_{N_2}$ and $\mathbf{L}_{N_2^*}$. Next, we are able to compute the angles between line pairs $\langle \mathbf{L}_{N_1}, \mathbf{L}_{N_2} \rangle$ and $\langle \mathbf{L}_{N_1}, \mathbf{L}_{N_2^*} \rangle$ by,

$$\boldsymbol{\alpha}_j = \texttt{tan}^{-1}\left(\texttt{det}\left(\left[\overrightarrow{\mathbf{L}_{N_1}}; \overrightarrow{\mathbf{L}_j}\right]\right), \texttt{dot}\left(\overrightarrow{\mathbf{L}_{N_1}}, \overrightarrow{\mathbf{L}_j}\right)\right), \quad j = N_2, N_2^* \tag{6.3}$$

where j indicates the angles between $\mathbf{L}_{N_1}$ and $\mathbf{L}_{N_j}$. Thus, we are able to identify the correct sorting direction of whole tendril by comparing the value of these two angles,

$$\mathcal{S} = \begin{cases} \mathcal{S}_1 \bigcup \mathcal{S}_2, & if\ \boldsymbol{\alpha}_{N_2} \leq \boldsymbol{\alpha}_{N_2^*} \\ \mathcal{S}_1 \bigcup \mathcal{S}_2^*, & if\ \boldsymbol{\alpha}_{N_2} > \boldsymbol{\alpha}_{N_2^*} \end{cases} \tag{6.4}$$

Due to the smooth and continuous curvature changes over the tendril length, this sorting result will output a reasonable direction regarding the natural growth of the tendril.

For the other case as shown in subfigure **B**, the segment from cross-point $\mathbf{p}_c$ to the tip end is not negligible. Thus, the whole tendirl will be divided into three segments. We can apply the same sorting technique for each segment from the above case without cross-intersection. The first segment $\mathcal{S}_1$ can be found easily. However, the difficulty lies in finding the correct sorting direction starting from the cross-point $\mathbf{p}_c$. For this case, it may falls into three possible sorting directions. As we already know, two of them belong to segment $\mathcal{S}_2$. The correct sorting that corresponds to the natural growth direction, can be found by angles of fitted lines. We need to identify which is the segment $\mathcal{S}_3$, in order to distinguish from segment $\mathcal{S}_2$. This can be done by finding the Euclidean distance from $\mathbf{p}_c$ to the last point of each segment. Apparently, we have the following relationship,

$$\begin{aligned} \|\mathbf{p}_c - \mathcal{S}_3[-1]\| &> \|\mathbf{p}_c - \mathcal{S}_2[-1]\| \\ \|\mathbf{p}_c - \mathcal{S}_3[-1]\| &> \|\mathbf{p}_c - \mathcal{S}_2^*[-1]\| \end{aligned} \tag{6.5}$$

where the writing $[-1]$ indicates the last element of the respective segment. We can easily conclude that $\mathcal{S}_3$ has a longer distance, than both clockwise and counterclockwise direction of $\mathcal{S}_2$. Therefore, $\mathcal{S}_3$ can be confirmed, which will give us,

$$\mathcal{S} = \begin{cases} \mathcal{S}_1 \bigcup \mathcal{S}_2 \bigcup \mathcal{S}_3, & if\ \boldsymbol{\alpha}_{N_2} \leq \boldsymbol{\alpha}_{N_2^*} \\ \mathcal{S}_1 \bigcup \mathcal{S}_2^* \bigcup \mathcal{S}_3, & if\ \boldsymbol{\alpha}_{N_2} > \boldsymbol{\alpha}_{N_2^*} \end{cases} \tag{6.6}$$

The above processing operations of segmentation and points-sorting are performed for the videos in all perspectives.

6.3.3 *Mapping Points Between Views*

Once $\mathcal{S}$ is obtained in each $\mathcal{V}_1$, $\mathcal{V}_2$ and $\mathcal{V}_3$, we need to define a point-to-point correspondence between views. The first step involves a homographic projection between the views taking $\mathcal{V}_2$ as a reference. The ArUco marker has been used as reference in the computation of the homography matrix $\mathcal{H}_{1,2}$ and $\mathcal{H}_{3,2}$. As a result we obtain a projection of the points in $\mathcal{V}_1$ and $\mathcal{V}_3$ onto $\mathcal{V}_2$ (Figure 6.5A). This allows to find the point-to-point correspondence between views using the same reference. Given two curves $\mathcal{S}_p$ and $\mathcal{S}_q$ in a metric space composed by order-preserving sets of points, it is possible to find the correspondence between the curves using the Fréchet distance [131]. This is a measure of similarity between curves that takes into account the location and ordering of the points along the curves.

Let $\mathcal{S}_p = \{u_1, ..., u_p\}$ and $\mathcal{S}_q = \{v_1, ..., v_q\}$ be the corresponding sequences, we want to find the mapping between points

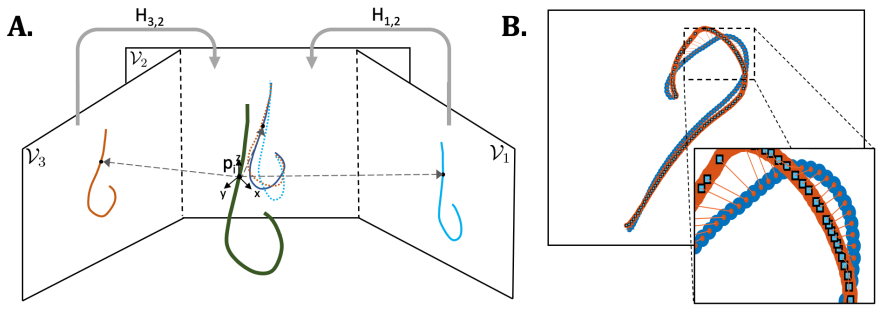


Figure 6.5: The process of mapping the points between the views. **A**. Homographic transformation between the views to position all the points with respect to a single reference frame. **B**. Application of the Fréchet distance to map the extracted set of points. When a set of correspondence has been found is possible to properly triangulate the points and retrive the three-dimensional shape of the original curve.

$$\left(u_{a_1}, v_{b_1}\right), \left(u_{a_2}, v_{b_2}\right), \ldots, \left(u_{a_m}, v_{b_m}\right) \tag{6.7}$$

where $a_1 = 1$, $b_1 = 1$ and $a_m = p$, $b_m = q$, that minimizes the disparity for 3D triangulation-based reconstruction between the points.

The mapping has also to respect the order of the points by $a_{i+1} = a_i + 1$ and $b_{i+1} = b_i + 1$. Considering that the sets of points have been sorted, we define the discrete Fréchet distance denoted as $\delta_F\left(\mathcal{S}_p, \mathcal{S}_q\right)$ by:

$$\delta_F\left(\mathcal{S}_p, \mathcal{S}_q\right) = \inf_{a_i, b_i} \max_{i=1,\ldots,m} \left\{ \texttt{dis}\left(u_{a_i}, v_{b_i}\right) \right\} \tag{6.8}$$

where `dis` is the Euclidean distance between one pair of points, and inf is the infimum over all parameterization of a_i and b_i. Before applying the Fréchet distance, we uniformly sample k $(k = 200)$ points from each view for consistency during processing. After the mapping, the sampled points are back-projected in their original view using the same homographic transformation. Lastly, through triangulation we project the 2D points in the 3D space (via `triangulateMultiview` function from MATLAB) to obtain the discrete 3D curve points

$$\mathcal{C} = \left\{\mathbf{c}_1, \mathbf{c}_2, \cdots, \mathbf{c}_k\right\}. \tag{6.9}$$

6.4 SHAPE MODELING

6.4.1 *Discrete Frenet-Serrat Point Fitting*

To describe the shape of the tendril from the reconstructed 3D points we adopt a 3D Clothoid curve fitting with piecewise approximation. We already investigated the same approach in 2D [31], here we extend

the same approach to the three-dimensional domain. To do so, in addition to the curvature, it is fundamental to retrieve also the information on the torsion.

Following the definition in Frenet-Serret frame as in [45], a 3D curve is defined by:

$$\mathcal{C}(s) = \int_0^s \mathbf{T}(u)\,\mathrm{d}u + \mathbf{c}_0 = \int_0^s \left[\int_0^t \frac{\mathrm{d}\mathbf{T}(u)}{\mathrm{d}u}\mathrm{d}u + \mathbf{T}_0\right]\mathrm{d}t + \mathbf{c}_0 \quad (6.10)$$

where the Frenet–Serret frame vectors are given by,

$$\begin{aligned}
\frac{\mathrm{d}\mathbf{T}(s)}{\mathrm{d}s} &= \kappa(s)\mathbf{N}(s) \\
\frac{\mathrm{d}\mathbf{N}(s)}{\mathrm{d}s} &= -\kappa(s)\mathbf{T}(s) + \tau(s)\mathbf{B}(s) \\
\frac{\mathrm{d}\mathbf{B}(s)}{\mathrm{d}s} &= -\tau(s)\mathbf{N}(s)
\end{aligned} \quad (6.11)$$

and $\kappa(s)$ and $\tau(s)$ are respectively curvature and torsion, having linearity relationship with curve length:

$$\begin{aligned}
\kappa(s) &= \kappa_0' s + \kappa_0 \\
\tau(s) &= \tau_0' s + \tau_0
\end{aligned} \quad (6.12)$$

In case of a discrete set of points, as already investigated in [52, 75], it is possible to describe the Frenet-Serret frame as follows. For a given point $\mathbf{c}_i$ located in the set of 3D points $\mathcal{C}$, we can define a sequence of the recursively discrete frame as $\mathcal{F}_i = (\mathbf{T}_i, \mathbf{N}_i, \mathbf{B}_i)$. The unit tangent vector can be given as:

$$\mathbf{T}_i = \frac{\mathbf{c}_{i+1} - \mathbf{c}_i}{|\mathbf{c}_{i+1} - \mathbf{c}_i|} \quad (6.13)$$

Then, the bi-normal and normal vectors can be defined by:

$$\begin{aligned}
\mathbf{N}_i &= \frac{\mathbf{T}_i - \mathbf{T}_{i-1}}{|\mathbf{T}_i - \mathbf{T}_{i-1}|} \\
\mathbf{B}_i &= \mathbf{T}_i \times \mathbf{N}_i
\end{aligned} \quad (6.14)$$

It should be noticed that there will be no discrete Frenet frames defined for the first and the last point, due to the dependence of calculation requiring at least three neighboring points. From the above equations, the discrete curvature and torsion can be derived as,

$$\begin{aligned}
\kappa_i &= \|\mathbf{T}_i - \mathbf{T}_{i-1}\| \\
\tau_i &= \frac{\mathbf{B}_i - \mathbf{B}_{i-1}}{|\mathbf{N}_i|}.
\end{aligned} \quad (6.15)$$

6.4.2 *Automatic Piecewise Fitting of Curvature & Torsion*

In order to guarantee the curvature-torsion continuity, we fit linearly the two quantities independently. However, the linearity of the Clothoid curve, as in Equation 6.12, should be preserved simultaneously. As in our previous implementation [31], we used dynamic programming to minimize the number of line segments and the fitting error. The objective functions of our optimization problem are:

$$\begin{aligned}\mathcal{J}_{\boldsymbol{\kappa}}\left(\mathbf{c}_a, \mathbf{c}_b\right) &= \min_{a<m<b}\left\{\mathcal{J}_{\boldsymbol{\kappa}}\left(\mathbf{c}_a, \mathbf{c}_m\right) + \mathcal{J}_{\boldsymbol{\kappa}}\left(\mathbf{c}_m, \mathbf{c}_b\right), \epsilon_{\boldsymbol{\kappa}} + \mathcal{E}_{\boldsymbol{\kappa}}^{fit}\left(\mathbf{c}_a, \mathbf{c}_b\right)\right\} \\ \mathcal{J}_{\boldsymbol{\tau}}\left(\mathbf{c}_e, \mathbf{c}_f\right) &= \min_{e<n<f}\left\{\mathcal{J}_{\boldsymbol{\tau}}\left(\mathbf{c}_e, \mathbf{c}_n\right) + \mathcal{J}_{\boldsymbol{\tau}}\left(\mathbf{c}_n, \mathbf{c}_f\right), \epsilon_{\boldsymbol{\tau}} + \mathcal{E}_{\boldsymbol{\tau}}^{fit}\left(\mathbf{c}_e, \mathbf{c}_f\right)\right\}\end{aligned} \tag{6.16}$$

where $\mathcal{J}_{\{\boldsymbol{\kappa}\}}$ and $\mathcal{J}_{\{\boldsymbol{\tau}\}}$ are the costs of fitting error for curvature, $\boldsymbol{\kappa}$, and torsion,$\boldsymbol{\tau}$ between two points.

On the right hand of the equation, $\epsilon_{\{\boldsymbol{\kappa}\}}$ and $\epsilon_{\{\boldsymbol{\tau}\}}$ are the constant penalty terms for adding a new segment. $\mathcal{E}_{\{\boldsymbol{\kappa}\}}^{fit}$ and $\mathcal{E}_{\{\boldsymbol{\tau}\}}^{fit}$ are the least-square fitting errors for linear regression of line segments, that is:

$$\begin{aligned}\mathcal{E}_{\boldsymbol{\kappa}}^{fit}\left(\mathbf{c}_a, \mathbf{c}_b\right) &= \min_{\alpha_{\boldsymbol{\kappa}}, \beta_{\boldsymbol{\kappa}}}\left(\sum_{t=a}^{b}\left|\alpha_{\boldsymbol{\kappa}} \cdot s(\mathbf{c}_t) + \beta_{\boldsymbol{\kappa}} - \kappa_t\right|\right) \\ \mathcal{E}_{\boldsymbol{\tau}}^{fit}\left(\mathbf{c}_e, \mathbf{c}_f\right) &= \min_{\alpha_{\boldsymbol{\tau}}, \beta_{\boldsymbol{\tau}}}\left(\sum_{t=e}^{f}\left|\alpha_{\boldsymbol{\tau}} \cdot s(\mathbf{c}_t) + \beta_{\boldsymbol{\tau}} - \tau_t\right|\right)\end{aligned} \tag{6.17}$$

with $\alpha_{\{\boldsymbol{\kappa}\}}$, $\alpha_{\{\boldsymbol{\tau}\}}$, $\beta_{\{\boldsymbol{\kappa}\}}$, and $\beta_{\{\boldsymbol{\tau}\}}$ being the slopes and intercepts of the least-square fitting line segments. The variables $s(\mathbf{c}_t)$, κ_t and τ_t are the arc-length, curvature and torsion at point $\mathbf{c}_t$, respectively.

Therefore, we are able to find the optimal automatic segmentation for curvature and torsion with M and N segments respectively. Ideally, we expect the curvature/torsion continuity for neighbouring pairs of segments. That is, for the intersection points between i^{th} and $(i+1)^{th}$ segment at $\mathbf{c}_{\boldsymbol{\kappa},i+1}$ and $\mathbf{c}_{\boldsymbol{\tau},i+1}$, the curvature and torsion at end-point of i^{th} segment should be matched with the start-point of the $(i+1)^{th}$ segment as:

$$\begin{aligned}\alpha_{\boldsymbol{\kappa},i} \cdot s(\mathbf{c}_{\boldsymbol{\kappa},i+1}) + \beta_{\boldsymbol{\kappa},i} &= \alpha_{\boldsymbol{\kappa},i+1} \cdot s(\mathbf{c}_{\boldsymbol{\kappa},i+1}) + \beta_{\boldsymbol{\kappa},i+1} \\ \alpha_{\boldsymbol{\tau},i} \cdot s(\mathbf{c}_{\boldsymbol{\tau},i+1}) + \beta_{\boldsymbol{\tau},i} &= \alpha_{\boldsymbol{\tau},i+1} \cdot s(\mathbf{c}_{\boldsymbol{\tau},i+1}) + \beta_{\boldsymbol{\tau},i+1}.\end{aligned} \tag{6.18}$$

Even though the start-end point between adjacent segments has been connected, the above curvature/torsion continuity may be violated. The reason is not taking into consideration intersection constraints in both curvature and torsion space. To solve this interconnection problem, we proposed algorithm 4 by returning of refined segmentation point list $\mathcal{S}_{\boldsymbol{\kappa}}$ (taking curvature as an example). The idea is to connect adjacent segments sequentially by satisfying Equation 6.18. Mathematically, we can achieve this by calculation of the slopes and intercepts for each pair of adjacent segments, in order to find the

refined interconnection points. However, this approach may cause an overshooting problem – i. e., the refined point lies outside of the two boundary points for the corresponding adjacent segments. Thus, we proposed a compensation procedure in the second part of algorithm 4. The idea behind this is to simply combine these adjacent segments if the overshooting occurs.

Algorithm 4: Refine of automatic segmentation considering interconnection and overshooting problems (taking curvature segments κ for example)

Input : The original linear fitting parameters for each segment, $\alpha_{\kappa,i}$ and $\beta_{\kappa,i}$

Output: Refined segments point list without overshooting $\mathcal{S}_\kappa = \{(\mathbf{s}_{\kappa,1}, \kappa_1), (\mathbf{s}_{\kappa,2}, \kappa_2), \cdots (\mathbf{s}_{\kappa,M}, \kappa_M)\}$

```
// the following is going to solve for interconnection problem
// initialize an empty refined segments point list
```

$\bar{\mathcal{S}}_\kappa \leftarrow$ `empty`

for *each adjacent segments pair id* $(i, i+1)$ *in* $\mathbf{c}_\kappa$ **do**

  $A_1, B_1 \leftarrow \alpha_{\kappa,i}, \beta_{\kappa,i}$

  $A_2, B_2 \leftarrow \alpha_{\kappa,i+1}, \beta_{\kappa,i+1}$

  $x \leftarrow \dfrac{B_2 - B_1}{A_1 - A_2}$

  $y \leftarrow A_1 \cdot x + B_1$

  `// adding a refined intersection point into segment point list`

  $\bar{\mathcal{S}}_\kappa \leftarrow \{\bar{\mathcal{S}}_\kappa, (x, y)\}$

```
// the following is going to compensate for overshooting problem
// initialize no-overshooting segments point list
```

$\mathcal{S}_\kappa \leftarrow \bar{\mathcal{S}}_\kappa$

$\mathfrak{F} \leftarrow$ `True`

while $\mathfrak{F}$ **do**

  `// get length of current no-overshooting segments point list`

  $K \leftarrow$ `len` $(\mathcal{S}_\kappa)$

  for *each segment id* i *in* K **do**

    `// get curve distance of three adjacent segments points`

    $s_{i-1} \leftarrow \mathcal{S}_{\kappa,i-1}[x]$

    $s_i \leftarrow \mathcal{S}_{\kappa,i}[x]$

    $s_{i+1} \leftarrow \mathcal{S}_{\kappa,i+1}[x]$

    if $(s_i > s_{i-1}$ *and* $s_i > s_{i+1})$ *or* $(s_i < s_{i-1}$ *and* $s_i < s_{i+1})$ **then**

      `// delete current segment id` i

      $\mathcal{S}_{\kappa,i} \leftarrow$ `empty`

      $\mathfrak{F} \leftarrow$ `False`

      break

return $\mathcal{S}_\kappa$

6.4.3 *Runge-Kutta Integration*

After the automatic line segmentation for both the curvature and torsion, it's able to obtain the fitted curvature and torsion at each curve length from the previous step. As denoted by Equation 6.18, the curvature parameters are $\alpha_{\kappa,i}$ and $\beta_{\kappa,i}$, while the torsion parameters are $\alpha_{\tau,i}$ and $\beta_{\tau,i}$, $i = 1, 2, \cdots, K$. The reconstruction of a 3D curve from above curvature and torsion can be done through integration of Tangent/Normal/Binormal Unit Vectors (TNB) frame as in Equation 6.10. According to [75], we can get the piece-wise integration using 4th order Runge-Kutta methods in order to improve accuracy,

$$\begin{aligned}
\mathbf{T}_{i+1} &= \left[1 + \frac{\kappa_i^2 \Delta s^2}{2} + \frac{(\kappa_i^4 + \kappa_i^2 \tau_i^2)\Delta s^4}{4}\right] \mathbf{T}_i + \left[\kappa_i \Delta s - \frac{(\kappa_i^3 - \kappa_i \tau_i^2)\Delta s^3}{6}\right] \mathbf{N}_i \\
&\quad + \left[\frac{\kappa_i \tau_i \Delta s^2}{2} - \frac{(\kappa_i^3 \tau_i + \kappa_i \tau_i^3)\Delta s^4}{24}\right] \mathbf{B}_i \\
\mathbf{N}_{i+1} &= \left[-\kappa_i \Delta s + \frac{(\kappa_i \tau_i^2 + \kappa_i^3)\Delta s^3}{6}\right] \mathbf{T}_i + \left[1 - \frac{(\kappa_i^2 + \tau_i^2)\Delta s^2}{2} + \frac{(\kappa_i^2 + \tau_i^2)^2 \Delta s^4}{24}\right] \mathbf{N}_i \\
&\quad + \left[\tau_i \Delta s - \frac{(\kappa_i^2 \tau_i + \tau_i^3)\Delta s^3}{6}\right] \mathbf{B}_i \\
\mathbf{B}_{i+1} &= \left[\frac{\kappa_i \tau_i \Delta s^2}{2} - \frac{(\kappa_i \tau_i^3 + \kappa_i^3 \tau_i)\Delta s^4}{24}\right] \mathbf{T}_i + \left[-\tau \Delta s + \frac{(\kappa_i^2 \tau_i + \tau_i^3)\Delta s^3}{6}\right] \mathbf{N}_i \\
&\quad + \left[1 - \frac{\tau_i^2 \Delta s^2}{2} - \frac{(\kappa_i^2 \tau_i^2 + \tau_i^4)\Delta s^4}{24}\right] \mathbf{B}_i
\end{aligned} \tag{6.19}$$

Then we are able to perform a Runge-Kutta integration as algorithm 5. According to Equation 6.10, the approximation of the integrated curve point can be achieved by the trapezoidal rule as follows,

$$\mathcal{P}_{i+1} = \mathcal{P}_i + \frac{\Delta s}{2} (\mathbf{T}_{i+1} + \mathbf{T}_i) \tag{6.20}$$

where we define the initial point by $\mathbf{p}_0 = \mathbf{c}_0$ from the original ordered discrete points set.

6.4.4 *Optimal Rotation & Translation*

In the previous section, we have obtained an integrated TNB frame and coordinates using the Runge-Kutta method. However, it is highly dependent on the initial TNB vectors (i. e., $\mathbf{T}_0, \mathbf{N}_0, \mathbf{B}_0$). Thus, its accuracy may be affected by noisy initialization. Meanwhile, the existence of corners at the connection points of piece-wise segments for integration may be presented. In order to improve the global reconstruction performance, we can perform an optimal rigid transformation according to shape matching theory [8].

Algorithm 5: Runge-Kutta integration for curve reconstruction

Input : Refined curvature and torsion segments point list without overshooting $\mathcal{S}_\kappa = \{(\mathbf{s}_{\kappa,1}, \kappa_1), (\mathbf{s}_{\kappa,2}, \kappa_2), \cdots (\mathbf{s}_{\kappa,M}, \kappa_M)\}$, $\mathcal{S}_\tau = \{(\mathbf{s}_{\tau,1}, \tau_1), (\mathbf{s}_{\tau,2}, \tau_2), \cdots (\mathbf{s}_{\tau,N}, \tau_N)\}$, initial curve point $\mathbf{p}_0$, initial TNB frame $\mathbf{T}_0, \mathbf{N}_0, \mathbf{B}_0$

Output: Runge-Kutta integration of TNB frame $\mathbf{T}, \mathbf{N}, \mathbf{B}$, and the integrated curve point list $\mathcal{P}$

1 **for** *each curve length* **do**

  // get the j^{th} curve length

2 $\mathbf{s}_j \leftarrow j \cdot \Delta s$

  // find the corresponding curvature segment point pairs

3 $(\mathbf{s}_{\kappa,A}, \kappa_A), (\mathbf{s}_{\kappa,A+1}, \kappa_{A+1}) \leftarrow \mathcal{S}_\kappa$

  // calculate the corresponding fitted curvature

4 $\kappa_j \leftarrow \frac{\kappa_{A+1} - \kappa_A}{\mathbf{s}_{\kappa,A} - \mathbf{s}_{\kappa,A+1}} \cdot (\mathbf{s}_j - \mathbf{s}_{\kappa,A}) + \kappa_A$

  // find the corresponding torsion segment point pairs

5 $(\mathbf{s}_{\tau,B}, \tau_A), (\mathbf{s}_{\tau,B+1}, \tau_{B+1}) \leftarrow \mathcal{S}_\tau$

  // calculate the corresponding fitted torsion

6 $\tau_j \leftarrow \frac{\tau_{B+1} - \tau_B}{\mathbf{s}_{\tau,B} - \mathbf{s}_{\tau,B+1}} \cdot (\mathbf{s}_j - \mathbf{s}_{\tau,B}) + \tau_B$

7

  // get the Runge-Kutta integration of TNB frame coordinates using Equation 6.19

8 $\mathbf{T}_j, \mathbf{N}_j, \mathbf{B}_j \leftarrow \kappa_j, \tau_j, \Delta s, \mathbf{T}_{j-1}, \mathbf{N}_{j-1}, \mathbf{B}_{j-1}$

  // get the integrated curve point coordinates using Equation 6.20

9 $\mathcal{P}_j \leftarrow \Delta s, \mathcal{P}_{j-1}, \mathbf{T}_j, \mathbf{T}_{j-1}$

10 **return** $\mathbf{T}, \mathbf{N}, \mathbf{B}, \mathcal{P}$

Assuming to have the two curves defined as set of points in $\mathbb{R}^3$: $\mathcal{C} = \{\mathbf{c}_1, \mathbf{c}_2, \cdots, \mathbf{c}_t\}$ representing the ordered discrete points from multi-view reconstruction (as in Section 6.3.3), and $\mathcal{P} = \{\mathbf{p}_1, \mathbf{p}_2, \cdots, \mathbf{p}_t\}$ representing the curve points from the shape modeling using 3D piecewise Clothoid in algorithm 5, it is possible to find and optimal rotation matrix $\mathbf{R}$ and the translation vector $[\mathbf{t}, \mathbf{t}_0]$ to register the two curves. This is a least-square optimization problem and can be defined as:

$$(\mathbf{R}, \mathbf{t}) = \arg\min_{\mathbf{R},\mathbf{t}} \sum_{i=1}^{t} \|\mathbf{R} \cdot (\mathbf{p}_i - \mathbf{t}_0) + \mathbf{t} - \mathbf{c}_i\|_2^2 \tag{6.21}$$

It can be solved using Singular Value Decomposition (SVD) or polar decomposition methods as detailed in [8, 84].

6.5 RESULTS AND ANALYSIS

Here, we demonstrate the accuracy in reconstructing frames, including the accuracy of stereo reconstruction and the accuracy of fitting the reconstructed points by Piece-wise Clothoid (PCD) curves. For this validation, we chose the dataset where stimulation was applied to the third section of a tendril (Figure 6.1.D). We selected three instances to represent of a particular tendril's morphing phase: the beginning (at 1^{st} frame), half response (at 100^{th} frame), and final shape response (at 200^{th} frame) after the stimulation.

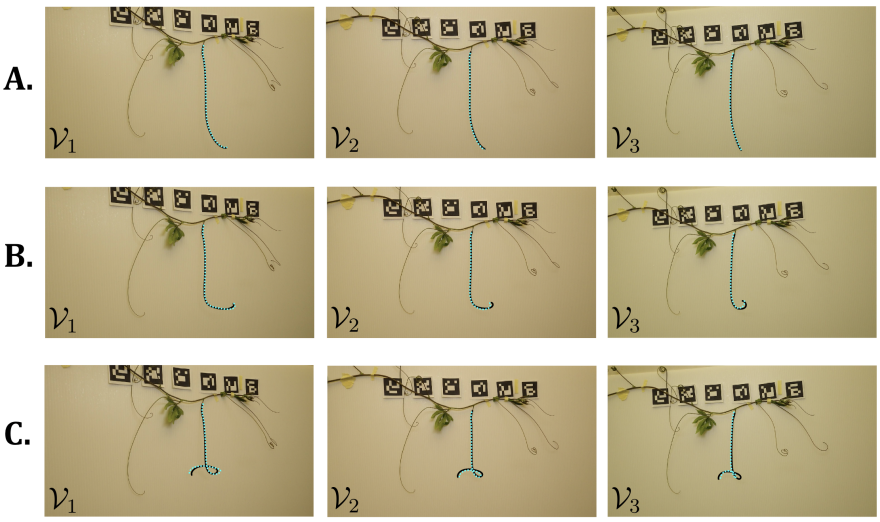


Figure 6.6: The shape comparison of extracted tendril skeletons (highlighted in black) and the stereo reconstructed projections (highlighted in cyan) in corresponding views, $\mathcal{V}_1$, $\mathcal{V}_2$ and $\mathcal{V}_3$. **A**, **B** and **C** are the results of the 1^{st} frame, the 100^{th} frame and the 200^{th} frame, shown by row.

6.5.1 *Accuracy of Stereo Reconstruction*

To verify the accuracy of our stereo reconstruction method, we projected the reconstructed 3D tendrils points onto the image plane for each perspective (i. e., $\mathcal{V}_1$, $\mathcal{V}_2$ and $\mathcal{V}_3$) and compared them with the extracted 2D skeletons. The visual comparison of Figure 6.6 demonstrates a good match between the re-projections (highlighted in cyan) in the three morphing phases and the extracted skeleton (highlighted in black) in each view. The process of reconstruction relies on bundle adjustment, which involves comparing pairs of images. Specifically, we compare the pairs ($\mathcal{V}_1$, $\mathcal{V}_2$) and ($\mathcal{V}_3$, $\mathcal{V}_2$) in our case. Overall, the reprojection accuracy in $\mathcal{V}_1$ and $\mathcal{V}_2$ exhibits slightly better than in $\mathcal{V}_3$. This is because the bundle adjustment optimization process involves using $\mathcal{V}_2$ as a common feature in each pair of images being compared.

Due to its closer proximity to $\mathcal{V}_2$, the view of $\mathcal{V}_1$ provides superior results compared to that of $\mathcal{V}_3$. Conversely, $\mathcal{V}_3$ perspective also contributes to shape optimization of the 3D reconstructed model with respect to the depth estimation.

We also conducted a numerical comparison of the image-pixel differences between the extracted skeleton points and the projections of the reconstructed tendril points onto three image planes. The compared disparity was determined by calculating the Mean Error (ME) and Standard Deviation (SD) in three sections: the entire shape, base section and tip section. The ME values for each section were calculated by taking the absolute difference between the skeletonized points and the projection of reconstructed points, and averaging over all the points in the section. The SD values were calculated as the standard deviation of the differences between the reconstructed tendril's projection and the extracted tendril points in each section. The length of the base section and tip section was assigned to be one-quarter of the whole length of the tendril, measured separately from its base and tip. The whole image size is 1920×1080 pixels.

Table 6.1 demonstrates that the mean error for the base section is the lowest among other sections, indicating a higher reconstruction accuracy in this section. The tip section has slightly higher ME values, indicating a slightly lower accuracy in sections. The ME value for the total length of the tendril is higher than that for the base section but still within an acceptable range, which is less than 23 pixels and quite small compared to the overall size of 2.0736×10^6 pixels.

The SD values for all sections are relatively small, indicating that the reconstructed curves are consistent and reliable. The SD for the base section is the lowest, indicating a higher degree of accuracy and consistency in this section. The SD for the tip section is slightly higher than that for the other sections, which is due to the greater variability of the tendril shape in this region. The difference in the SD of the entire shape reconstruction is also small, less than 14 pixels.

Furthermore, both errors become more significant as the tendril shape evolves from the initial morphology (1^{st} frame) to the final shape (200^{th} frame). This is since our method adopted the first frame for tendril shape initialization, and all subsequent frames were based on this initialization.

Overall, the reconstruction accuracy of the base segment is higher than that of the tip segment, and our reconstruction accuracy is considerable.

6.5.2 *Accuracy of Clothoid Fitting*

Next, we also used the re-projection approach and compared the projections onto the correspondent views to validate the accuracy of reconstructed points fitted by the piece-wise clothoid curves method.

Frame		ME (pixel)			SD (pixel)		
	Views	Entire	Base Seg	Tip Seg	Entire	Base Seg	Tip Seg
1	$\mathcal{V}_1$	3.4951	2.9020	3.0643	0.8043	0.4448	0.4390
	$\mathcal{V}_2$	4.9690	3.7757	9.5178	2.9742	0.6733	1.0568
	$\mathcal{V}_3$	8.0666	6.8500	7.0944	1.9148	1.3554	1.9023
100	$\mathcal{V}_1$	7.9629	3.2556	15.0116	4.8738	0.6560	3.3446
	$\mathcal{V}_2$	8.6539	6.8103	16.3470	5.2214	2.0423	2.8152
	$\mathcal{V}_3$	17.628	9.1724	22.2579	7.0410	1.3888	6.7207
200	$\mathcal{V}_1$	13.001	5.7096	7.10485	8.6477	2.0893	5.8880
	$\mathcal{V}_2$	10.935	6.1356	10.3278	5.6904	2.5911	1.5974
	$\mathcal{V}_3$	22.454	13.125	10.4357	13.0686	3.2229	6.2604

Table 6.1: A comparison of average and standard errors in image pixel between skeleton points and projections of reconstructed tendril points onto three image planes. The results are relative to the tendril's three morphing phases at the 1^{st}, 100^{th}, and 200^{th} frame.

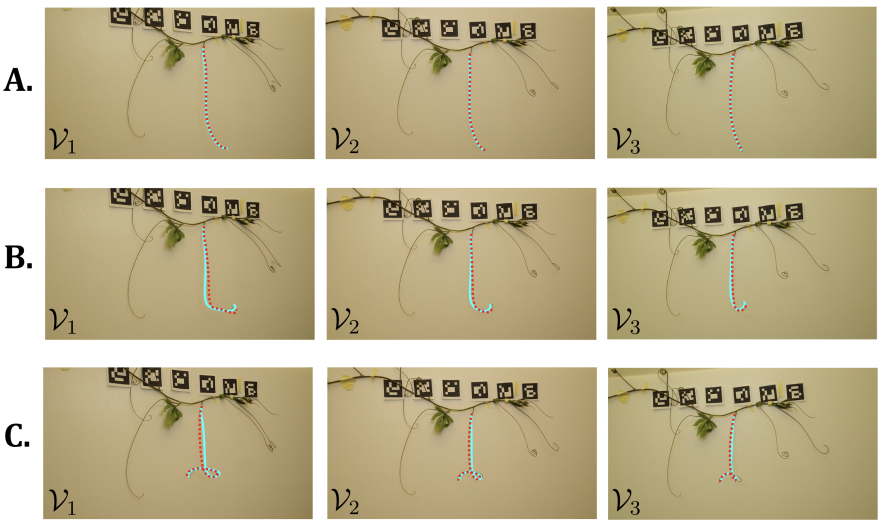


Figure 6.7: The shape comparison of the stereo reconstruction projections (highlighted in cyan) and the Piece-wise Clothoid (PCD) fitted projections (highlighted in red) in corresponding views, $\mathcal{V}_1$, $\mathcal{V}_2$ and $\mathcal{V}_3$. **A**, **B** and **C** are the results of the 1^{st} frame, the 100^{th} frame and the 200^{th} frame, shown by row.

This involved comparing the projections of the fitted curves obtained using the piece-wise clothoid method (highlighted in red) and the original reconstructed tendril points (highlighted in cyan). Figure 6.7 illustrates that the stereo reconstruction projections and the piece-wise clothoid fitted projections have a good fitting results for the whole shape in each corresponding view. Intuitively, the fitting results in middle sections have a certain deviation.

To quantify the accuracy of the PCD curve fitting model, we also performed a numerical comparison of the image-pixel differences between the projections of the PCD curve fitting model and the original reconstructed tendril points. Table 6.2 also shows the Mean Error (ME) and Standard Deviation (SD) comparison of three representative tendril sections, i. e., the base, tip, and entire segment. The results show that the change trend of both error values is similar to that of the reconstruction results in the Section 6.5.1. That is because our fitting method is based on the reconstruction results. Therefore, both errors overall become more significant as the tendril's morphological evolution from the initial shape (1^{st} frame) to the final shape (200^{th} frame). Furthermore, an analysis comparison of ME values in the entire shape and the base/tip segments indicates that the fitting results in middle sections deviate significantly from other parts. The continuity of curvature and torsion is required by the piecewise property of clothoid curves, which is the main reason for this. The SD values for all sections are relatively small (less than 10 pixels), indicating that our clothoid fitting curves are reliable. To sum up, the results of our analysis suggest that the piece-wise clothoid curve fitting model is an effective method for accurately describing the shape of tendrils.

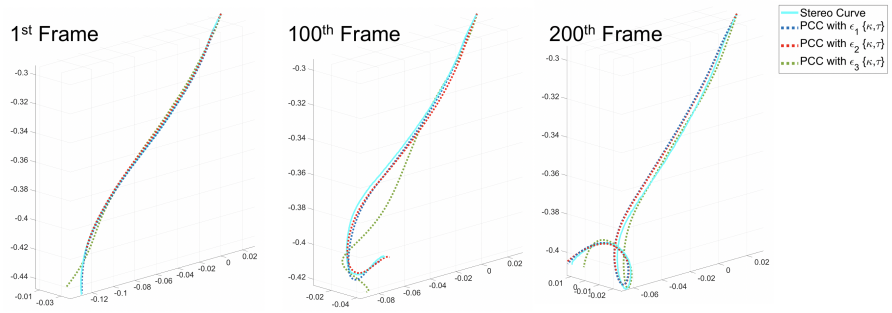


Figure 6.8: The selected frames after reconstruction and piecewise Clothoid curve fitting under different penalties in curvature and torsion.

6.5.3 *Sensitivity of Fitting Parameters*

The goodness of piecewise fitting results lies in how to determine the appropriate number of segments to achieve the optimal fitting. We evaluated the results by setting different, arbitrary chosen penalties in the optimization problem in Equation 6.16. The proposed algorithm generates a different number of piecewise clothoid segments depending on the penalties. We can observe that values of penalties ($\epsilon_{i\{\boldsymbol{\kappa}\}}$ and $\epsilon_{i\{\boldsymbol{\tau}\}}$, where $i = 1, 2, 3$) highly affect the reconstruction, especially at the 100^{th} frame, where the deformation is at half of the process, visualized in Figure 6.8. It is quite reasonable since during this stage, the tendril undergoes changes in both curvature and torsion significantly.

Frame		ME (pixel)			SD (pixel)		
	Views	Entire	Base Seg	Tip Seg	Entire	Base Seg	Tip Seg
1	$\mathcal{V}_1$	6.2466	3.7479	4.8391	2.7127	1.6500	1.5890
	$\mathcal{V}_2$	5.3262	2.4242	6.3898	2.0181	1.0712	0.9608
	$\mathcal{V}_3$	4.1638	2.1449	5.0599	1.4418	0.8736	1.5731
100	$\mathcal{V}_1$	15.3940	15.1840	10.3420	5.2313	5.9630	2.5095
	$\mathcal{V}_2$	9.4546	8.1449	7.2112	3.1676	3.5505	2.1564
	$\mathcal{V}_3$	6.1265	4.4073	4.5838	2.3424	2.1925	1.2073
200	$\mathcal{V}_1$	16.2491	15.2359	13.5972	7.4025	9.2382	1.3979
	$\mathcal{V}_2$	10.5715	8.7959	9.4189	4.3685	5.5375	0.9723
	$\mathcal{V}_3$	7.9385	5.5857	5.4172	3.6088	3.7365	1.5812

Table 6.2: A comparison of average and standard errors in image pixel between projections of reconstructed tendril points and piece-wise clothoid fitted points onto the three image planes. The results are relative to the tendril's three morphing phases at the 1^{st}, 100^{th}, and 200^{th} frame.

Tables hile, the corresponding numerical comparison is shown in Table 6.3. To facilitate comparison, the number of segments required for approximation, the coefficient of determination (R^2) for Piecewise Clothoid Fitting, the Sum of Squares Error (SSE), and the Sum of Squares Total (SST) are reported for each pair of parameters $\epsilon_{i\{\kappa\}}$ and $\epsilon_{i\{\tau\}}$. The errors in the table for comparing different parameters selection also involved three regions, the tip segment, the base segment and the entire length.

Generally, all cases produce an R^2 value larger than 0.9. Although the Sum of Squares Total (SST) is similar across the different sets of parameters, the Sum of Squares Error (SSE) shows variable results. Therefore, we can automatically select the penalties to get the optimal number of segments and reach an optimal fit for each frame. To this aim, we rely on a grid search policy by minimizing SSE and R^2 within a pre-defined range of penalty values. The search process is illustrated in Figure 6.9, which depicts the penalty selection for the 100^{th} frame as an example. We performed a grid search within a broad range, then selected several interest regions (for example, the regions within grey dashed lines in Figure 6.9) and repeated the grid search until we found the appropriate penalties determined by the error fitting of SSE and R^2.

6.5.4 *Reconstruction From a Sequence of Frames*

The above results were evaluated from a single frame. It is possible to extract the evolution of the curvature and torsion over time by

Frame	Penalty			Segments		R^2			SSE			SST3		
	i	$\epsilon_{i\{\kappa\}}$	$\epsilon_{i\{\tau\}}$	κ	τ	Entire	Base Seg	Tip Seg	Entire	Base Seg	Tip Seg	Entire	Base Seg	Tip Seg
1	1	100	100	6	136	0.9995	0.9977	0.9917	0.0014	0.0085	0.0006	2.7572	0.0373	0.0778
	2	200	300	3	56	0.9993	0.9989	0.9989	0.0018	0.0040	0.0006	2.7532	0.0373	0.0779
	3	500	500	3	49	0.9717	0.6589	0.7749	0.0788	0.0127	0.018	2.7859	0.0373	0.0782
100	1	100	100	13	117	0.9963	0.9967	0.8540	0.0078	0.0001	0.0030	2.1123	0.0326	0.0206
	2	500	900	7	30	0.9983	0.9854	0.9645	0.0034	0.0005	0.0007	2.0243	0.0325	0.0210
	3	600	1500	7	3	0.9699	0.9652	0.1882	0.0660	0.0011	0.0254	2.1889	0.0325	0.0214
200	1	100	100	18	112	0.9973	0.9826	0.9762	0.0045	0.0007	0.0005	1.6781	0.0406	0.0231
	2	100	200	18	77	0.9977	0.9865	0.9801	0.0038	0.0005	0.0005	1.6782	0.0406	0.0231
	3	800	450	9	41	0.9850	0.9246	0.7727	0.0253	0.0031	0.0052	1.6851	0.0406	0.0229

Table 6.3: A summary of the results for the Clothoid model fitting as a function of the penalty parameters. The results are relative to the tendril stimulated at **S3** and for the 1^{st}, 100^{th}, and 200^{th} frame. To easily compare the results, for every pair of parameters $\epsilon_{i\{\kappa\}}$ and $\epsilon_{i\{\tau\}}$, the number of segments needed for the approximation, the coefficient of determination (R^2) for Piece-wise Clothoid Fitting, the Sum of Squares Error (SSE), and the Sum of Squares Total (SST) are reported.

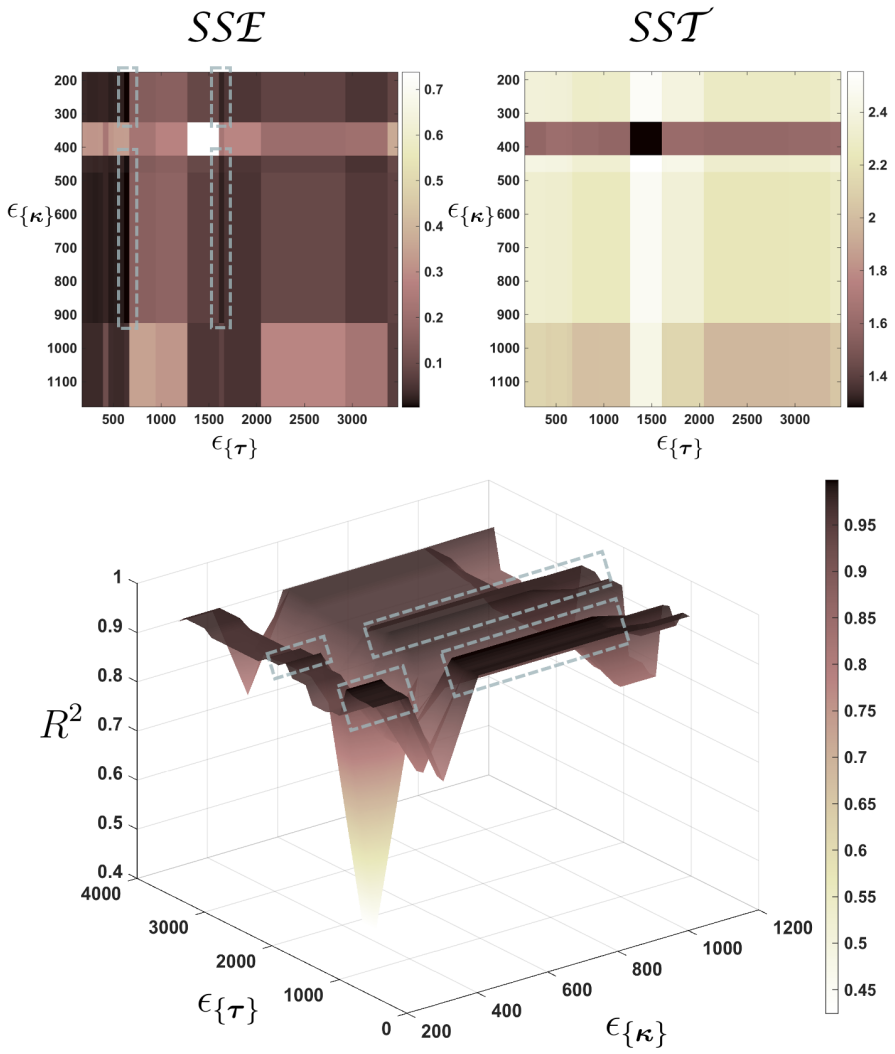


Figure 6.9: The fitting error of selected 100^{th} frame after piecewise clothoid curve fitting with different penalties in curvature and torsion.

looking at the entire sequence of frames (15 min of recorded video give approximately 21,500 frames). To compare the effects of the applied stimuli, here we consider all the four cases **S1**, **S2**, **S3**, **S4**, as introduced in Figure 6.1D.

By fixing the number of points in the reconstructed curve and the penalty cost $\epsilon_{i\{\kappa\}}$ and $\epsilon_{i\{\tau\}}$, we can visualize the morphological evolution of the tendril over time and the region of highest deformation. Figure 6.10 shows the results of selected dataset for each case. All the curves have been reconstructed using 200 points and considering the temporal evolution over a subset of the videos sampling the data every 120 s for a total of 200 frames. The highlighted pixels represent the pixel index of the split segment. From the results it is possible to notice that the number of piece-wise segments is generally the same for all frames, and that the index locations stabilize after a while (e.g., Figure 6.10A, segment **S2**, from frame 80). In addition, it is possible to

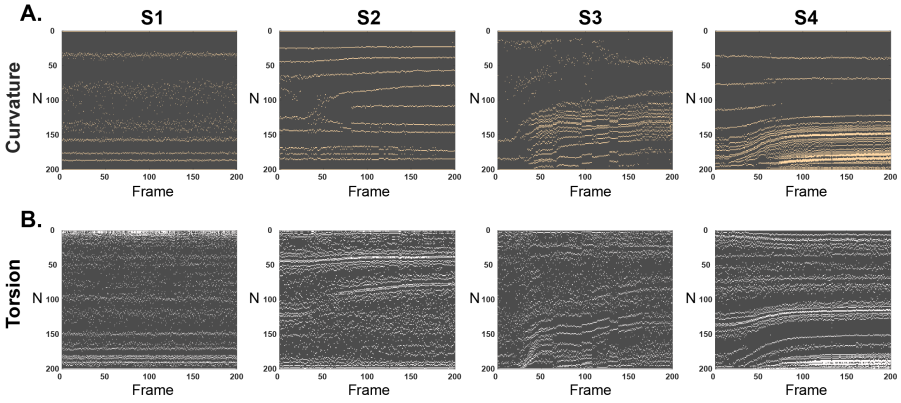


Figure 6.10: Location of the splitting point between segments in the linear fitting of **A** the curvature and **B** the torsion. For each case, we reconstruct the curve using 200 points over a subset of the entire video which was sampled every 120 *s*, thus reducing the amount of frames to 200.

notice that the indices are denser around the location between point 150^{th} to 200^{th}, this is more visible for the cases **S3** and **S4**, which are in the apical region of the tendril. The number of segments in torsion plots (Figure 6.10B) is even higher. Thus, we can tell that the torsion has a more nonlinear behavior along the entire tendrils' length. From a mechanics point of view, the reconstructed curve shows non-constant twisting in space due to an additional out-of-plane torque. This pattern fits the requirements of the plant tendrils to find support object to grow against gravity.

Figure 6.11 shows the evolution of the tendril motion fitted by the proposed algorithm. The initial and final frames were highlighted in black and red curves respectively, while the dynamical motions in colored curves. In all cases, the tendrils show a high response to the stimulus and, at the exception of a stimulus in S1 region (Figure 6.11A), show large deformations. This is also noticeable by looking at the curvature and torsion evolution over time (second and third rows in the figure). Here it is possible to see that for **S1** and **S2** there is a large change in curvature in the apical area and a stimulus in the S2 region (Figure 6.11B) produces a large, moving change in torsion. Also, a stimulus in the S3 region produces a clear change in curvature that moves from the tip backwards (Figure 6.11C from 3 *min* it is possible to notice a sharp change in the curvature). A similar behavior is present in the results relative to the stimulus in S4 region. Differently from the previous results, the change in curvature is well localized in the same region of the stimulus, while the change in torsion happens in multiple points of the tendril.

To further confirm the movement trend of the morphological evolution of the studied tendrils as a consequence of the applied stimulus, we averaged curvature and torsion values at initial and final states

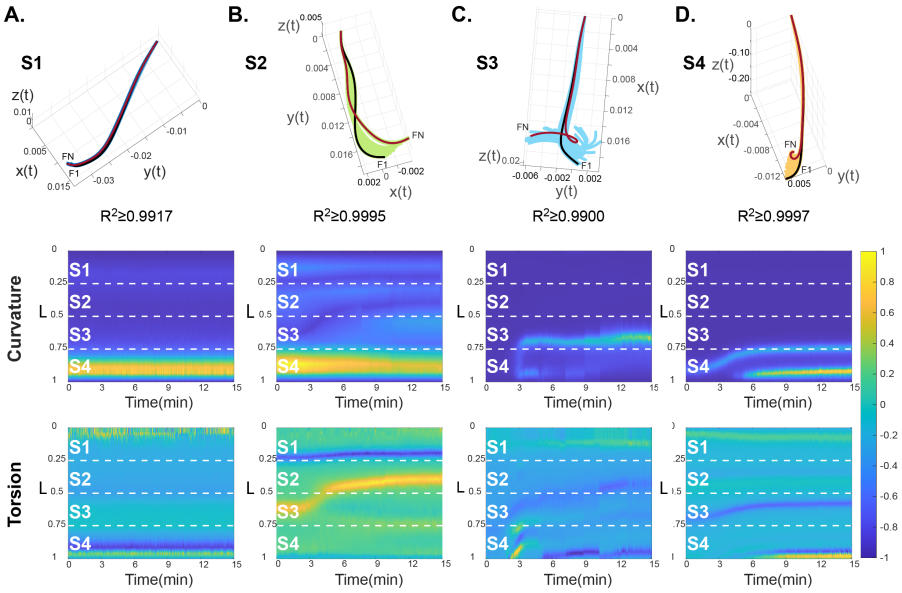


Figure 6.11: The comparison of morphology evolution of the four representative tendrils after stimulation in four different regions with the correspondent variation of curvature and torsion. The first row shows the morphology evolution of tendrils after the stimulation in S1, S2, S3 and S4 region (from left to right) applied individually for each case. The initial frame and the final frame are highlighted in black and in red respectively. The middle row demonstrates the correspondent color changes in normalized curvature along the normalized curve length and the last row shows the changes in normalized torsion.

over all the repetitions for each experimental group. Figure 6.12 summarizes the results. We found that after the stimulus is applied to any part of the tendril, it triggers a sequence of movements in the tendril which brings a change in its morphology. This reveals that the sensitivity of tendrils is endowed with local transduction at site of stimulation whose effect is propagated to adjacent regions.

6.5.5 *Analysis of Tip Motions*

A final analysis possible thanks to the proposed modeling algorithm is related to the motion of the most apical point of the tendril after the application of a stimulus (Figure 6.13). When it occurred in the S1 region (Figure 6.13A), the tip showed a stable movement around to a central point. The movement changes when the stimulus is applied to the S2 region (Figure 6.13B) passing from a static motion to a quasi-linear movement in the space. For the last two cases, stimulus in region S3 and S4, the tip of the tendril moves following a curvilinear pattern spanning in a large volume. The different tip movement patterns support our previous results: regions of the tendrils closer to the base result less active with respect to regions proximal to the tip.

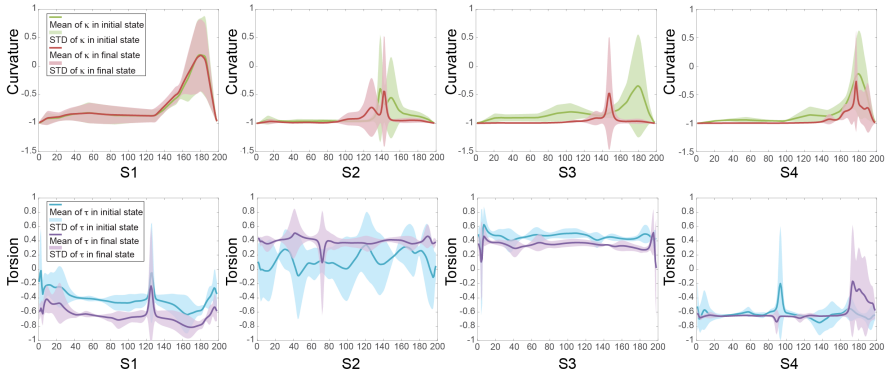


Figure 6.12: The comparison of curvature and torsion between the initial state and the final state, in addition to the change trends.

6.6 SUMMARY

In this chapter, we present a new methodology to reconstruct and analyse tendril curling shape and movement in space, based on stereo vision reconstruction and 3D piece-wise clothoid for shape analysis, with no need for marker-based features. We used this approach to describe different 3D morphologies assumed by natural tendrils triggered by mechanical stimulation and analyze their shape evolution over time. This work provides a reliable (high accuracy, $R^2 \geq 0.99$) approach to reconstruct and model filamentous continuum structures. It demonstrates its applicability to the morphological description of tendrils of *passiflora* and contributed to the analysis of stimulus-response relationship in this model organ of climbing plant, helping identifying region of high responsiveness which might be related with higher sensitivity.

From our results we can infer information regarding the stiffness of these organs and draw specifications for the design of slender, continuum, curling robots targeting anchoring or grasping through coiling deformations. For example, we can suggest a variable stiffness distribution of the structure going from stiffer to softer from base to tip, and greater sensitivity to be displaced at the tip. The proposed method is implemented based on post-stimulus reconstruction and static model representation of curling behavior in spacial dimensions. Thus, neglecting possible dynamics that might act during deformation. This is a crucial aspect when shifting this analysis to elaborate on control strategies for soft robots. The integration of our model with force-based dynamics models, such as the Cosserat rod theory, and the fully automatic image segmentation for data pre-processing, remain for future work. In addition, as a analysis tool of plant behavior, fully automatic segmentation of interest organs and additional experimental validation inferred by our approach could be discussed as the future work.

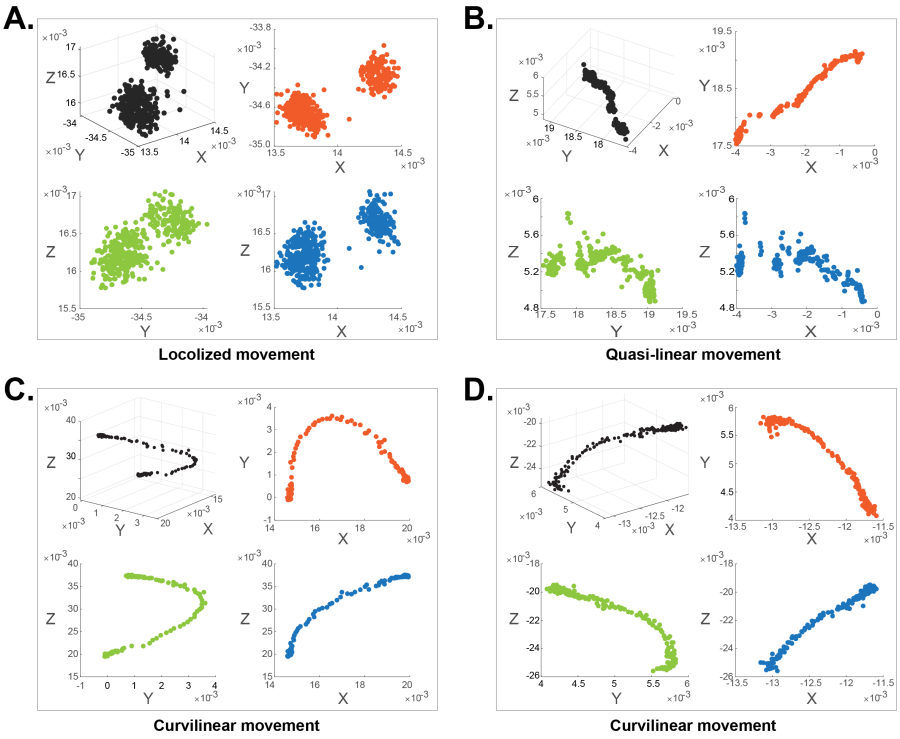


Figure 6.13: 3D tip movement of tendrils in black and the correspondent projections of trajectories to X-Y, Y-Z, X-Z planar, respectively colored in orange, green and blue.

7

CONCLUSIONS & FUTURE DIRECTIONS

Curling behavior, as the most common geometry of continuum elements, is able to produce various curling or coiling morphologies. Such shape configurations are most curling up from the tip and bending along the arc length, producing a continuously curved shape. While it is of great importance to building methods of shape analysis for these kind of biological thin systems to facilitate the translation of functional principles into artificial systems, such as soft robots.

However, the modeling and reconstruction of curling shapes are still challenging in the biological and robotics fields, especially for thin structures. More importantly, the lack of an analytical method for shaping morphology analysis is a significant constraint in characterizing and enhancing the controllability of robotic systems, such as soft continuum robots.

The main focus of this thesis is to present a novel shape modeling and reconstruction approach that also provides a feasible solution to morphological analysis of continuum, curling structures, from both an engineering and biological perspective. This problem is mathematically complex due to the slender, continuous shape of the "almost" 1D-object (a curve) that is embedded in a plane (2D images) but requires analysis in a 3D environment (motion space).

7.1 CONTRIBUTIONS OF THIS WORK

Taking the evolution of *passiflora* tendrils' morphology upon mechano-stimuli as an example, this thesis proposes novel methodologies to reconstruct and analyze tendrils' curling morphologies and movement both in 2D and 3D cases. As mentioned in Chapter 1, *passiflora* tendril is irritated by mechanical stimulation, we thus addressed the issue of analyzing its shape changes employing a marker-less technology of shape sensing based on vision and curve model fitting. This work provides a promising tool from biological and engineering perspectives for shape representation of tendril-like thin, continuum structures, which prompted us to mainly investigate the following three questions:

- **Q1**: How to choose a curve model for accurate shape representation?
- **Q2**: For the vision-based shape reconstruction method, how to process data in 2D and 3D respectively?
- **Q3**: How to characterize the morphological dynamics over time?

The first question pertains to **shape modeling** and suggests that choosing an appropriate curve model. The second question concerns **shape reconstruction** using vision-based methods and inquires about the difference between processing 2D and 3D data. Lastly, the third question relates to **motion analysis** over time. These three questions are all related to the field of computer vision and image processing and address important considerations for accurately representing and analyzing shapes and motions, in particular for thin continuum structures.

7.2 ANSWERS OF PROPOSED QUESTIONS

We first conducted a survey concerning the shape reconstruction technique (Chapter 2), such as model-based, sensor-based and vision-based approaches. These techniques can provide shape reconstruction under different situations with limitations. We thus proposed a combined 3D reconstruction approach for thin, slender objects that combines vision and modeling techniques.

We introduced the clothoid curve to describe the curling continuum shapes since the natural tendril has analogy characteristics – i. e., smooth transition between one straight line and one curve or between multiple curve segments.

To describe 2D curling shapes, we proposed three model-based approaches using: I) single-segment clothoid, II) piece-wise clothoid with a prescribed number of segments (in Chapter 4) III) piece-wise clothoid model with the optimal number of segments (in Chapter 5). And to describe 3D curling shape, we based on the 2D work and used 3D piecewise clothoid curve for the shape representation (in Chapter 6).

As suggested from the presented results, the curling shape is reliably described by clothoid curve fitting both in 2D and 3D cases. In the 2D case, the proposed approaches have been validated on both the biological and artificial continuum structures and are numerically evaluated. We obtain an improvement of more than 100% in biological tendril and up to 5% with a soft continuum robotic artefact, demonstrating the feasibility and reliability of our approach. In addition, we find that from 4 to 6 segments are enough to describe with high accuracy ($R^2 > 0.9$) the tendril shape across different stages of curling evolution in planar cases. In the 3D case, our work also provides a reliable approach to reconstruct and model filamentous continuum structures with high accuracy ($R^2 \geq 0.99$) in spacial dimensions.

In conclusion, clothoid spiral, both in 2D and 3D, fulfills our accurate description requirements for curling shape and answers to question **Q1**.

Next, to answer **Q2**, we describe the process of data acquisition and processing in two different dimensions. In the planar, processing

a single image or an image sequence is completed by the following steps: image resizing, segmentation by thresholding, binarization for better ROI extraction and sort of unarranged skeleton points, preparing for the curve fitting. In the space, the processing is based on stereo reconstruction. The process starts with the acquisition of video data from three different perspectives via cameras. A semi-automatic segmentation method was developed using small inter-frame variation and K-NN search. Subsequently, the unordered skeleton points were extracted after binarization and skeletonization. Then, the procedure sorts the unordered skeleton points. After this, it is possible to find the correspondence between the skeleton curves in different views using the Fréchet distance. Finally, through triangulation, we project the 2D points in the 3D space to obtain the reconstructed discrete 3D curve points.

A common and important step in both processes is a novel sorting algorithm for 2D unarranged points that I developed. It addresses the issue of potentially unwanted branching and discontinuities, and misleading ordering direction in the presence of sharp curvature change by the implementation of a weight-point association. Moreover, the developed algorithm is divided according to the occurrence of intersection point as on-plane and off-plane cases (see Chapter 6).

After taking the vision and clothoid model-based shape reconstruction, we analyzed the changes over time in the morphology of natural tendrils after the mechano-stimuli, whose results concerning the changes in curvature and torsion also respond accordingly to question **Q3**.

In the 2D case, we noted that the portion close to the base of the tendril does not change curvature in time, even though previously stimulated along the body length, while the most apical region is more dynamic in curvature variation.

To further study the morphologies and stimulus-response relationship of tendrils, we set up the experiment protocol with piecewise stimuli in four segments to explore the dynamic characteristics of morphological motion over time in the 3D space while considering the variation in both curvature and torsion. Specifically, we focused on the relationship between the shape change and the trigger location. We found that after the stimulus is applied to any part of the tendril, it triggers a sequence of movements in the tendril which brings a change in its morphology. This reveals that the sensitivity of tendrils is endowed with local transduction at the site of stimulation, whose effect is propagated to adjacent regions. In addition, stimuli applied at different sites cause the tendril tip to follow different spatial trajectories, such as a stable movement around a central point when stimuli are applied in the base of a tendril, and stimuli in the apical area, the tip of the tendril moves following a curvilinear pattern spanning in a large volume. Such different tip movement patterns support our

previous results in the 2D case: regions of the tendrils closer to the base result less active with respect to regions proximal to the tip. From the location where the linear fitting algorithm splits the curve in the curvature and torsion graphs, we also found that the indices of segmented location are denser around the tip of the tendril, that is, the apical region is the region of highest deformation due to the stimuli-responsive in situ. Moreover, the torsion has a more nonlinear behavior along the entire tendrils' length than the curvature. This conclusion corroborates that the stimulated tendril shows non-constant twisting in space due to an additional off-plane torque.

7.3 LIMITATIONS & FUTURE DIRECTIONS

This research provides favorable results, but still several aspects can be improved to achieve better results in future works. The following aspects could be expanded upon:

Automatic Image Segmentation: The tendril segmentation step in Chapter 6 is semi-automatic, and it could be improved as a fully-automated operation of image segmentation using pre-built foreground and background models. In addition, our data considers a simplified growing environment – a white board as the background. The real environment should be much complex, whose scenarios possible with poorer shape visibility of ROI, or with overlapping parts. These works would be favorable as a tool for analyzing plant growth and behavior in real environment.

Real-time Shape Reconstruction: Now, our methods are off-line and all the operations of shape reconstruction for each frame takes about 30s on average, except the time of video loading and data pre-processing. Considering the ultimate goal, real-time reconstruction of curling shape will be necessary for shape control in the future work. The fully automated segmentation mentioned in previous aspect could be also as one part to realize the real-time shape reconstruction.

Dynamics Factors Involvement: Next, the proposed methods are implemented based on static model representation of curling behavior. Thus, neglecting possible dynamics that might act during deformation. This is a crucial aspect when shifting the analysis to elaborate on control strategies for soft robots. The integration of our model with force-based dynamics models, such as the Cosserat rod theory, remains for the next step.

Non-Parametric Modeling Approach: Our suggested methodologies are based on the parameterized clothoid models, which are implemented through fitting curve data for local optimization, resulting in slow speed of convergence and inaccuracy of shape reconstruction. In Chapter 5, we further used a rational approximation of 2D clothoid model, which is generated by evaluating the error of polynomial approximation of the equations and point interpolation. Thus, one

aspect of future works is to employ machine learning methods with non-parametric models and shape geometry primitives for a better fit to a spatial shape of a continuum robot and to incorporate the pre-trained data to accelerate the speed of shape reconstruction and representation.

Shape Control: Based on the proposed shape models incorporating with seroving control strategy, a future application could be to use this methodology for some spacial tasks, such as shape trajectory tracking or end effector positioning. Such tasks under shape configuration are achieved by an optimization-based closed-loop method to iteratively solve the Jacobian matrix by minimizing the task space error. Further, the shape-based method could also be used for the force estimation to solve the force sensing problem in applications when the continuum element interacts with the environment, such as, a tendril-like robot climbing along a vertical support. Moreover, during the shape seroving control process, incorporating the effect of gravity may be necessary.

In addition, we would also like to explore extensions, such as full volumetric shape servoing, handling of contact or interact with the external environment. These promising works pave the way for automatic control of the 3D shapes of tendril-like growing robots targeting, bending, twisting or deforming inspired by the moving-by-growing abilities of climbing plants.

7.4 APPLIICATIONS

As a summary, I developed a reliable methodology to reconstruct and model filamentous continuum structures that can be used as a tool for the morphology analysis of tendril-like organs, such as stem growing, earthworm or nematode locomotion [119]. Moreover, the practical bio-analysis can provide the biological property for the design of bio-inspired robots with stimuli-response characteristics. For instance, we inferred information from the results regarding the stiffness and sensitivity distribution of tendrils, which can be used as specifications for the design of slender, continuum, curling robots targeting, anchoring or grasping through coiling deformations. In one specific example, a tendril-like robot with variable stiffness distribution of structure that goes from stiffer to softer, from base to tip, with increased sensitivity to displacement at the tip. It might also suggest how the required sensors are distributed along the body length in terms of quantity and position.

According to the design solution of the double symmetrical cycle for biomimetic robots (in Chapter 1), the tendril-inspired robot can be abstracted into a working platform to test hypotheses on the factors causing morphological changes and sensitivity transduction, allowing us to examine our understanding of biological systems without dealing with the whole complex system of climbing plants.

Part IV

APPENDIX

A

DERIVATION OF PARTIAL DERIVATIVES

According to Equation 3.4, Clothoid with Fresnel Integrals is defined as:

$$\begin{aligned} X_c &= \int_0^s \mathscr{F}_{cos} d\xi = s\mathbb{X}_0(k_1 s^2, k_2 s, \alpha_0) \\ Y_c &= \int_0^s \mathscr{F}_{sin} d\xi = s\mathbb{Y}_0(k_1 s^2, k_2 s, \alpha_0) \\ \mathscr{F}_{cos} &= cos(\frac{k_1}{2}s^2 + k_2 s + \alpha_0) \\ \mathscr{F}_{sin} &= sin(\frac{k_1}{2}s^2 + k_2 s + \alpha_0) \end{aligned} \tag{A.1}$$

Then, we perform the affine transformation (i.e., $\mathcal{R}, \mathcal{S}, \mathcal{T}$) to the generated the fitting curve $X_\mathcal{F}$ and $Y_\mathcal{F}$, that is,

$$\begin{aligned} X_\mathcal{C}^\mathcal{T} &= \mathcal{T} X_\mathcal{C} \\ X_\mathcal{C}^\mathcal{S} &= \mathcal{S} X_\mathcal{C}^\mathcal{T} \\ X_\mathcal{C}^\mathcal{R} &= \mathcal{R} X_\mathcal{C}^\mathcal{S} \\ X_\mathcal{F} &= \mathcal{R}\mathcal{S}\mathcal{T} X_c \end{aligned} \tag{A.2}$$

During each transform, it should be applied with respect to the same fixed point [49],

$$\begin{aligned} X_\mathcal{C}^\mathcal{T}[1] &= -X_\mathcal{C}[1] + X_\mathcal{I}[1] \\ Y_\mathcal{C}^\mathcal{T}[1] &= -Y_\mathcal{C}[1] + Y_\mathcal{I}[1] \\ X_\mathcal{C}^\mathcal{R}[1] &= X_\mathcal{C}^\mathcal{S}[1] = X_\mathcal{C}^\mathcal{T}[1] \\ Y_\mathcal{C}^\mathcal{R}[1] &= Y_\mathcal{C}^\mathcal{S}[1] = Y_\mathcal{C}^\mathcal{T}[1] \end{aligned} \tag{A.3}$$

where $X_\mathcal{I}$ and $Y_\mathcal{I}$ represent the image skeleton points after ordering.

Here, we list the main calculation of partial derivatives for f of Equation 4.3:

$$\begin{aligned} \frac{\partial f}{\partial \Theta} &= (X_\mathcal{F} - X_\mathcal{I})\frac{\partial X_\mathcal{F}}{\partial \Theta} + (Y_\mathcal{F} - Y_\mathcal{I})\frac{\partial Y_\mathcal{F}}{\partial \Theta} \\ \Theta &= w_s, h_s, \beta, k_1, l_a, l_b \end{aligned} \tag{A.4}$$

Take the partial derivative of both sides of Equation 4.2,

$$\begin{pmatrix} \nabla_\Theta X_\mathcal{F} \\ \nabla_\Theta Y_\mathcal{F} \\ 0 \end{pmatrix} = \nabla_\Theta \left(\mathcal{R}\mathcal{S}\mathcal{T} \begin{bmatrix} X_\mathcal{C}^T \\ Y_\mathcal{C}^T \\ 1 \end{bmatrix} \right) \tag{A.5}$$

where the correspondent relationship in parameters (Θ) are the followings: width scale (w_s) and height scale (h_s) are related to curve

scale $\mathcal{S}$, angle (β) is related curve rotation $\mathcal{R}$, the parameters of curvature (k_1), start length (l_a), end length (l_b) are related to the fitted curve.

In details, calculation of partial derivatives for the scale and rotation:

$$\begin{pmatrix} \nabla_{w_s} X_{\mathcal{F}} \\ \nabla_{w_s} Y_{\mathcal{F}} \\ 0 \end{pmatrix} = \mathcal{R}\ \nabla_{w_s}\mathcal{S}\ \mathcal{T} \begin{bmatrix} X_{\mathcal{C}}^T \\ Y_{\mathcal{C}}^T \\ 1 \end{bmatrix} \tag{A.6}$$

$$\begin{pmatrix} \nabla_{h_s} X_{\mathcal{F}} \\ \nabla_{h_s} Y_{\mathcal{F}} \\ 0 \end{pmatrix} = \mathcal{R}\ \nabla_{h_s}\mathcal{S}\ \mathcal{T} \begin{bmatrix} X_{\mathcal{C}}^T \\ Y_{\mathcal{C}}^T \\ 1 \end{bmatrix} \tag{A.7}$$

$$\begin{pmatrix} \nabla_{\beta} X_{\mathcal{F}} \\ \nabla_{\beta} Y_{\mathcal{F}} \\ 0 \end{pmatrix} = \nabla_{\beta}\mathcal{R}\ \mathcal{S}\mathcal{T} \begin{bmatrix} X_{\mathcal{C}}^T \\ Y_{\mathcal{C}}^T \\ 1 \end{bmatrix} \tag{A.8}$$

Subsequently, calculation of partial derivatives for the parameters of fitted curve:

$$\begin{pmatrix} \nabla_{\Theta_1} X_{\mathcal{F}} \\ \nabla_{\Theta_1} Y_{\mathcal{F}} \\ 0 \end{pmatrix} = \nabla_{\Theta_1}(\mathcal{R}\mathcal{S}\mathcal{T}) \begin{bmatrix} X_{\mathcal{C}}^T \\ Y_{\mathcal{C}}^T \\ 1 \end{bmatrix} + \mathcal{R}\mathcal{S}\mathcal{T} \begin{bmatrix} \nabla_{\Theta_1} X_{\mathcal{C}} \\ \nabla_{\Theta_1} Y_{\mathcal{C}} \\ 0 \end{bmatrix} \tag{A.9}$$
$$\Theta_1 = \{k_1, l_a, l_b\}$$

Where

$$\begin{aligned} \nabla_{\Theta_1}(\mathcal{R}\mathcal{S}\mathcal{T}) = \frac{\partial \mathcal{R}_1}{\partial \Theta_1}\mathcal{R}_2\mathcal{R}_3\mathcal{S}\mathcal{T} + \mathcal{R}_1\mathcal{R}_2\frac{\partial \mathcal{R}_3}{\partial \Theta_1}\mathcal{S}\mathcal{T} \\ + \mathcal{R}\frac{\partial \mathcal{S}_1}{\partial \Theta_1}\mathcal{S}_2\mathcal{S}_3\mathcal{T} + \mathcal{R}\mathcal{S}_1\mathcal{S}_2\frac{\partial \mathcal{S}_3}{\partial \Theta_1}\mathcal{T} \\ + \mathcal{R}\mathcal{S}\frac{\partial \mathcal{T}}{\partial \Theta_1}\Big\} \end{aligned} \tag{A.10}$$

Then, calculation of partial derivatives for Rotation $\mathcal{R}$, Scalling $\mathcal{S}$ and Translation $\mathcal{T}$ transformation:

$$\mathcal{S}_1 \text{ or } \mathcal{R}_1 = \begin{bmatrix} 1 & 0 & X_{sr} \\ 0 & 1 & Y_{sr} \\ 0 & 0 & 1 \end{bmatrix}, \qquad \mathcal{S}_3 \text{ or } \mathcal{R}_3 = \begin{bmatrix} 1 & 0 & -X_{sr} \\ 0 & 1 & -Y_{sr} \\ 0 & 0 & 1 \end{bmatrix} \tag{A.11}$$

$$\nabla_{w_s}\mathcal{S} = \mathcal{S}_1 \begin{bmatrix} 1 & 0 & 0 \\ 0 & 0 & 0 \\ 0 & 0 & 0 \end{bmatrix} \mathcal{S}_3, \qquad \nabla_{h_s}\mathcal{S} = \mathcal{S}_1 \begin{bmatrix} 0 & 0 & 0 \\ 0 & 1 & 0 \\ 0 & 0 & 0 \end{bmatrix} \mathcal{S}_3 \tag{A.12}$$

$$\nabla_\beta \mathcal{R} = \mathcal{R}_1 \begin{bmatrix} -\sin(\beta) & -\cos(\beta) & 0 \\ \cos(\beta) & -\sin(\beta) & 0 \\ 0 & 0 & 0 \end{bmatrix} \mathcal{R}_3 \tag{A.13}$$

$$\begin{aligned} \nabla_{\Theta_1} \mathcal{R}_1 = & -\nabla_{\Theta_1} \mathcal{R}_3 = \nabla_{\Theta_1} \mathcal{S}_1 \\ = & -\nabla_{\Theta_1} \mathcal{S}_3 = \begin{bmatrix} 0 & 0 & \nabla_{\Theta_1} X_{sr} \\ 0 & 0 & \nabla_{\Theta_1} Y_{sr} \\ 0 & 0 & 0 \end{bmatrix} \end{aligned} \tag{A.14}$$

where

$$\begin{pmatrix} \nabla_{\Theta_1} X_{sr} \\ \nabla_{\Theta_1} Y_{sr} \\ 0 \end{pmatrix} = \nabla_{\Theta_1} \mathcal{T} \begin{bmatrix} X_{\mathcal{C}} \\ Y_{\mathcal{C}} \\ 1 \end{bmatrix} + \mathcal{T} \begin{bmatrix} \nabla_{\Theta_1} X_{\mathcal{C}} \\ \nabla_{\Theta_1} Y_{\mathcal{C}} \\ 0 \end{bmatrix} \tag{A.15}$$

$$\mathcal{T} = \begin{bmatrix} 1 & 0 & X_t \\ 0 & 1 & Y_t \\ 0 & 0 & 1 \end{bmatrix}, \qquad \nabla_{\Theta_1} \mathcal{T} = \begin{bmatrix} 0 & 0 & -\nabla_{\Theta_1} X_t \\ 0 & 0 & -\nabla_{\Theta_1} Y_t \\ 0 & 0 & 0 \end{bmatrix} \tag{A.16}$$

$$\begin{aligned} \nabla_{k_1} X_{\mathcal{I}} = & -\frac{1}{2} s^3 \mathbb{Y}_2(k_1 s^2, k_2 s, \alpha_0), \\ \nabla_{k_1} Y_{\mathcal{I}} = & \frac{1}{2} s^3 \mathbb{X}_2(k_1 s^2, k_2 s, \alpha_0) \end{aligned} \tag{A.17}$$

$$\begin{aligned} & s = l_a + \Delta \cdot j, \qquad \Delta = \frac{l_b - l_a}{N-1}, \\ & j = 0, 1, 2, \cdots, N-1 \end{aligned} \tag{A.18}$$

$$\nabla_{l_a} s = 1 - \frac{1}{N-1} \cdot j, \quad \nabla_{l_a} s = \frac{1}{N-1} \cdot j \tag{A.19}$$

$$\begin{aligned} & \nabla_{\Theta_2} X = \nabla_{\Theta_2} s \; \mathscr{F}_{cos}, \qquad \nabla_{\Theta_2} Y = \nabla_{\Theta_2} s \; \mathscr{F}_{sin} \\ & \quad \Theta_2 = l_a, l_b \end{aligned} \tag{A.20}$$

BIBLIOGRAPHY

[1] E. Abbena, S. Salamon, and A. Gray. *Modern Differential Geometry of Curves and Surfaces with Mathematica*. Textbooks in Mathematics. CRC Press, 2017. ISBN: 9781420010312. URL: https://books.google.com/books?id=NDoPEAAAQBAJ.

[2] Farshid Alambeigi, Sahba Aghajani Pedram, Jason L. Speyer, Jacob Rosen, Iulian Iordachita, Russell H. Taylor, and Mehran Armand. "SCADE: Simultaneous Sensor Calibration and Deformation Estimation of FBG-Equipped Unmodeled Continuum Manipulators." In: *IEEE Transactions on Robotics* 36.1 (2020), pp. 222–239. DOI: 10.1109/TRO.2019.2946726.

[3] Janine M. Benyus. *Biomimicry: innovation inspired by nature*. New York : Morrow, 1997.

[4] Carl T. Bergstrom and Jevin D. West. "Why scatter plots suggest causality, and what we can do about it." In: (2018).

[5] E. Bertolazzi. *CLOTHOIDS: A C++ LIBRARY WITH MATLAB INTERFACE FOR THE HANDLING OF CLOTHOID CURVES*. https://ebertolazzi.github.io/Clothoids/. Last accessed May 2022. 2022.

[6] Enrico Bertolazzi and Marco Frego. "G1 fitting with clothoids." In: *Mathematical Methods in the Applied Sciences* (Mar. 2014).

[7] Enrico Bertolazzi and Marco Frego. "G1 fitting with clothoids." In: *Mathematical Methods in the Applied Sciences* 38.5 (2015), pp. 881–897. DOI: https://doi.org/10.1002/mma.3114.

[8] Sofien Bouaziz, Andrea Tagliasacchi, Hao Li, and Mark Pauly. "Modern Techniques and Applications for Real-Time Non-Rigid Registration." In: *SIGGRAPH ASIA 2016 Courses*. Macau: Association for Computing Machinery, 2016. ISBN: 9781450345385. DOI: 10.1145/2988458.2988490.

[9] W. D. Brush. "The Formation of Mechanical Tissue in the Tendrils of Passiflora caerulea as Influenced by Tension and Contact." In: *Botanical Gazette* 53 (), pp. 453 –477.

[10] Jessica Burgner-Kahrs, D. Caleb Rucker, and Howie Choset. "Continuum Robots for Medical Applications: A Survey." In: *IEEE Transactions on Robotics* 31.6 (2015), pp. 1261–1280. DOI: 10.1109/TRO.2015.2489500.

[11] Jason Burris, Scott Lenaghan, and C. Stewart. "Climbing plants: attachment adaptations and bioinspired innovations." In: *Plant Cell Reports* (Nov. 2017).

[12] David B. Camarillo, Christopher F. Milne, Christopher R. Carlson, Michael R. Zinn, and J. Kenneth Salisbury. "Mechanics Modeling of Tendon-Driven Continuum Manipulators." In: *IEEE Transactions on Robotics* 24.6 (2008), pp. 1262–1273. DOI: 10.1109/TRO.2008.2002311.

[13] E. Wassim Chehab, Elizabeth Eich, and Janet Braam. "Thigmomorphogenesis: a complex plant response to mechano-stimulation." In: *Journal of Experimental Botany* 60.1 (Dec. 2008), pp. 43–56.

[14] Hao Cheng, Hongji Shang, Bin Lan, Houde Liu, Xueqian Wang, and Bin Liang. "Orientation to Pose: Continuum Robots Shape Sensing Based on Piecewise Polynomial Curvature Model." In: *CoRR* abs/2103.05150 (2021). arXiv: 2103.05150.

[15] Yash Chitalia, Nancy Joanna Deaton, Seokhwan Jeong, Nahian Rahman, and Jaydev P. Desai. "Towards FBG-Based Shape Sensing for Micro-Scale and Meso-Scale Continuum Robots With Large Deflection." In: *IEEE Robotics and Automation Letters* 5.2 (2020), pp. 1712–1719. DOI: 10.1109/LRA.2020.2969934.

[16] Margaret M. Coad, Laura H. Blumenschein, Sadie Cutler, Javier A. Reyna Zepeda, Nicholas D. Naclerio, Haitham El-Hussieny, Usman Mehmood, Jee-Hwan Ryu, Elliot W. Hawkes, and Allison M. Okamura. "Vine Robots: Design, Teleoperation, and Deployment for Navigation and Exploration." In: *IEEE Robotics Automation Magazine* 27.3 (2020), pp. 120–132. DOI: 10.1109/MRA.2019.2947538.

[17] Jordan M. Croom, D. Caleb Rucker, Joseph M. Romano, and Robert J. Webster. "Visual sensing of continuum robot shape using self-organizing maps." In: *2010 IEEE International Conference on Robotics and Automation*. 2010, pp. 4591–4596. DOI: 10.1109/ROBOT.2010.5509461.

[18] D.T.DOUGAL. "Tendrils of Passiflora caerulea II External phenomena of irritability and coiling." In: *Botanical Gazette* (1893).

[19] D.T.MAC.DOUGAL. "Tendrils of Passiflora caerulea I. Morphology and anatomy." In: *Botanical Gazette* (1892).

[20] Mohsen Moradi Dalvand, Saeid Nahavandi, and Robert D Howe. "Fast vision-based catheter 3D reconstruction." In: *Physics in Medicine and Biology* 61.14 (2016), pp. 5128–5148. DOI: 10.1088/0031-9155/61/14/5128.

[21] P. Dario, G. Sandini, P. Aebischer, and North Atlantic Treaty Organization. Scientific Affairs Division. *Robots and Biological Systems: Towards a New Bionics?: Towards a New Bionics? ; [proceedings of the NATO Advanced Research Workshop on Robots and Biological Systems, Held at Il Ciocco, Toscana, Italy, June 26 - 30,*

1989]. NATO ASI Series. Springer Berlin Heidelberg, 1993. ISBN: 9783540561583.

[22] Charles Darwin. *The Movements and Habits of Climbing Plants*. London: John Murray, 1875.

[23] Cosimo Della Santina, Robert K. Katzschmann, Antonio Biechi, and Daniela Rus. "Dynamic control of soft robots interacting with the environment." In: *2018 IEEE International Conference on Soft Robotics (RoboSoft)*. 2018, pp. 46–53. DOI: 10.1109/ROBOSOFT.2018.8404895.

[24] Heiko Donat, Jiecong Gu, and Jochen J. Steil. "Real-Time Shape Estimation for Concentric Tube Continuum Robots with a Single Force/Torque Sensor." In: *Frontiers in Robotics and AI* 8 (2021). ISSN: 2296-9144. DOI: 10.3389/frobt.2021.734033.

[25] Alessio Dore, Gabrijel Smoljkic, Emmanuel Vander Poorten, Mauro Sette, Jos Vander Sloten, and Guang-Zhong Yang. "Catheter navigation based on probabilistic fusion of electromagnetic tracking and physically-based simulation." In: *2012 IEEE/RSJ International Conference on Intelligent Robots and Systems*. 2012, pp. 3806–3811. DOI: 10.1109/IROS.2012.6386139.

[26] Azadeh Doroudchi, Roozbeh Khodambashi, Amir Salimi Lafmejani, Daniel M. Aukes, and Spring Berman. "Dynamic Modeling of a Hydrogel-based Continuum Robotic Arm with Experimental Validation." In: *2020 3rd IEEE International Conference on Soft Robotics (RoboSoft)*. 2020, pp. 695–701. DOI: 10.1109/RoboSoft48309.2020.9116012.

[27] Pierre E. Dupont, Jesse Lock, Brandon Itkowitz, and Evan Butler. "Design and Control of Concentric-Tube Robots." In: *IEEE Transactions on Robotics* 26.2 (2010), pp. 209–225. DOI: 10.1109/TRO.2009.2035740.

[28] Matlab File Exchange. *2D - 2D Projective Homography (3x3) Estimation*. https://www.mathworks.com/matlabcentral/fileexchange/28760-2d-2d-projective-homography-3x3-estimation. Last accessed May 2022. 2010.

[29] Ricardo Fabbri and Benjamin B. Kimia. "Multiview Differential Geometry of Curves." In: *International Journal of Computer Vision* 120.3 (2016), pp. 324–346. ISSN: 1573-1405. DOI: 10.1007/s11263-016-0912-7.

[30] Jie Fan, Emanuela Del Dottore, Francesco Visentin, and Barbara Mazzolai. "Image-based Approach to Reconstruct Curling in Continuum Structures." In: *2020 3rd IEEE International Conference on Soft Robotics (RoboSoft)*. 2020, pp. 544–549. DOI: 10.1109/RoboSoft48309.2020.9115981.

[31] Jie Fan, Francesco Visentin, Emanuela Del Dottore, and Barbara Mazzolai. "An Image-Based Method for the Morphological Analysis of Tendrils with 2D Piece-Wise Clothoid Approximation Model." In: *Biomimetic and Biohybrid Systems*. 2020, pp. 80–91. ISBN: 978-3-030-64313-3.

[32] Ge Fang, Xiaomei Wang, Kui Wang, Kit-Hang Lee, Justin D. L. Ho, Hing-Choi Fu, Denny Kin Chung Fu, and Ka-Wai Kwok. "Vision-Based Online Learning Kinematic Control for Soft Robots Using Local Gaussian Process Regression." In: *IEEE Robotics and Automation Letters* 4.2 (2019), pp. 1194–1201. DOI: 10.1109/LRA.2019.2893691.

[33] P E Fayemi, K Wanieck, C Zollfrank, N Maranzana, and A Aoussat. "Biomimetics: process, tools and practice." In: *Bioinspiration&Biomimetics* 12.1 (2017), p. 011002. DOI: 10.1088/1748-3190/12/1/011002.

[34] "Festo bionic handling assistant." In: (). URL: https://www.festo.com/us/en/e/about-festo/research-and-development/bionic-learning-network/highlights-from-2010-to-2012/bionic-handling-assistant-id_33759/.

[35] Nicolas Franceschini, Franck Ruffier, and Julien Serres. "A Bio-Inspired Flying Robot Sheds Light on Insect Piloting Abilities." In: *Current Biology* 17.4 (2007), pp. 329–335. ISSN: 0960-9822. DOI: https://doi.org/10.1016/j.cub.2006.12.032.

[36] Kevin C. Galloway, Yue Chen, Emily Templeton, Brian Rife, Isuru S. Godage, and Eric J. Barth. "Fiber Optic Shape Sensing for Soft Robotics." In: *Soft Robotics* 6.5 (2019). PMID: 31241408, pp. 671–684. DOI: 10.1089/soro.2018.0131.

[37] Yusof Ganji * and Farrokh Janabi-Sharifi. "Catheter Kinematics for Intracardiac Navigation." In: *IEEE Transactions on Biomedical Engineering* 56.3 (2009), pp. 621–632. DOI: 10.1109/TBME.2009.2013134.

[38] M Gazzola, LH Dudte, AG McCormick, and L Mahadevan. "Forward and inverse problems in the mechanics of soft filaments." In: *Royal Society open science* 5.6 (2018), p. 171628. DOI: 10.1098/rsos.171628.

[39] Isuru S. Godage, David T. Branson, Emanuele Guglielmino, Gustavo A. Medrano-Cerda, and Darwin G. Caldwell. "Shape function-based kinematics and dynamics for variable length continuum robotic arms." In: *2011 IEEE International Conference on Robotics and Automation*. 2011, pp. 452–457. DOI: 10.1109/ICRA.2011.5979607.

[40] Isuru S Godage, Gustavo A Medrano-Cerda, David T Branson, Emanuele Guglielmino, and Darwin G Caldwell. "Modal kinematics for multisection continuum arms." In: *Bioinspiration and Biomimetics* 10.3 (2015), p. 035002. DOI: 10.1088/1748-3190/10/3/035002.

[41] Isuru S. Godage, Robert J. Webster, and Ian D. Walker. "Center-of-Gravity-Based Approach for Modeling Dynamics of Multisection Continuum Arms." In: *IEEE Transactions on Robotics* 35.5 (2019), pp. 1097–1108. DOI: 10.1109/TRO.2019.2921153.

[42] Tipakorn Greigarn, Nate Lombard Poirot, Xinyang Xu, and M. Cenk Çavuşoğlu. "Jacobian-Based Task-Space Motion Planning for MRI-Actuated Continuum Robots." In: *IEEE Robotics and Automation Letters* 4.1 (2019), pp. 145–152. DOI: 10.1109/LRA.2018.2881987.

[43] Tipakorn Greigarn and M. Cenk Çavuşoğlu. "Pseudo-rigid-body model and kinematic analysis of MRI-actuated catheters." In: *2015 IEEE International Conference on Robotics and Automation (ICRA)*. 2015, pp. 2236–2243. DOI: 10.1109/ICRA.2015.7139495.

[44] Li Guiqing, Li Xianmin, and Li Hua. "3D discrete clothoid splines." In: *Proceedings. Computer Graphics International 2001*. 2001, pp. 321–324. DOI: 10.1109/CGI.2001.934690.

[45] Gur Harary and Ayellet Tal. "3D Euler Spirals for 3D Curve Completion." In: *Proceedings of the Twenty-Sixth Annual Symposium on Computational Geometry*. SoCG '10. Snowbird, Utah, USA: Association for Computing Machinery, 2010, pp. 393–402. ISBN: 9781450300162. DOI: 10.1145/1810959.1811025.

[46] Gur Harary and Ayellet Tal. "3D Euler spirals for 3D curve completion." In: *Computational Geometry* 45.3 (2012), pp. 115–126. ISSN: 0925-7721. DOI: https://doi.org/10.1016/j.comgeo.2011.10.001.

[47] Elliot W. Hawkes, Laura H. Blumenschein, Joseph D. Greer, and Allison M. Okamura. "A soft robot that navigates its environment through growth." In: *Science Robotics* 2.8 (2017), eaan3028. DOI: 10.1126/scirobotics.aan3028.

[48] Mark A. Heald. "Rational approximations for the Fresnel integrals." In: 1985.

[49] Donald D. Hearn and M. Pauline Baker. *Handbook of Mathematical Functions, With Formulas, Graphs, and Mathematical Tables*. 3rd ed. Prentice Hall, 1974, pp. 239–246.

[50] Qiulin Hou, Changhou Lu, and Xueyong Li. "A novel pose sensing model for soft manipulator based on helical FBG." In: *Sensors and Actuators A: Physical* 321 (2021), p. 112586. ISSN: 0924-4247. DOI: https://doi.org/10.1016/j.sna.2021.112586.

[51] Kaiwen Hsiao and Hiromi Mochiyama. "A wire-driven continuum manipulator model without assuming shape curvature constancy." In: *2017 IEEE/RSJ International Conference on Intelligent Robots and Systems (IROS)*. 2017, pp. 436–443. DOI: 10.1109/IROS.2017.8202190.

[52] Shuangwei Hu, Martin Lundgren, and Antti J. Niemi. "Discrete Frenet frame, inflection point solitons, and curve visualization with applications to folded proteins." In: *Phys. Rev. E* 83 (6 2011), p. 061908. DOI: 10.1103/PhysRevE.83.061908.

[53] Hui Huang, Shihao Wu, Daniel Cohen-Or, Minglun Gong, Hao Zhang, Guiqing Li, and Baoquan Chen. "L1-Medial Skeleton of Point Cloud." In: *ACM Trans. Graph.* 32.4 (2013). ISSN: 0730-0301. DOI: 10.1145/2461912.2461913.

[54] Shaoping Huang, Deshan Meng, Xueqian Wang, Bin Liang, and Weining Lu. "A 3D Static Modeling Method and Experimental Verification of Continuum Robots Based on Pseudo-Rigid Body Theory." In: *2019 IEEE/RSJ International Conference on Intelligent Robots and Systems (IROS)*. 2019, pp. 4672–4677. DOI: 10.1109/IROS40897.2019.8968526.

[55] ISO/TC266. *Biomimetics-Terminology, concepts and methodology*. Berlin:Beuth, 2015. ISBN: 9780580813207.

[56] M. J. Jaffe. "Physiological Studies on Pea Tendrils: VI. The Characteristics of Sensory Perception and Transduction." In: *Plant Physiology* 45.6 (1970), pp. 756–760. ISSN: 00320889, 15322548.

[57] M. J. Jaffe and A. W. Galston. "Physiological Studies on Pea Tendrils. I. Growth and Coiling Following Mechanical Stimulation." In: *Plant Physiology* 41.6 (June 1966), pp. 1014–1025. ISSN: 0032-0889.

[58] M.J. Jaffe. "Thigmomorphogenesis: The Response of Plant Growth and Development to Mechanical Stimulation: With Special Reference to Bryonia dioica." In: *Planta* 114.2 (1973), pp. 143–157. ISSN: 00320935, 14322048. URL: http://www.jstor.org/stable/23370789 (visited on 07/07/2022).

[59] Farrokh Janabi-Sharifi, Amir Jalali, and Ian D. Walker. "Cosserat Rod-Based Dynamic Modeling of Tendon-Driven Continuum Robots: A Tutorial." In: *IEEE Access* 9 (2021), pp. 68703–68719. DOI: 10.1109/ACCESS.2021.3077186.

[60] Alan R. Jones. *Best Fit Lines &Curves*. Routledge, 2018.

[61] Rongjie Kang, Yong Guo, Lisha Chen, David T. Branson, and Jian S. Dai. "Design of a Pneumatic Muscle Based Continuum Robot With Embedded Tendons." In: *IEEE/ASME Transactions on Mechatronics* 22.2 (2017), pp. 751–761. DOI: 10.1109/TMECH.2016.2636199.

[62] Robert K. Katzschmann, Cosimo Della Santina, Yasunori Toshimitsu, Antonio Bicchi, and Daniela Rus. "Dynamic Motion Control of Multi-Segment Soft Robots Using Piecewise Constant Curvature Matched with an Augmented Rigid Body Model." In: *2019 2nd IEEE International Conference on Soft Robotics (RoboSoft)*. 2019, pp. 454–461. DOI: 10.1109/ROBOSOFT.2019.8722799.

[63] Kleoniki Keklikoglou et al. "Micro-CT for Biological and Biomedical Studies: A Comparison of Imaging Techniques." In: *Journal of Imaging* 7.9 (2021). ISSN: 2313-433X.

[64] Sangbae Kim, Matthew Spenko, Salomon Trujillo, Barrett Heyneman, Daniel Santos, and Mark R. Cutkosky. "Smooth Vertical Surface Climbing With Directional Adhesion." In: *IEEE Transactions on Robotics* 24 (2008), pp. 65–74.

[65] P. D. Kovesi. *MATLAB and Octave Functions for Computer Vision and Image Processing*. Available from: https://www.peterkovesi.com/matlabfns/.

[66] T. LUO, H. CHEN, and G.S. KASSAB. "3D reconstruction of elastin fibres in coronary adventitia." In: *Journal of Microscopy* 265.1 (2017), pp. 121–131. DOI: https://doi.org/10.1111/jmi.12470.

[67] Edward Lambert, Richard Romano, and David Watling. "Optimal Path Planning with Clothoid Curves for Passenger Comfort." In: May 2019, pp. 609–615. DOI: 10.5220/0007801806090615.

[68] Cecilia Laschi, Matteo Cianchetti, Barbara Mazzolai, Laura Margheri, Maurizio Follador, and Paolo Dario. "Soft robot arm inspired by the octopus." In: *Advanced robotics* 26.7 (2012), pp. 709–727.

[69] Cecilia Laschi, Barbara Mazzolai, and Matteo Cianchetti. "Soft robotics: Technologies and systems pushing the boundaries of robot abilities." In: *Science Robotics* 1.1 (2016), eaah3690. DOI: 10.1126/scirobotics.aah3690. eprint: https://www.science.org/doi/pdf/10.1126/scirobotics.aah3690. URL: https://www.science.org/doi/abs/10.1126/scirobotics.aah3690.

[70] In-Kwon Lee. "Curve reconstruction from unorganized points." In: *Computer Aided Geometric Design* (2000).

[71] Kit-Hang Lee, Denny K.C. Fu, Martin C.W. Leong, Marco Chow, Hing-Choi Fu, Kaspar Althoefer, Kam Yim Sze, Chung-Kwong Yeung, and Ka-Wai Kwok. "Nonparametric Online Learning Control for Soft Continuum Robot: An Enabling Technique for Effective Endoscopic Navigation." In: *Soft Robotics* 4.4 (2017). PMID: 29251567, pp. 324–337. DOI: 10.1089/soro.2016.0065.

[72] Raphael Linus Levien. "From Spiral to Spline: Optimal Techniques in Interactive Curve Design." PhD thesis. EECS Department, University of California, Berkeley, 2009. URL: http://www2.eecs.berkeley.edu/Pubs/TechRpts/2009/EECS-2009-162.html.

[73] Guo Li, Ligang Liu, Hanlin Zheng, and Niloy J. Mitra. "Analysis, Reconstruction and Manipulation Using Arterial Snakes." In: *ACM SIGGRAPH Asia 2010 Papers*. SIGGRAPH ASIA '10. Seoul, South Korea: Association for Computing Machinery, 2010. ISBN: 9781450304399. DOI: 10.1145/1866158.1866178.

[74] Shiwei Li, Yao Yao, Tian Fang, and Long Quan. "Reconstructing Thin Structures of Manifold Surfaces by Integrating Spatial Curves." In: *2018 IEEE/CVF Conference on Computer Vision and Pattern Recognition*. 2018, pp. 2887–2896. DOI: 10.1109/CVPR.2018.00305.

[75] Sungyeop Lim and Soonhung Han. "Helical extension method for solving the natural equation of a space curve." In: 5.3 (2017), p. 035002. DOI: 10.1088/2051-672x/aa7ea8.

[76] Jindong Liu, Yuchuang Tong, and Jinguo Liu. "Review of snake robots in constrained environments." In: *Robotics and Autonomous Systems* 141 (2021), p. 103785. ISSN: 0921-8890. DOI: https://doi.org/10.1016/j.robot.2021.103785.

[77] Lingjie Liu, Duygu Ceylan, Cheng Lin, Wenping Wang, and Niloy J. Mitra. "Image-Based Reconstruction of Wire Art." In: *ACM Trans. Graph.* 36.4 (2017). ISSN: 0730-0301. DOI: 10.1145/3072959.3073682.

[78] Tobias Mahl, Alexander Hildebrandt, and Oliver Sawodny. "A Variable Curvature Continuum Kinematics for Kinematic Control of the Bionic Handling Assistant." In: *IEEE Transactions on Robotics* 30.4 (2014), pp. 935–949. DOI: 10.1109/TRO.2014.2314777.

[79] Arthur W. Mahoney, Hunter B. Gilbert, and Robert J. Webster III. "A REVIEW OF CONCENTRIC TUBE ROBOTS: MODELING, CONTROL, DESIGN, PLANNING, AND SENSING." In: *The Encyclopedia of Medical Robotics*. 2018. Chap. Chapter 7, pp. 181–202. DOI: 10.1142/9789813232266_0007.

[80] Andrew D Marchese, Cagdas D Onal, and Daniela Rus. "Autonomous soft robotic fish capable of escape maneuvers using fluidic elastomer actuators." In: *Soft robotics* 1.1 (2014), pp. 75–87.

[81] Tobias Martin, Juan Montes, Jean-Charles Bazin, and Tiberiu Popa. "Topology-Aware Reconstruction of Thin Tubular Structures." In: *SIGGRAPH Asia 2014 Technical Briefs*. SA '14. Shen-

zhen, China: Association for Computing Machinery, 2014. ISBN: 9781450328951. DOI: 10.1145/2669024.2669035.

[82] Shuhei Miyashita, Steven Guitron, Kazuhiro Yoshida, Shuguang Li, Dana D. Damian, and Daniela Rus. "Ingestible, controllable, and degradable origami robot for patching stomach wounds." In: *2016 IEEE International Conference on Robotics and Automation (ICRA)* (2016), pp. 909–916.

[83] Henry P. Moreton and Carlo H. Séquin. "Scale-Invariant Minimum-Cost Curves: Fair and Robust Design Implements." In: *Computer Graphics Forum* 12.3 (1993), pp. 473–484. DOI: https://doi.org/10.1111/1467-8659.1230473. eprint: https://onlinelibrary.wiley.com/doi/pdf/10.1111/1467-8659.1230473. URL: https://onlinelibrary.wiley.com/doi/abs/10.1111/1467-8659.1230473.

[84] Matthias Muller, Bruno Heidelberger, Matthias Teschner, and Markus Gross. "Meshless Deformations Based on Shape Matching." In: *ACM Transactions on Graphics* 24.3 (July 2005), pp. 471–478. ISSN: 0730-0301.

[85] Indrek Must, Edoardo Sinibaldi, and Barbara Mazzolai. "A variable-stiffness tendril-like soft robot based on reversible osmotic actuation." In: *Nature Communications* 10 (Jan. 2019). DOI: 10.1038/s41467-018-08173-y.

[86] NDI. *Aurora Electromagnetic Tracking Solution*. https://www.ndigital.com/electromagnetic-tracking-technology/aurora/. Last accessed May 2022. 2022.

[87] Noel Naughton, Jiarui Sun, Arman Tekinalp, Tejaswin Parthasarathy, Girish Chowdhary, and Mattia Gazzola. "Elastica: A Compliant Mechanics Environment for Soft Robotic Control." In: *IEEE Robotics and Automation Letters* 6.2 (2021), pp. 3389–3396. DOI: 10.1109/LRA.2021.3063698.

[88] David Navarro-Alarcon and Yun-Hui Liu. "Fourier-Based Shape Servoing: A New Feedback Method to Actively Deform Soft Objects into Desired 2-D Image Contours." In: *IEEE Transactions on Robotics* 34.1 (2018), pp. 272–279. DOI: 10.1109/TRO.2017.2765333.

[89] Marika Neumann and Jessica Burgner-Kahrs. "Considerations for follow-the-leader motion of extensible tendon-driven continuum robots." In: *2016 IEEE International Conference on Robotics and Automation (ICRA)* (2016), pp. 917–923.

[90] Leslie Ng, Mark A. Elgar, and Devi Stuart-Fox. "From Bioinspired to Bioinformed: Benefits of Greater Engagement From Biologists." In: *Frontiers in Ecology and Evolution* 9 (2021). ISSN: 2296-701X. DOI: 10.3389/fevo.2021.790270.

[91] S Ohrhallinger, Amal Dev Parakkat, and J Peethambaran. *Shape Reconstruction in 2D: From Theory to Practice*. Eurographics 2022 - Tutorial. Apr. 2022.

[92] Yong-Lae Park, Santhi Elayaperumal, Bruce Daniel, Seok Chang Ryu, Mihye Shin, Joan Savall, Richard J. Black, Behzad Moslehi, and Mark R. Cutkosky. "Real-Time Estimation of 3-D Needle Shape and Deflection for MRI-Guided Interventions." In: *IEEE/ASME Transactions on Mechatronics* 15.6 (2010), pp. 906–915. DOI: 10.1109/TMECH.2010.2080360.

[93] Ryan S. Penning and Michael R. Zinn. "A combined modal-joint space control approach for continuum manipulators." In: *Advanced Robotics* 28.16 (2014), pp. 1091–1108. DOI: 10.1080/01691864.2014.913503.

[94] Qiao Qiao, Gianni Borghesan, Joris De Schutter, and Emmanuel Vander Poorten. "Force from Shape—Estimating the Location and Magnitude of the External Force on Flexible Instruments." In: *IEEE Transactions on Robotics* 37.5 (2021), pp. 1826–1833. DOI: 10.1109/TRO.2021.3062504.

[95] Priyanka Rao, Quentin Peyron, Sven Lilge, and Jessica Burgner-Kahrs. "How to Model Tendon-Driven Continuum Robots and Benchmark Modelling Performance." In: *Frontiers in Robotics and AI* 7 (2021). ISSN: 2296-9144. DOI: 10.3389/frobt.2020.630245.

[96] Tobias Reichl, José Gardiazabal, and Nassir Navab. "Electromagnetic Servoing—A New Tracking Paradigm." In: *IEEE Transactions on Medical Imaging* 32.8 (2013), pp. 1526–1535. DOI: 10.1109/TMI.2013.2259636.

[97] Federico Renda, Frédéric Boyer, Jorge Dias, and Lakmal Seneviratne. "Discrete Cosserat Approach for Multisection Soft Manipulator Dynamics." In: *IEEE Transactions on Robotics* 34.6 (2018), pp. 1518–1533. DOI: 10.1109/TRO.2018.2868815.

[98] III Robert J. Webster and Bryan A. Jones. "Design and Kinematic Modeling of Constant Curvature Continuum Robots: A Review." In: *The International Journal of Robotics Research* 29.13 (2010), pp. 1661–1683. DOI: 10.1177/0278364910368147.

[99] Roy J. Roesthuis, Marco Kemp, John J. van den Dobbelsteen, and Sarthak Misra. "Three-Dimensional Needle Shape Reconstruction Using an Array of Fiber Bragg Grating Sensors." In: *IEEE/ASME Transactions on Mechatronics* 19.4 (2014), pp. 1115–1126. DOI: 10.1109/TMECH.2013.2269836.

[100] Roy J. Roesthuis and Sarthak Misra. "Steering of Multisegment Continuum Manipulators Using Rigid-Link Modeling and FBG-Based Shape Sensing." In: *IEEE Transactions on Robotics* 32.2 (2016), pp. 372–382. DOI: 10.1109/TRO.2016.2527047.

[101] Susan Heyner Rogers K. Joshi and Edna R. Green. In: *biology. Encyclopedia Britannica* 25 (2019). URL: https://www.britannica.com/science/biology.

[102] Benoît Rosa, Valentin Bordoux, and Florent Nageotte. "Combining Differential Kinematics and Optical Flow for Automatic Labeling of Continuum Robots in Minimally Invasive Surgery." In: *Frontiers in Robotics and AI* 6 (2019). ISSN: 2296-9144. DOI: 10.3389/frobt.2019.00086.

[103] D. Caleb Rucker and Robert J. Webster III. "Statics and Dynamics of Continuum Robots With General Tendon Routing and External Loading." In: *IEEE Transactions on Robotics* 27.6 (2011), pp. 1033–1044. DOI: 10.1109/TRO.2011.2160469.

[104] Hwan-Taek Ryu, Jaehong Woo, Byung-Rok So, and Byung-Ju Yi. "Shape and Contact Force Estimation of Inserted Flexible Medical Device." In: *International Journal of Control, Automation and Systems* 18.1 (2020), pp. 163–174. ISSN: 2005-4092. DOI: 10.1007/s12555-019-0237-8.

[105] S. M. Hadi Sadati, S. Elnaz Naghibi, Ali Shiva, Yohan Noh, Aditya Gupta, Ian D. Walker, Kaspar Althoefer, and Thrishantha Nanayakkara. "A Geometry Deformation Model for Braided Continuum Manipulators." In: *Frontiers in Robotics and AI* 4 (2017). ISSN: 2296-9144. DOI: 10.3389/frobt.2017.00022.

[106] S.M. Hadi Sadati et al. "TMTDyn: A Matlab package for modeling and control of hybrid rigid–continuum robots based on discretized lumped systems and reduced-order models." In: *The International Journal of Robotics Research* 40.1 (2021), pp. 296–347. DOI: 10.1177/0278364919881685.

[107] A Sadeghi, A Mondini, E Del Dottore, V Mattoli, L Beccai, S Taccola, C Lucarotti, M Totaro, and B Mazzolai. "A plant-inspired robot with soft differential bending capabilities." In: *Bioinspiration & Biomimetics* 12.1 (2016), p. 015001. DOI: 10.1088/1748-3190/12/1/015001. URL: https://doi.org/10.1088/1748-3190/12/1/015001.

[108] Ali Sadeghi, Alessio Mondini, and Barbara Mazzolai. "Preliminary Experimental Study on Variable Stiffness Structures Based on Textile Jamming for Wearable Robotics." In: *Wearable Robotics: Challenges and Trends*. Ed. by Maria Chiara Carrozza, Silvestro Micera, and José L. Pons. Cham: Springer International Publishing, 2019, pp. 49–52. ISBN: 978-3-030-01887-0.

[109] Hossein Sadjadi, Keyvan Hashtrudi-Zaad, and Gabor Fichtinger. "Fusion of Electromagnetic Trackers to Improve Needle Deflection Estimation: Simulation Study." In: *IEEE Transactions on Biomedical Engineering* 60.10 (2013), pp. 2706–2715. DOI: 10.1109/TBME.2013.2262658.

[110] Hossein Sadjadi, Keyvan Hashtrudi-Zaad, and Gabor Fichtinger. "Simultaneous Electromagnetic Tracking and Calibration for Dynamic Field Distortion Compensation." In: *IEEE Transactions on Biomedical Engineering* 63.8 (2016), pp. 1771–1781. DOI: 10.1109/TBME.2015.2502138.

[111] Sujit Kumar Sahu, Canberk Sozer, Benoit Rosa, Izadyar Tamadon, Pierre Renaud, and Arianna Menciassi. "Shape Reconstruction Processes for Interventional Application Devices: State of the Art, Progress, and Future Directions." In: *Frontiers in Robotics and AI* 8 (2021). ISSN: 2296-9144. DOI: 10.3389/frobt.2021.758411.

[112] Cosimo Della Santina and Daniela Rus. "Control Oriented Modeling of Soft Robots: The Polynomial Curvature Case." In: *IEEE Robotics and Automation Letters* 5.2 (2020), pp. 290–298. DOI: 10.1109/LRA.2019.2955936.

[113] Sina Sareh, Yohan Noh, Min Li, Tommaso Ranzani, Hongbin Liu, and Kaspar Althoefer. "Macrobend optical sensing for pose measurement in soft robot arms." In: *Smart Materials and Structures* 24.12 (2015), p. 125024. DOI: 10.1088/0964-1726/24/12/125024.

[114] O Schmitt. "Third Int." In: *Biophysics Congress*. 1969, p. 297.

[115] Andrew K. Schulz, Madeline Boyle, Colin Boyle, Sophia Sordilla, Catalina Rincon, Scott Hooper, Catie Aubuchon, Joy S. Reidenberg, Claire Higgins, and David L. Hu. "Skin wrinkles and folds enable asymmetric stretch in the elephant trunk." In: *Proceedings of the National Academy of Sciences* 119.31 (2022), e2122563119. DOI: 10.1073/pnas.2122563119. eprint: https://www.pnas.org/doi/pdf/10.1073/pnas.2122563119. URL: https://www.pnas.org/doi/abs/10.1073/pnas.2122563119.

[116] Livia Scorza and Marcelo Dornelas. "Plants on the move: Toward common mechanisms governing mechanically-induced plant movements." In: *Plant signaling & behavior* 6 (Dec. 2011), pp. 1979–86. DOI: 10.4161/psb.6.12.18192.

[117] Julien R. Serres and Franck Ruffier. "Optic flow-based collision-free strategies: From insects to robots." In: *Arthropod Structure & Development* 46.5 (2017). From Insects to Robots, pp. 703–717. ISSN: 1467-8039. DOI: https://doi.org/10.1016/j.asd.2017.06.003.

[118] Luca Sestini, Benoit Rosa, Elena De Momi, Giancarlo Ferrigno, and Nicolas Padoy. "A Kinematic Bottleneck Approach for Pose Regression of Flexible Surgical Instruments Directly From Images." In: *IEEE Robotics and Automation Letters* 6.2 (2021), pp. 2938–2945. DOI: 10.1109/LRA.2021.3062308.

[119] Michael Shaw, Haoyun Zhan, Muna Elmi, Vijay Pawar, Clara Essmann, and Mandayam Srinivasan. "Three-dimensional behavioural phenotyping of freely moving C. Elegans using quantitative light field microscopy." In: *PLOS ONE* 13 (July 2018), e0200108. DOI: 10.1371/journal.pone.0200108.

[120] Robert F Shepherd, Filip Ilievski, Wonjae Choi, Stephen A Morin, Adam A Stokes, Aaron D Mazzeo, Xin Chen, Michael Wang, and George M Whitesides. "Multigait soft robot." In: *Proceedings of the national academy of sciences* 108.51 (2011), pp. 20400–20403.

[121] Chaoyang Shi, Xiongbiao Luo, Peng Qi, Tianliang Li, Shuang Song, Zoran Najdovski, Toshio Fukuda, and Hongliang Ren. "Shape Sensing Techniques for Continuum Robots in Minimally Invasive Surgery: A Survey." In: *IEEE Transactions on Biomedical Engineering* 64.8 (2017), pp. 1665–1678. DOI: 10.1109/TBME.2016.2622361.

[122] Chaoyang Shi, Carlos Tercero, Xianliang Wu, Seiichi Ikeda, Kimihiro Komori, Kiyohito Yamamoto, Fumihito Arai, and Toshio Fukuda. "Real-time in vitro intravascular reconstruction and navigation for endovascular aortic stent grafting." In: *The International Journal of Medical Robotics and Computer Assisted Surgery* 12.4 (2016), pp. 648–657. DOI: https://doi.org/10.1002/rcs.1736.

[123] Inderjeet Singh, Yacine Amara, Achille Melingui, Pushparaj Mani Pathak, and Rochdi Merzouki. "Modeling of Continuum Manipulators Using Pythagorean Hodograph Curves." In: *Soft Robotics* 5.4 (2018). PMID: 29746203, pp. 425–442. DOI: 10.1089/soro.2017.0111.

[124] Edoardo Sinibaldi, Alfredo Argiolas, Gian Luigi Puleo, and Barbara Mazzolai. "Another Lesson from Plants: The Forward Osmosis-Based Actuator." In: *PLOS ONE* 9 (July 2014), pp. 1–12. DOI: 10.1371/journal.pone.0102461.

[125] Shuang Song, Zheng Li, Max Q.-H. Meng, Haoyong Yu, and Hongliang Ren. "Real-Time Shape Estimation for Wire-Driven Flexible Robots With Multiple Bending Sections Based on Quadratic Bézier Curves." In: *IEEE Sensors Journal* 15.11 (2015), pp. 6326–6334. DOI: 10.1109/JSEN.2015.2456181.

[126] Shuang Song, Zheng Li, Max Q.-H. Meng, Haoyong Yu, and Hongliang Ren. "Real-Time Shape Estimation for Wire-Driven Flexible Robots With Multiple Bending Sections Based on Quadratic Bézier Curves." In: *IEEE Sensors Journal* 15.11 (2015), pp. 6326–6334. DOI: 10.1109/JSEN.2015.2456181.

[127] Shuang Song, Zheng Li, Haoyong Yu, and Hongliang Ren. "Shape reconstruction for wire-driven flexible robots based on Bézier curve and electromagnetic positioning." In: *Mechatronics* 29 (2015), pp. 28–35. ISSN: 0957-4158. DOI: https://doi.org/10.1016/j.mechatronics.2015.05.003.

[128] V. Sonneville, A. Cardona, and O. Brüls. "Geometrically exact beam finite element formulated on the special Euclidean group SE(3)." In: *Computer Methods in Applied Mechanics and Engineering* 268 (2014), pp. 451–474. ISSN: 0045-7825. DOI: https://doi.org/10.1016/j.cma.2013.10.008.

[129] Mariane S. Sousa-Baena, Lúcia G. Lohmann, José Hernandes-Lopes, and Neelima R. Sinha. "The molecular control of tendril development in angiosperms." In: *New Phytologist* 218.3 (2018).

[130] Damien Teney and Justus Piater. "Sampling-Based Multiview Reconstruction without Correspondences for 3D Edges." In: *2012 Second International Conference on 3D Imaging, Modeling, Processing, Visualization & Transmission*. 2012, pp. 160–167. DOI: 10.1109/3DIMPVT.2012.28.

[131] Eiter Thomas and Mannila Heikki. "Computing discrete Fréchet distance." In: 1994.

[132] John Till, Vincent Aloi, and Caleb Rucker. "Real-time dynamics of soft and continuum robots based on Cosserat rod models." In: *The International Journal of Robotics Research* 38.6 (2019), pp. 723–746. DOI: 10.1177/0278364919842269.

[133] Stephen Tully and Howie Choset. "A Filtering Approach for Image-Guided Surgery With a Highly Articulated Surgical Snake Robot." In: *IEEE Transactions on Biomedical Engineering* 63.2 (2016), pp. 392–402. DOI: 10.1109/TBME.2015.2461531.

[134] Anil Usumezbas, Ricardo Fabbri, and Benjamin B. Kimia. "From Multiview Image Curves to 3D Drawings." In: *Computer Vision – ECCV 2016*. Ed. by Bastian Leibe, Jiri Matas, Nicu Sebe, and Max Welling. Cham: Springer International Publishing, 2016, pp. 70–87. ISBN: 978-3-319-46493-0.

[135] Anil Usumezbas, Ricardo Fabbri, and Benjamin B. Kimia. "The Surfacing of Multiview 3D Drawings via Lofting and Occlusion Reasoning." In: *2017 IEEE Conference on Computer Vision and Pattern Recognition (CVPR)*. 2017, pp. 4560–4569. DOI: 10.1109/CVPR.2017.485.

[136] Alberto Vaccarella, Elena De Momi, Andinet Enquobahrie, and Giancarlo Ferrigno. "Unscented Kalman Filter Based Sensor Fusion for Robust Optical and Electromagnetic Tracking in Surgical Navigation." In: *IEEE Transactions on Instrumentation and Measurement* 62.7 (2013), pp. 2067–2081. DOI: 10.1109/TIM.2013.2248304.

[137] Alessandro Vandini, Antonino Salerno, Christopher J. Payne, and Guang-Zhong Yang. "Vision-based motion control of a flexible robot for surgical applications." In: *2014 IEEE International Conference on Robotics and Automation (ICRA)*. 2014, pp. 6205–6211. DOI: 10.1109/ICRA.2014.6907774.

[138] Tomas da Veiga, James H Chandler, Peter Lloyd, Giovanni Pittiglio, Nathan J Wilkinson, Ali K Hoshiar, Russell A Harris, and Pietro Valdastri. "Challenges of continuum robots in clinical context: a review." In: *Progress in Biomedical Engineering* 2.3 (2020), p. 032003. DOI: 10.1088/2516-1091/ab9f41.

[139] Venkatasubramanian Kalpathy Venkiteswaran, Jakub Sikorski, and Sarthak Misra. "Shape and contact force estimation of continuum manipulators using pseudo rigid body models." In: *Mechanism and Machine Theory* 139 (2019), pp. 34–45. ISSN: 0094-114X. DOI: https://doi.org/10.1016/j.mechmachtheory.2019.04.008.

[140] Renato Vidoni, Tanja Mimmo, and Camilla Pandolfi. "Tendril-Based Climbing Plants to Model, Simulate and Create Bio-Inspired Robotic Systems." In: *Journal of Bionic Engineering* 12 (Apr. 2015).

[141] Valentine Ivanov Vullev. "From Biomimesis to Bioinspiration: What's the Benefit for Solar Energy Conversion Applications?" In: *The Journal of Physical Chemistry Letters* 2.5 (2011), pp. 503–508. DOI: 10.1021/jz1016069.

[142] Haodong Wang, Zhiyuan Yan, Yongzhuo Gao, Weidong Wang, and Zhijiang Du. "3-D Force Sensing Strategy of Laryngeal Continuum Surgical Robot Based on Fiber Bragg Gratings." In: *IEEE Transactions on Instrumentation and Measurement* 70 (2021), pp. 1–10. DOI: 10.1109/TIM.2021.3106106.

[143] Xiaomei Wang, Ge Fang, Kui Wang, Xiaochen Xie, Kit-Hang Lee, Justin D. L. Ho, Wai Lun Tang, James Lam, and Ka-Wai Kwok. "Eye-in-Hand Visual Servoing Enhanced With Sparse Strain Measurement for Soft Continuum Robots." In: *IEEE Robotics and Automation Letters* 5.2 (2020), pp. 2161–2168. DOI: 10.1109/LRA.2020.2969953.

[144] Junbo Wei, Shuxin Wang, Jinhua Li, and Siyang Zuo. "Novel Integrated Helical Design of Single Optic Fiber for Shape Sensing of Flexible Robot." In: *IEEE Sensors Journal* 17.20 (2017), pp. 6627–6636. DOI: 10.1109/JSEN.2017.2748162.

[145] Robert Wood. "Fly, Robot, Fly." In: *IEEE Spectrum* 45.3 (2008), pp. 25–29. DOI: 10.1109/MSPEC.2008.4457845.

[146] Ran Xu, Aaron Yurkewich, and Rajni V. Patel. "Curvature, Torsion, and Force Sensing in Continuum Robots Using Helically Wrapped FBG Sensors." In: *IEEE Robotics and Automation Letters* 1.2 (2016), pp. 1052–1059. DOI: 10.1109/LRA.2016.2530867.

[147] Han Yuan, Philip Wai Yan Chiu, and Zheng Li. "Shape-Reconstruction-Based Force Sensing Method for Continuum Surgical Robots With Large Deformation." In: *IEEE Robotics and Automation Letters* 2.4 (2017), pp. 1972–1979. DOI: 10.1109/LRA.2017.2716444.

[148] Han Yuan, Lili Zhou, and Wenfu Xu. "A comprehensive static model of cable-driven multi-section continuum robots considering friction effect." In: *Mechanism and Machine Theory* 135 (2019), pp. 130–149. ISSN: 0094-114X. DOI: https://doi.org/10.1016/j.mechmachtheory.2019.02.005.

[149] Huichan Zhao, Jonathan Jalving, Rukang Huang, Ross Knepper, Andy Ruina, and Robert Shepherd. "A Helping Hand: Soft Orthosis with Integrated Optical Strain Sensors and EMG Control." In: *IEEE Robotics & Automation Magazine* 23.3 (2016), pp. 55–64. DOI: 10.1109/MRA.2016.2582216.

[150] Huichan Zhao, Kevin O'Brien, Shuo Li, and Robert F. Shepherd. "Optoelectronically innervated soft prosthetic hand via stretchable optical waveguides." In: *Science Robotics* 1.1 (2016), eaai7529. DOI: 10.1126/scirobotics.aai7529.

[151] Qingxiang Zhao, Jiewen Lai, Kaicheng Huang, Xiaobing Hu, and Henry K. Chu. "Shape Estimation and Control of a Soft Continuum Robot Under External Payloads." In: *IEEE/ASME Transactions on Mechatronics* (2021), pp. 1–12. DOI: 10.1109/TMECH.2021.3116970.

[152] Weikun Zhen, Chaohui Gong, and Howie Choset. "Modeling rolling gaits of a snake robot." In: *Proceedings - IEEE International Conference on Robotics and Automation* 2015 (June 2015), pp. 3741–3746. DOI: 10.1109/ICRA.2015.7139719.

[153] Xue Zhou, Shuguang Li, Xuegang Li, Xin Yan, Xuenan Zhang, and Tonglei Cheng. "A Vectorial Analysis of the Curvature Sensor Based on a Dual-Core Photonic Crystal Fiber." In: *IEEE Transactions on Instrumentation and Measurement* 69.9 (2020), pp. 6564–6570. DOI: 10.1109/TIM.2020.2968777.

DECLARATION

Put your declaration here.

Pontedera, PI, May 2022

Jie Fan

COLOPHON

This thesis was conducted under Ph.D. program of Scuola Superiore Sant'Anna,

https://www.santannapisa.it/en

and hosted by Bioinspired Soft Robotics Laboratory at Istituto Italiano di Tecnologia, Italy. More information is available at:

https://bsr.iit.it/

Thank you very much for your reading and feedback.